

# POLITECNICO DI TORINO

Corso di Laurea Magistrale in Ingegneria Energetica e Nucleare

Tesi di Laurea Magistrale

## **Innovative silicon detectors for measuring the energy of clinical proton beams.**



### **Relatore**

Prof. Sandra Dulla

### **Correlatori**

Dr. Anna Vignati (Università degli Studi di Torino,  
Istituto Nazionale di Fisica Nucleare)

Dr. Felix Mas Milian (Università degli studi di Torino,  
Universidade Estadual de Santa Cruz, Ilheus, Brazil)

### **Candidato**

Cosimo Galeone

Dicembre 2019



Rivolgo i miei ringraziamenti a tutto il team di fisica medica, per avermi accolto in modo spontaneo e umano sin dal primo giorno. In particolare, Anna e Felix, per essere stati sempre estremamente disponibili, gentili e pazienti nei miei confronti.

Desidero ringraziare i miei genitori, e tutti i miei familiari, per essere stati di grande supporto in questi anni, anche se a grande distanza...Infine ringrazio tutti i miei amici (Grottagliesi e non) per aver reso vacanze e, saltuari weekend, dei grandi momenti di svago.

## Abstract.

During my master thesis I investigated the use of innovative silicon detectors optimized for time resolution (Ultra Fast Silicon Detectors, UFSDs) to assess the beam energy of clinical proton beams. The research activity I performed is involved in the MoVeIt project of the INFN (Istituto Nazionale di Fisica Nucleare), aiming at developing new beam monitors for future treatments in charged particle therapy.

The capability to detect single protons and the outstanding time resolution provided by the UFSD technology are exploited to measure protons time of flight (TOF), obtaining the energy and, consequently, the depth of penetration (i.e. the range) of the beams in the tissues.

In the first part of the thesis, the work is focused on the analysis of the signals acquired by two different UFSD detector prototypes during the beam tests in two Italian facilities: CNAO (Centro Nazionale di Adroterapia Oncologica) and Trento Protontherapy Center (TPT).

The TOF has been calculated as the difference of protons time-of-arrival in two UFSD sensors in a telescope configuration, using the constant fraction algorithm. I contributed to develop and implement two different methods to analyze the coincident signals in the two detectors, as reported in chapter 2 together with the detector description and the experimental setup.

The third chapter describes the detector calibration, needed to estimate the time offset (due to the cables and the dead time of the acquisition system) and the distance between the sensors in the telescope with an uncertainty of few hundreds of  $\mu\text{m}$ . I contributed to develop two calibration approaches. The first one (named *absolute approach*) is relying on the nominal energies provided by the clinical facilities, while the second one (*relative approach*) is independent from the nominal energies. The beam energies are then obtained from the TOF values, the distances and the time offset through an analytical approximation validated with Geant4 simulations, taking into account the energy lost in the air between sensors. The preliminary results, obtained with two UFSDs at relative distances ranging between 7 and 97 cm on clinical proton beams with energies between 62 and 228 MeV, showed an error smaller than 1 MeV (at 228 MeV, 97 cm) in the energy estimation.

In the fourth chapter of my thesis, I describe the two MATLAB applications developed for the analysis and the computational simulation of a UFSD sensor specifically designed for the project. The latter, segmented in 8 strips, allows the simultaneous acquisition of 16 signals (8 from each sensor of the telescope). The two methods implemented to analyze the signal of one channel, as described in the second chapter, are extended and applied to measure the TOF with the two 8 strips sensors, identifying the coincident signals. The *relative approach* of the calibration process, described in the third chapter, is validated against the simulation results. The preliminary experimental results and the simulations of the sensor segmented in 8 strips verified the feasibility of a UFSD prototype for the beam energy measurement.

The perspectives and the open-points, like the experimental validation of a final prototype reading out all the 8 strips of the UFSD sensors and the improvement of the data acquisition and processing (to allow the energy estimation in few milliseconds) are described in the final chapter.

# Summary

<b>1. Introduction.....</b>	<b>6</b>
1.1 Interaction of heavy charged particles with matter .....	6
1.2 Advantages of hadron therapy.....	8
1.3 Main features of Trento and Pavia therapy centers .....	11
1.3.1 Cyclotron .....	11
1.3.2 Synchrotron.....	12
1.4 Current detectors in charged particle therapy.....	13
1.5 Ultra Fast Silicon Detectors as new detectors for charged particle therapy.....	16
1.6 Aim of the thesis.....	17
<b>2. Time of flight determination .....</b>	<b>19</b>
2.1 Introduction .....	19
2.2 Detector prototype and data acquisition.....	20
2.3 Time of flight measurement app .....	23
2.4 Signals analysis .....	23
2.5 Time of flight measurement .....	28
2.5.1 Method 1 ( <i>3-sigma method</i> ).....	33
2.5.2 Method 2 ( <i>second gaussian method</i> ) .....	34
2.6 Results .....	36
<b>3. Calibration .....</b>	<b>42</b>
3.1 Introduction .....	42
3.2 Energy measurement .....	43
3.3 <i>Absolute method</i> .....	45
3.3.1 Results.....	46
3.4 <i>Relative method</i> .....	47
3.4.1 Results.....	52
3.4.1.1 Pavia therapy center tests results .....	53
3.4.1.2 Trento therapy center tests results.....	56
<b>4. 16 strips simulation and analysis .....</b>	<b>60</b>
4.1 Introduction .....	60
4.2 Signal simulation.....	62
4.2.1 Geant4 simulation.....	62

4.2.2 Weightfield2 simulation .....	63
4.2.3 Simulation method.....	64
4.3 Time of flight measurement recap.....	69
4.3.1 Method 1 ( <i>3-sigma method</i> ).....	70
4.3.2 Method 2 ( <i>second gaussian method</i> ) .....	71
4.3.3 Results.....	72
4.3.3.1 Measured results vs simulated results .....	72
4.3.4 Facing strip analysis .....	74
4.3.5 Strip-by-strip analysis.....	75
4.3.6 Combination of <i>3-sigma</i> and <i>second gaussian method</i> .....	78
4.4 Alignment analysis .....	80
4.4.1 Y-Z plane misalignment. ....	82
4.5 Calibration validation .....	85
<b>5. Conclusions</b> .....	<b>92</b>
<b>Appendix A.</b> .....	<b>97</b>
<b>Appendix B.</b> .....	<b>99</b>
<b>Appendix C.</b> .....	<b>103</b>
<b>Appendix D.</b> .....	<b>109</b>
<b>Appendix E.</b> .....	<b>111</b>
<b>Bibliography.</b> .....	<b>115</b>

# 1. Introduction.

## 1.1 Interaction of heavy charged particles with matter

The interactions of heavy charged particles, like protons, with atoms and nuclei of the matter can be divided into three categories: interactions with the individual electrons of the atoms, with the nucleus and with the atoms as whole [1].

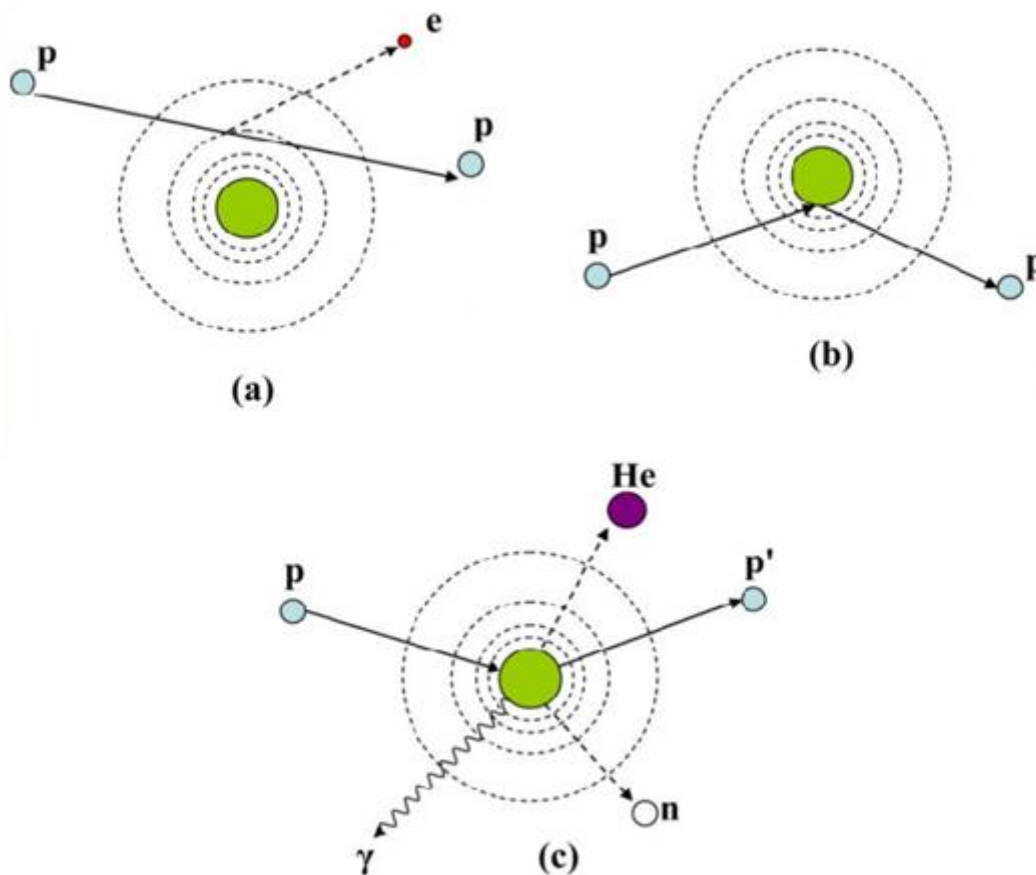


Figure 1.1: Proton interaction mechanisms: (a) inelastic Coulomb interaction with atomic electron, (b) elastic Coulomb interaction with nucleus, (c) non-elastic nuclear interaction. Picture taken from [2].

These processes are called: stopping, scattering and nuclear interactions. The first two proceed via electromagnetic interactions between the charge of the incident particle and the charge of the atomic electrons or nuclei, with nuclear interactions that are relatively infrequent.

Protons lose their energy primarily through electromagnetic interactions with atomic electrons (stopping, Fig. 1a). They exert electromagnetic forces on atomic electrons and impart energy sufficient to ionize the atoms or to excite them. Because of a mass which is large compared to the mass of the electrons (1832 times bigger) protons lose only a small fraction of their energy in a single interaction, and they are deflected by only small angles [2].

As charge particles slow down, they also scatter (Fig. 1b), mainly by interaction with atomic nuclei. Most single deflections, even by nuclei, are very small, in particular for particle heavier than protons. Because the interaction is electromagnetic, through the Coulomb force, the phenomenon is called multiple Coulomb scattering.

The less frequent phenomenon of the three is nuclear interactions (Fig. 1c), even though they lead to a much more profound effect. In these cases, the proton (primary particle) enters the nucleus, with the following generation of secondaries, such as protons, neutrons, heavy fragments like alphas, gamma rays and the recoiling residual nucleus, emitted with a large angle of deflection.

Counting for all these effects, this kind of particles travels an almost straight path through matter, losing energy continuously in small amounts through collisions, mostly, with atomic electrons.

The processes by which protons slow down and deposit energy along their tracks determine the distribution of the **absorbed dose, energy per unit mass of the target**, in the patient. The linear rate of energy loss in a medium for ionization,  $-\frac{dE}{dx}$ , expressed in MeV/cm, is the basic physical quantity that determines the dose that the particle delivers in the medium. It is called **Stopping Power** of the medium for the particle and it is described by the following Bethe-Bloch equation [3]:

$$S = -\frac{dE}{dx} = \frac{4\pi N_A z^2 Z}{m_e c^2 \beta^2 A} \rho \ln \frac{2m_e c^2 \beta^2 \gamma^2}{I} + \text{relativistic terms} \quad (1.1)$$

where:

- $\beta = \frac{v}{c}$ ,  $v$  is the velocity of the particle and  $c$  the speed of light;
- $N_A$ , is the Avogadro number;
- $ze$ , is the particle charge;
- $m_e$ , is the rest mass of the electron;
- $Z, A, \rho$  and  $I$  are the atomic number, the mass number, the density and the mean excitation energy of the medium.

The quantity  $\frac{dE}{dx}$  is negative: as  $x$  increases, the energy decreases. However,  $S$  is almost always defined in terms of mass stopping power, counting for the density of the medium:

$$\frac{S}{\rho} = -\frac{1}{\rho} \frac{dE}{dx} \left[ \frac{\text{MeV}}{\text{g cm}^2} \right] \quad (1.2)$$

and it expresses the rate of energy loss per  $\text{g/cm}^2$  of the medium traversed. Another quantity, closely related to the stopping power, is the **Linear Energy Transfer (LET)**, or restricted stopping power, defined as the average energy locally imparted to the medium per unit track length ( $\text{keV}/\mu\text{m}$ ) [4]. The LET is connected with the absorbed dose as:

$$\text{Dose} = 1.6 \cdot 10^{-19} \text{LET} \frac{F}{\rho} \quad (1.3)$$

where  $F$  is the fluence ( $\text{particle/cm}^2$ ) and  $\rho$  is the density of the medium ( $\text{g/cm}^3$ ).

The dominant terms of the Bethe-Bloch equation are the  $\frac{1}{v^2}$  and  $Z$  dependences. The  $\frac{1}{v^2} \approx \frac{1}{E}$  dependence leads to an increase in the energy loss with decreasing particle energy. At low energies, the velocity of the particle is similar to the one of the orbital electrons in the material with a consequent increase in the probability that the projectile picks up the electrons. Therefore, there is a change of the charge  $Z$ , that must be replaced with  $Z_{eff}$ , the effective projectile charge [3]:

$$Z_{eff} = Z \left( 1 - e^{-125\beta Z^{2/3}} \right) \quad (1.4)$$

Because of these dependences, at non relativistic energies, there is an increase in the energy loss as the kinetic energy of the particle reduces along the track, in particular in the last few millimeters. At the end of the path, the stopping power drops because of a rapid decrease of  $Z_{eff}$ , with most of the energy that is deposited near the end of the trajectory. This effect can be expressed in terms of absorbed dose, through Equation 1.3, as function of the penetration depth.

As shown by Figure 1.2, for a charged particle like proton or carbon ions, the maximum is located at the end of the path shaping the Bragg peak, which depends on the three interaction methods described before.

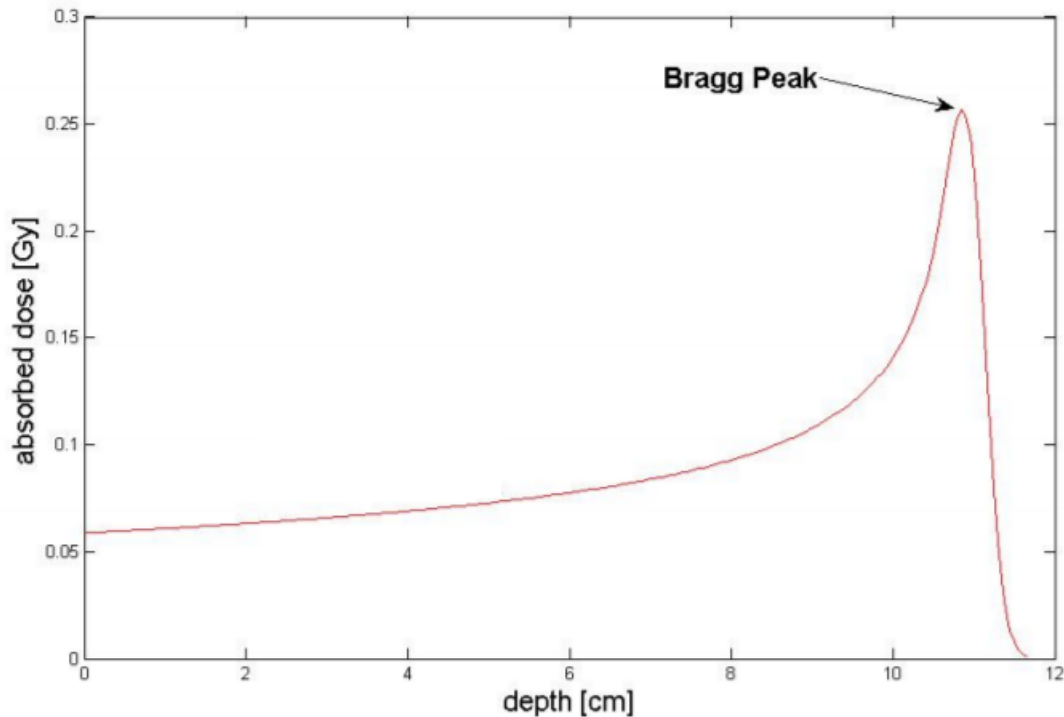


Figure 1.2: Bragg curve for a proton. It describes the absorbed dose function of the penetration depth. Picture taken from [5].

## 1.2 Advantages of hadron therapy

Subatomic particles and electromagnetic waves with energies above few electron volts (eV) are ionizing radiations. This means that particles or photons going through human tissues slow down losing energy and ionizing them. These forms of radiation have enough energy to damage molecules as DNA and can cure cancer by concentrating high dose of radiation directly at the cancerous cells. The development of the radiotherapy techniques based on photon or electron beams has been continuous in the last sixty years with contributions from a large community, and represents a critical and inseparable component of comprehensive cancer treatment and care [6].

The tumors that do not respond positively to conventional radiation therapy are classified as being radio-resistant. Moreover, some tumors are located very close to sensitive organs, which are called organ at risks (OAR), such as the optic nerve or the spinal cord. For these tumors the excellent targeting properties of hadrons can be used to deliver higher doses to the tumor, while reducing the doses absorbed by the surrounding healthy tissues [7]. Such particles have a number of potential

advantages for use in radiotherapy, arising both from the physical aspects of their energy deposition and from biological phenomena resulting from the high density of energy depositions. Indeed, protons and especially carbon ions have a particularly destructive effect on biological tissues at the end of their path, with respect to conventional ionizing radiation [8].

The physical advantage in the use of charged particles, like protons, relies in the distribution of the absorbed dose, which increases with depth and vanishes after a steep maximum, the Bragg peak.

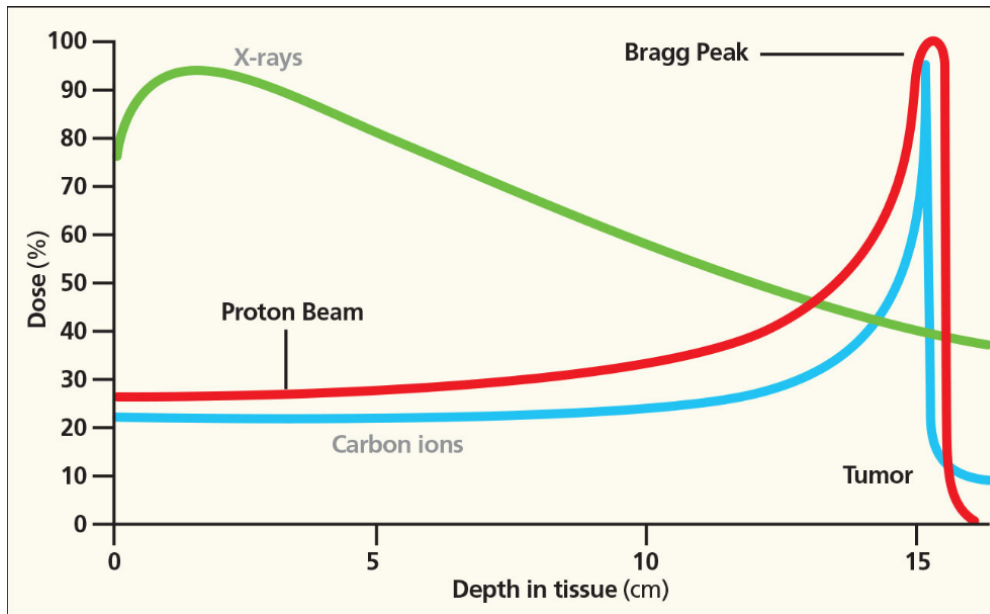


Figure 1.3: Protons and carbon ions deliver most of the dose at specific depth that depends on their energy. X-rays dose distribution reaches the maximum rapidly and then decreases exponentially. Picture taken from [9].

The deposition of X-rays decreases exponentially as they penetrate tissues, while charged particles release almost all the dose in a sharp peak at the end of their path (Fig. 1.3), which depth can be tuned by adjusting the incident particle beam energy. Thus, with accurate dose delivery, particle therapy has the potential to treat tumors more effectively and more precisely, with reduced treatment toxicities and radiation-induced secondary tumor incidence, improving long-term quality of life.

An additional advantage of using heavy charged particles is that the beam can be actively driven by magnetic deflection, reducing the passive components, therefore the lateral scattering that it is already smaller for proton beams (and heavier ion beams) than the penumbra of conventional X-ray or electron beams.

A well-known disadvantage of charged particle therapy is related to the higher complexity and cost of this kind of therapy with respect to the well-established conventional radiotherapy with photons and electrons.

To conclude this rapid introduction to charged particle therapy, it is worth mentioning how the Bragg peak curves shown in the previous figures are used every day to treat patients, as they are evidently not wide enough to cover the volume of the tumor. To achieve it, the energy of the beam has to be varied in a controlled way to obtain many narrow Bragg peaks, that summed up, originates a Spread Out Bragg Peak (SOBP). To deliver the desired dose to the whole treatment volume, this technique is used, consisting of the superimposition of beams with decreasing energies (Fig. 1.4). In Figure 1.5 there is a comparison between the dose deposition coming from a SOBP (protons beam) and a photons beam.

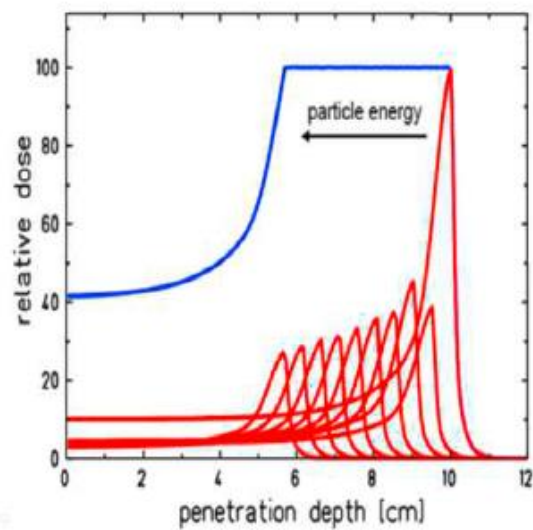


Figure 1.4: Superposition of Bragg peak to form a Spread Out Bragg Peak. Picture taken from [10].

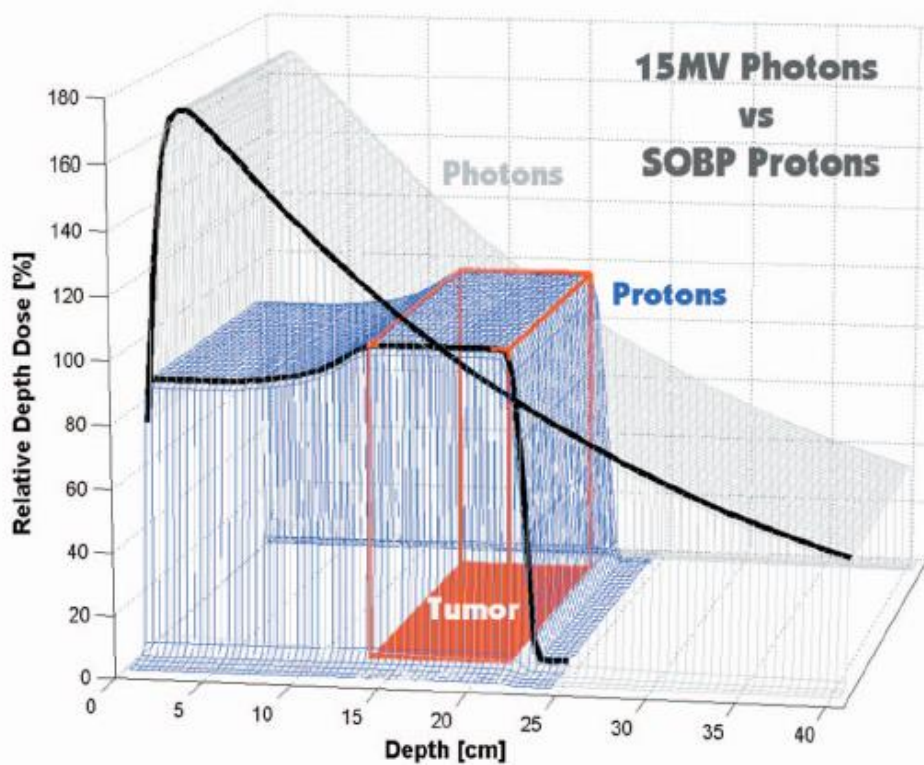


Figure 1.5: Comparison between photon dose distribution and SOBPs, with protons. In red are represented the target volume and the ideal dose distribution. Protons deliver less dose to the region close to the target volume and stop right after. The protons dose distribution is closer to the ideal one more than the photon dose distribution does. Picture taken from [11].

A SOBPs can be performed using two different techniques: passive and active scattering. For the passive scattering, the beam energy required is reached by inserting devices and shifter to degrade the beam, covering the planned target volume. Different approach for the active scanning technique that instead of a broad beam, it uses a narrow pencil beam [12]. To cover the tumor volume, discretized into several layers of equal particle range, the pencil beam is diverted by applying

magnetic fields, to modify the trajectory of the beam, and by energy variations, to reach the required depth of each slice.

### 1.3 Main features of Trento and Pavia therapy centers

Worldwide, there are 63 charged particle therapy facilities, the majority proton centers. There are 11 carbon ions facilities in operation, some of which have also proton capabilities [13].

A hadron therapy facility consists of three main equipment components: (1) a particles accelerator with energy selection system, (2) a beam transport system and (3) a beam delivery system. The beam energy produced by the accelerator must be sufficient to reach the deepest tumors. The most common and diffused accelerators are circular and cyclic like cyclotron, isochronous cyclotron, synchrocyclotrons, and synchrotrons. The physical process involved in accelerator and beam transport design is described by the Lorentz force law:

$$F = q (E + v \times B) \quad (1.5)$$

The application of the electric field  $E$  increases the energy of the particle of charge  $q$ , and the magnetic field  $B$  modifies the trajectory.

Circular machines like cyclotron and synchrotron allows the acceleration of charged particles in a compact machine, reusing the same electric field. In general, they must be able to produce beams which penetrate up to 26-38 cm into the patient tissues and with sufficient intensity (number of particles) to deliver the desired dose within few minutes. However, the energy range and intensity requirements mostly depend on the beam delivery technique adopted.

In Italy, there are 3 charged particle therapy facilities: CATANA (Centro di AdroTerapia ed Applicazioni Nucleari Avanzate, Catania), CNAO (Centro di Adroterapia Oncologica, Pavia) and TPT (Trento Proton Therapy facility, Trento). CATANA is a research center of the INFN (Istituto Nazionale di Fisica Nucleare), equipped with a superconductive cyclotron, where one week per year, ocular melanomas are treated with clinical proton beams. The beam energy, in CATANA, is 62 MeV, with a consequent penetration range of few cm.

The data analyzed during my thesis have been acquired at CNAO and TPT, equipped, respectively, with a synchrotron and a cyclotron.

#### 1.3.1 Cyclotron

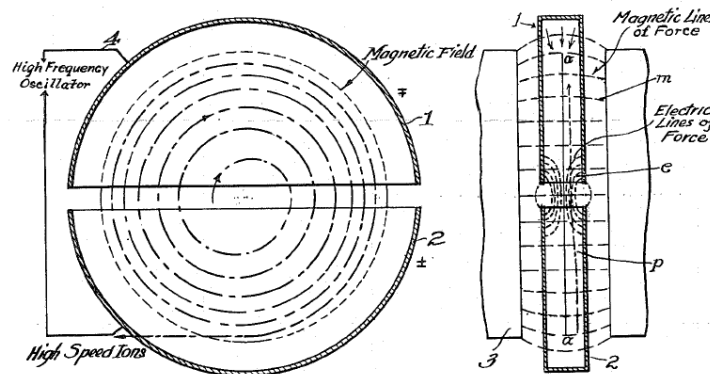


Figure 1.6: Illustration of the beam trajectory on the left side, and of the electric and magnetic field on the right side. Picture taken from [11].

Figure 1.6 shows the scheme of a cyclotron, in which a high-frequency alternating voltage applied across the gap between the two halves (“dees”) alternately attracts and repels charged particles. A magnetic field dipole covers both the “dees”. The particles are accelerated going from one dee to the other (switching the polarity once the particle reaches the gap, to avoid deceleration) and they do not experience any electric field once inside each half. The perpendicular magnetic field lend the circular path, that because of the increase of the velocity becomes a spiral. The radiofrequency of the electric field, to synchronize the path of the particles and the phase of the electric field, derives from the equation  $\omega = \frac{qB}{m}$ . The radius of the trajectory increases until there is no room left. Having an almost constant  $B$  field, the beam energy essentially depends on cyclotron dimension. To reach the required beam energy, according to the depth of the tumor, it must be passively manipulated.

The cyclotron installed in TPT accelerates the beam up to a maximum energy of 228 MeV, that can be reduced to 70 MeV by applying, shortly after the accelerator exit, several rotating degraders of different thickness and material. This is a part of the Energy Selection System (ESS) that allows the selection of the required energy. The beam intensity (number of particles) ranges between 1 and 320 nA, with this current that is the charge collected by an ionization chamber at the exit of the cyclotron, before the ESS.

The proton beam current is modulated over a 50% duty-cycle square wave, with a 100ms period. Calibrated monitor ionization chambers (IC) are installed in the gantries to keep track of the beam flux and position [14].

### 1.3.2 Synchrotron

A cyclotron, instead, uses constant magnetic field and electric field with a constant frequency, both of them are varied in a synchrotron. The path of the particles is kept constant, as they are accelerated, by increasing these parameters appropriately.

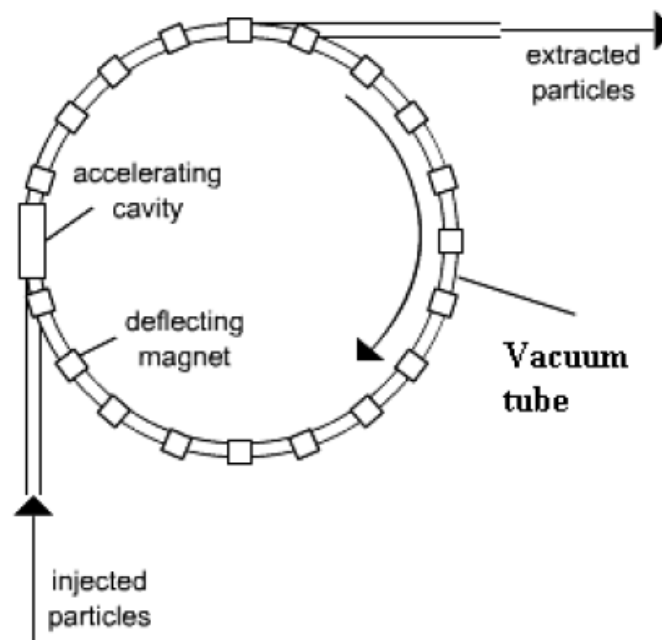


Figure 1.7: Scheme of a synchrotron. The main components, represented, are: injection line, accelerating cavity, deflecting magnets and the extraction line. Picture taken from [11].

Figure 1.7 shows a scheme of a synchrotron. The particles are injected from outside the accelerator by, typically, a LINAC (linear accelerator) with an energy of 3 to 7 MeV. To achieve the required acceleration, the magnetic field and the frequency of the electric field must be increased in synchrony. Having a finite time to cycle the magnets, there is a pulsed output production. The beam acceleration cycle takes (circa) 200ms to 1 s, and the beam extraction occurs over a similar period. The pulse repetition rate is therefore 0.5-2 Hz. Once the beam reaches the required energy it is extracted and delivered to the treatment room (or experimental room) through the beam transport system.

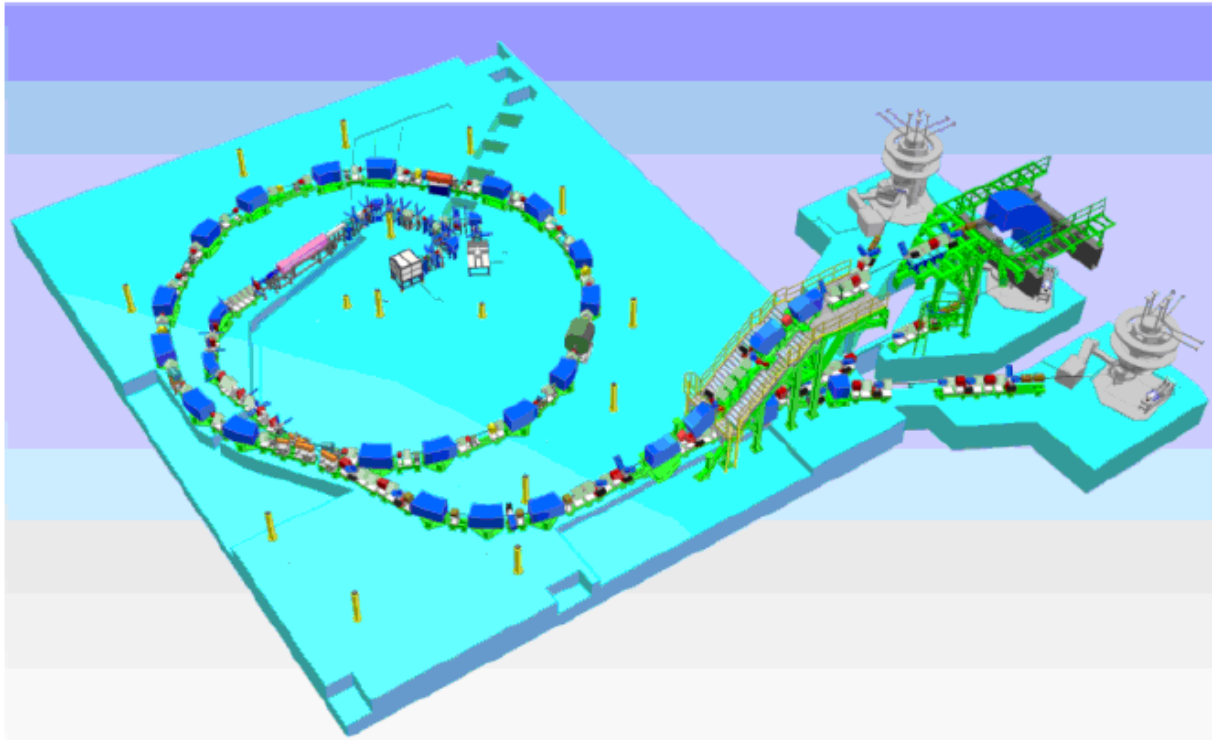


Figure 1.8: Scheme of the CNAO synchrotron. Picture taken from [15].

The CNAO synchrotron (Fig. 1.8) has a diameter of approximately 25m and accelerates protons and carbon ions respectively from 60 to 250 MeV and 120 to 400 MeV/u, corresponding to a range in water of approximately 1mm, up to 27 cm. Sources and LINAC are placed inside the main ring making the accelerator more compact.

As described in this section, both the cyclotron and the synchrotron accelerate the particles in bunches. The main difference is about the frequency of extraction, that in CNAO is 4 MHz and in TPT is 100 MHz. Because of this, the beam of the tests conducted at CNAO seems to be continuous instead of the clear bunched nature of the beam in TPT.

## 1.4 Current detectors in charged particle therapy

Beam monitoring is one of the fundamental steps in particle therapy, because it verifies and drives the beam delivery from the accelerator, with a real-time check of the beam characteristics, like the beam position and number of delivered ions, and the requirements dictated by the treatment plan. As mentioned before, to cover the entire volume of the tumor, in charge particle therapy, the application of different shots at different energies (SOBP) is required, with a prescribed number of particles in each shot. The dose delivery system must drive and hold the beam to the correct positions, until the prescribed dose has been delivered. Today, the main components of the dose delivery system are the gas-filled ionization chambers, able to measure in real-time some beam parameters like the average

flux and the transversal position, by integrating the ionization charge produced by several thousands of crossing particles. This is an indirect measurement of the beam.

The basic functioning of the ionization chamber is related to the electron-ion pair generated by the ionization of a gas, that fills the chamber, crossed by a charged particle. A certain voltage difference is applied between two points of the gas volume boundary. Because of this polarity, there is a collection of these free charges at the correspondent electrode. The information about the beam intensity derives from the resulting charge, current pulse or voltage difference at the detector electrodes.

To generate a detectable electric signal, a large number of charge pairs should be generated and sharply collected, to reduce the impact of recombination effects, that leads to an attenuation of the signal. Indeed, the attraction between two particles of opposite polarity (Coulomb force) ends with the generation of a neutral molecule (recombination effect). The voltage applied to the gas chamber is crucial because, as represented in Fig. 1.9, the electron-ion pair recombination rate is inversely proportional to the bias voltage.

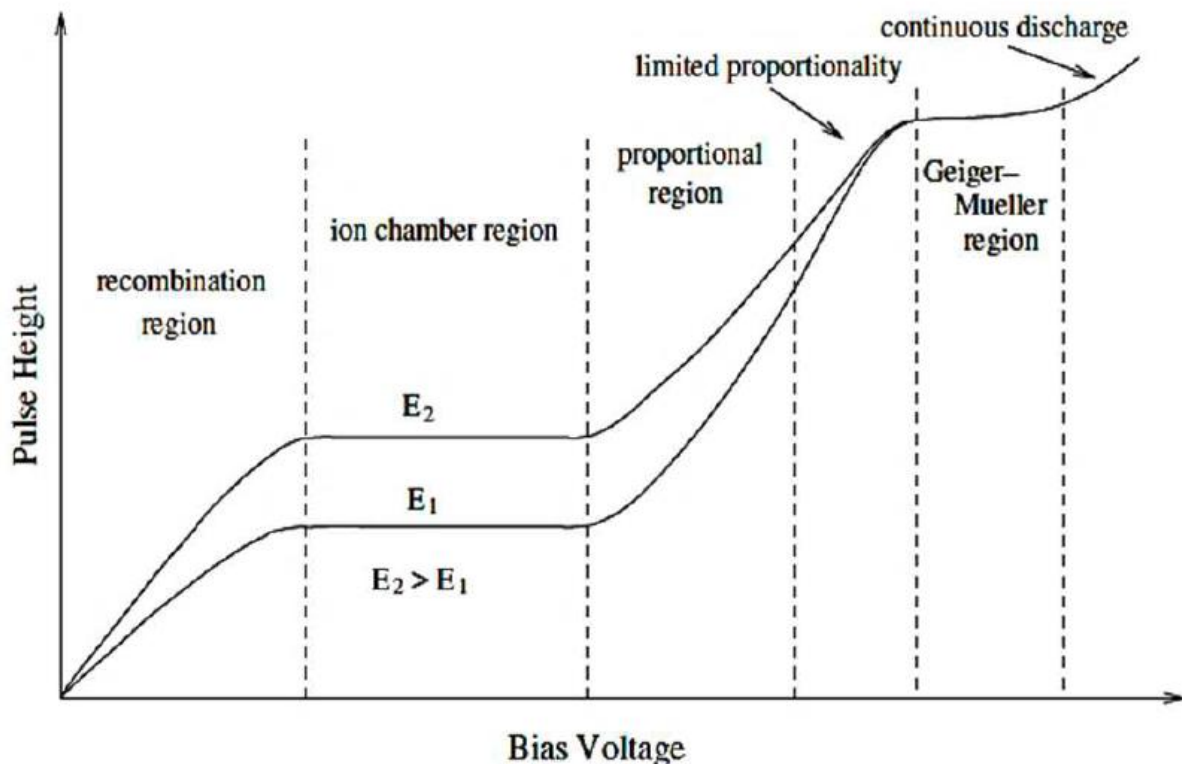


Figure 1.9: Different regions of operation of gas-filled detectors. The pulse height is related to the bias voltage, that defines the detector mode of operation.  $E_1$  and  $E_2$  represents radiation with different energies. Picture taken from [16].

Therefore, increasing the bias voltage there is a reduction of the signal losses, enhancing the capability to collect charges up to a limit, that leads to the detector discharge.

The beam monitors currently used in charged particle facilities are stacks of ionization chambers, including integral chambers with a non-segmented anode to measure the beam flux, and position chambers with segmented anodes. The segmentation of the anodes (in strips or in pixels) allows the measurement of the particles position passing through the chambers. The typical sensitive area of ionization chambers ranges between  $20 \times 20$  and  $30 \times 30$   $\text{cm}^2$ .

The CNAO monitor chambers are enclosed in two independent steel boxes: BOX1 and BOX2 (Fig. 1.10). BOX1 contains an integral chamber (INT1) with a large anode, sensitive area of  $24 \times 24$   $\text{cm}^2$ , for the beam flux measurement, followed by two chambers with the anode segmented in 128 strips,

respectively, with vertical (StripX) and horizontal (StripY) orientations, for the beam position and width measurements. BOX2 is used as backup monitor, carrying the same evaluations of the first one. It contains a backup integral chamber (INT2), followed by a chamber with the anode segmented in 32x32 pixels, 6.6mm wide [17].

There are, in total, 5 parallel plate ionization chambers, filled with nitrogen, corresponding to a total water equivalent thickness of 0.9mm (the energy loss expressed in terms of penetration range in liquid water). They are located close to the patient to reduce the effect of the beam lateral dispersion, due to the interaction of the beam particles with the chamber.

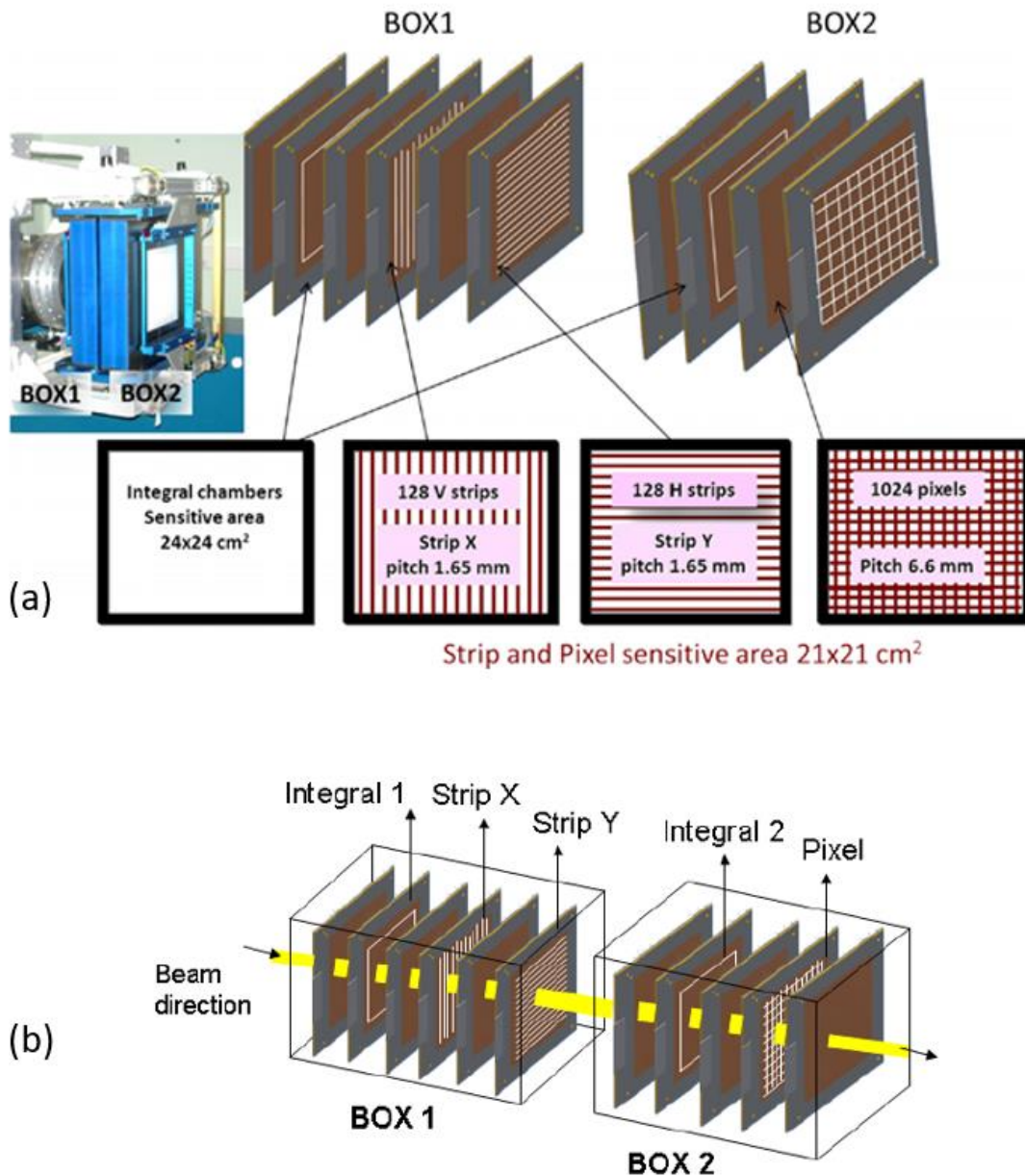


Figure 1.10: Representation of BOX1 and BOX2 of the CNAO dose delivery system. Picture taken from [17].

Ionization chambers have been used successfully for more than 60 years. However, their sensitivity limits the minimum beam intensity that can be safely delivered to the order of thousands of particles, while their slow collection time (hundreds of microseconds) precludes the use of ionization chambers on fast beam delivery strategies, which have been recently proposed. Therefore, ionization chambers represent the current limiting factor in developing completely different treatment strategies that use less radiation, that are faster, more accurate in the spatial delivery of the radiation dose, and that are

less damaging for healthy tissues and more accurate on the tumor target. Any of the new treatment modalities cannot be implemented without developing a monitoring system meeting the clinically driven precision of less than 1% in the number of particles delivered and uncertainty of less than 1 mm in the depth of penetration

## 1.5 Ultra Fast Silicon Detectors as new detectors for charged particle therapy

Current monitors (ICs) have small sensitivity (around  $10^4$  protons minimum to be detectable), slow charge collection time (around 100  $\mu$ s) and poor time resolution. These characteristics do not fulfil the requirements of some new kind of treatments, proposed to compensate for organ movement, such as rescanning [18] and tracking [19]. The latter is the most precise but also the most technically challenging, requiring the energy modulation shot-by-shot, following the motion of the target during irradiations. The rescanning technique works like the active scanning described before. Intrafraction motion can lead to an under- and overdose pattern, that can be averaged by repainting (rescanning) the planned treatment volume (PTV) multiple times, with smaller dose [20].

Within the MoVeIT project, the University of Torino and the Torino division of the INFN are exploring the **direct measurement** of the number of particles, beam energy and position of each particle, as a new monitoring approach in particle therapy [21].

The feasibility of the single particle tracking paradigm for beam monitoring in radiobiological experiments (up to 100 MHz/cm<sup>2</sup> fluence rate or  $10^8$  particles per second) represents the final goal of MoVeIT and an important milestone towards its possible translation into clinics.

Two new devices for on-line measurement of proton flux and energy are being developed, based on the Ultra Fast Silicon Detector (UFSD) technology, recently introduced in high energy physics and described in the following.

The basic functioning of silicon detectors, like Ultra-Fast Silicon Detectors (UFSD), originates from the p-n junction physics. In this kind of sensors, the sensitive area is the depleted region at the interface between two differently doped zones by means of external biasing. A charged particle travelling through the sensitive volumes ionizes the material with the consequent generation of electron-hole pairs (e-h), collected at the n<sup>++</sup> contact (electrons) and p<sup>++</sup> contact (holes). The motion of these e-h pairs induces a current that ends when the last charge carrier reaches its electrode. One electron-hole pair is generated every 3.6 eV released by a particle crossing the silicon detector, while to ionize a gas molecule in an ionization chamber around 30eV are needed. Therefore, with the same amount of energy silicon yields about 10 times the number of charge carriers.

The UFSDs are based on the Low Gain Avalanche Diodes (LGAD) technology, n-on-p silicon detectors with an internal moderate gain due to a thin p<sup>+</sup> layer, placed close to the bottom side of the n<sup>++</sup> electrode of a heavily doped junction. The charges generated by the ionization of the material are multiplied once they cross the gain layer. To reduce noise perturbations and electric field confinement complexity in segmented detector configurations (as the one involved in the experimental tests conducted) the gain is restricted to a value 10-20. The doping profile is not constant but there is a large increase in doping concentration in proximity to the junction, creating a large electric field (Fig. 1.11).

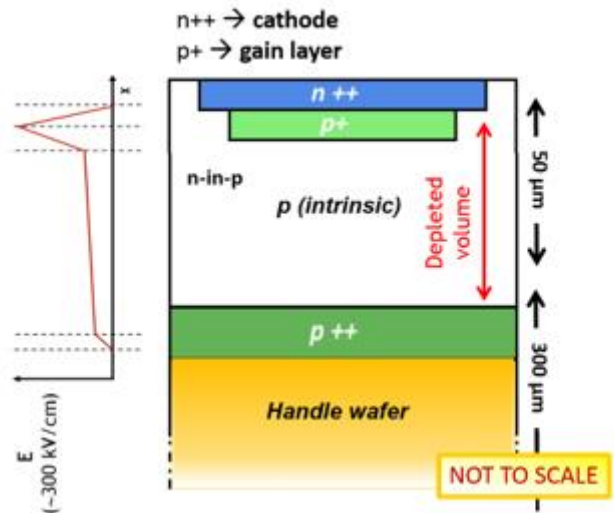


Figure 1.11: Illustration of an Ultra Fast Silicon Detector. The gain layer  $p^+$  posed under the  $n^{++}$  cathode generates a strong electric field ( $\sim 300\text{kV/cm}$ ).

The main advantages of UFSD are the charge collection time of the order of ns and the time resolutions of tens of ps. The ambitious idea of use the UFSD technology to replace the ionization chambers would potentially boost the implementation of faster and more accurate treatment modalities, nowadays prevented by the limits of state-of-the-art beam monitors.

The first MoVeIT detector prototype is aimed at counting the number of beam particles, while the second one will measure the beam energy with time of flight techniques, exploiting the innovative Ultra Fast Silicon Detector (UFSD) technology, recently introduced in high-energy physics experiments.

## 1.6 Aim of the thesis

Currently, the beam energy is not measured during the treatment delivery, but it is certified through checks of the accelerator (for synchrotrons) or proper verification of the range measurement before the treatment (for cyclotrons). A device for a direct and fast online measurement of the beam energy, now missing, would be of great benefit for regular quality assessment controls, for energy checks before the irradiation of new spills or for beam monitoring in future delivery schemes employing fast energy modulation [19].

The final goal of my thesis is the measurement of the proton beam energy from the signals acquired by two UFSD detectors in a telescope configuration (Fig. 1.12). This is a well-known approach consisting in measuring the Time Of Flight (TOF) the particles need to travel a known distance, thus obtaining the particles velocity and their energy. The challenges of the application of such an approach in the hadron therapy environment reside in the clinically acceptable measurement uncertainties and in the required time resolution. Indeed, the TOF detector should perform a prompt measurement of the proton beam energy with less than 1 MeV uncertainty in the clinical range (60-250 MeV). Moreover, in order to monitor the energy during the treatment, the detector has to be non-destructive, i.e. as thin as possible to reduce the multiple scattering, and radiation resistant, at least for about  $10^{15}$  protons/cm<sup>2</sup>, roughly corresponding to one year of clinical proton irradiation in a single treatment line.

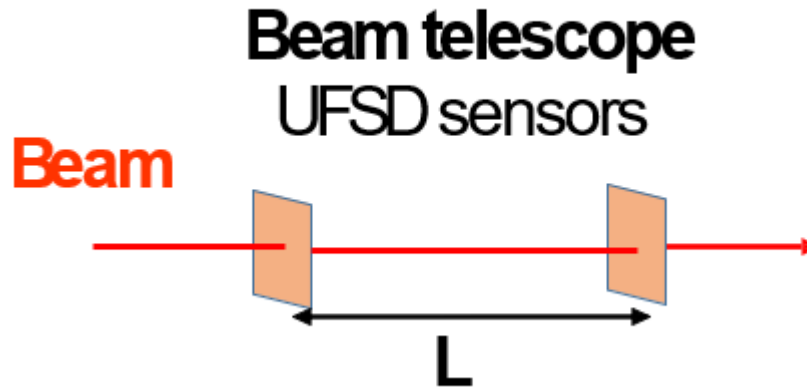


Figure 1.12: Scheme of the telescope configuration adopted for the experimental acquisition of the data.

To achieve the final goal, I contributed to develop and implement a MATLAB [22] application for the TOF determination. This code processes the output signals of the two sensors of the telescope to determine the time of arrival of the particles impinging on each detector ( $t_1$  and  $t_2$ ), identifies the possible coincidences (the signals in the two sensors generated by the crossing of the same particle) and measures the TOF as  $t_2 - t_1$  for the coincident signals. Two different methods have been developed and implemented to treat the coincidences. To validate this application, the experimental signals, acquired at CNAO and TPT using one channel out of the 8 available per each detector, have been used.

The future tests will be conducted reading 8 channels per detector, therefore, the TOF measurement application has been extended, to treat 16 signals. To validate this MATLAB application the future readout of all the sensor channels, I contributed to develop and implement a second MATLAB application for the simulation of 16 signals. This simulation app relies on the data generated by Geant4 and Weightfield2 simulations.

To determine the beam energy, from the measured TOFs (either for the signals acquired during the tests or the simulated ones), I contributed to develop and implement a calibration method of the system, in terms of distance and time offset. Indeed, the system is affected by uncertainties over the positions of the detectors and the time offset, due to the cables and the system used to digitize and store the data (digitizer), that is unknown.

Two approaches have been developed and implemented: *absolute* and *relative approach*. The first one, to calibrate the system in terms of distances and time offset, relies on the nominal energies, because of their small uncertainty being provided by the facility. This has been the first method developed, after the very first tests conducted, and it has been used to verify the feasibility of the project. The *relative approach*, instead, does not use the nominal energies, or any other nominal parameter. The employment of these two methods, with the TOFs measured either from the experimentally conducted tests or from the simulations, leads to very precise values of the beam energy. Thus, the difference between the nominal and measured beam range, at clinics relevant distances, stays within the limit of 1mm, imposed by the regulation, proving the feasibility of the developed methods (to measure the TOF and to calibrate the system).

Many others analysis have been conducted during the development of the main objectives of the thesis. Some of them have been reported, like: the study over the best combination of energies to perform the calibration or the analysis about which is the most performant approach to study the coincident signals, for the 16 channels TOF determination. Others have been overlooked, like the evaluation of the time offset that occurs between different channels of the digitizer.

## 2. Time of flight determination

### 2.1 Introduction

The beam energy determines the depth (i.e. the range) of the dose deposition into the patient tissue, therefore it is one of the most important parameters in order to target properly the tumor. In clinics, the beam energies should allow the treatment of tumors at different depths (3-30 cm) into the tissue, and the required accuracy in the range determination is within 1 mm. A not very precise estimation of the beam energy, with a consequent not accurate penetration range, may lead to an alteration of the dose delivered to the patient.

Currently, the beam energy is not measured during the treatment delivery, but it is certified through checks of the accelerator (for synchrotrons) or proper verification of the range measurement before the treatment (for cyclotrons).

The online measurement of the energy of the particles could play a crucial role in the development of new treatment strategies, such as the ones recently envisaged to treat moving targets and therefore to compensate for organ movement, with shot-by-shot energy modulations. Event though, at this moment, standard accelerators do not have the ability to change the beam range as fast as required by the respiration motion. Efforts towards 4D radiotherapy treatments have been done, using passive energy modulation systems. Indeed, two opposite wedge absorbers able to move orthogonally to the beam direction, increasing or decreasing the thickness of the absorber to reach the required beam energy are available in some facilities [23].

An innovative detector prototype based on a frontier silicon technology (UFSD, already introduced in the previous chapter) is being developed within the MoVeIT INFN project to measure the beam energy during irradiations using Time Of Flight (TOF) techniques.

My thesis aimed at analyzing the data acquired by the aforementioned detector during the tests performed at two clinical facilities for proton beam radiotherapy (CNAO, Pavia, and TPT, Trento), and at simulating multiple signals in order to study the experimental setup in the future step of the project.

To measure the energy of charged particles traveling along a path, with known distance, the TOF technique is a standard method. It detects the times,  $t_1$  and  $t_2$  at which one proton crosses  $S_1$  and  $S_2$ . Having  $\Delta t$  as,  $t_2 - t_1$  and the distance between  $S_1$  and  $S_2$ , the velocity can be calculated as:

$$v = \frac{L}{\Delta t} = c \cdot \sqrt{1 - \frac{E_0^2}{(E_0 + K)^2}} \quad (2.1)$$

where  $c$  is the light speed and  $E_0$  is the rest mass of the proton.

$$K = E_0 \cdot \left( \frac{c\Delta t}{\sqrt{c^2\Delta t^2 - L^2}} - 1 \right) \quad (2.2)$$

The particle kinetic energy can be calculated with Equation 2.2.

In this chapter, there is a description of the detectors setup used during the experimental acquisition of the signals (section 2.2). Then, the method developed for the analysis of the signals is described, aiming at defining the arrival time of the particles in the two detectors ( $t_1$  and  $t_2$ ). In the last section, two approaches are defined to measure the TOF, from the arrival times stored during the signals processing.

## 2.2 Detector prototype and data acquisition

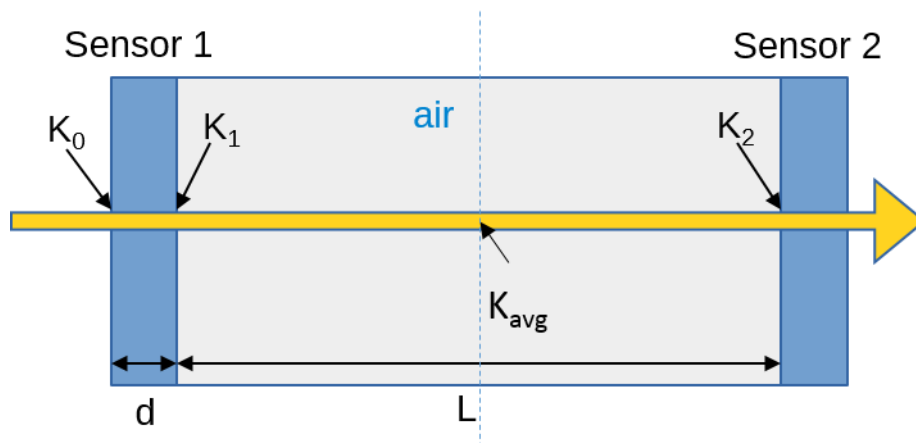


Figure 2.1: Side view of the two detectors (S1 and S2) arrangement.

Two UFSDs sensors  $S_1$  and  $S_2$  (with a defined thickness  $d$ ) at a distance  $L$ , has been used to build a telescope (Fig. 2.2b) and measure the TOF of protons, defined as the time the particles take to cover that distance  $L$ . In a clinical beam line, the isocenter is the reference distance for the patient positioning during treatments, where every beam parameter must be known. In particular, the nominal beam energy provided by the clinics is defined at the isocenter, where the first sensor  $S_1$  is located during the experimental acquisition of the data. For the two tests performed, both at CNAO and TPT, the clinical beam energy range (from 60 to 250 MeV) was considered.

The energy measurement is composed by two main steps: the data acquisition and the data analysis, which will be described in the following sections. For the first beam tests performed at CNAO, the two sensors, in Figure 2.2a, produced at Hamamatsu Photonics, HPK (Japan), have been used. Each sensor is made up of 4 pads, each of them with 80  $\mu\text{m}$  of active thickness and a sensitive area of  $3 \times 3 \text{ mm}^2$ , but only one out of the four pads has been readout for each detector. For the beam test at the Trento Protontherapy center (Trento), strip sensors specifically designed for the MoVeIT project and produced by Fondazione Bruno Kessler, FBK, (Trento) were used (Fig. 2.3).

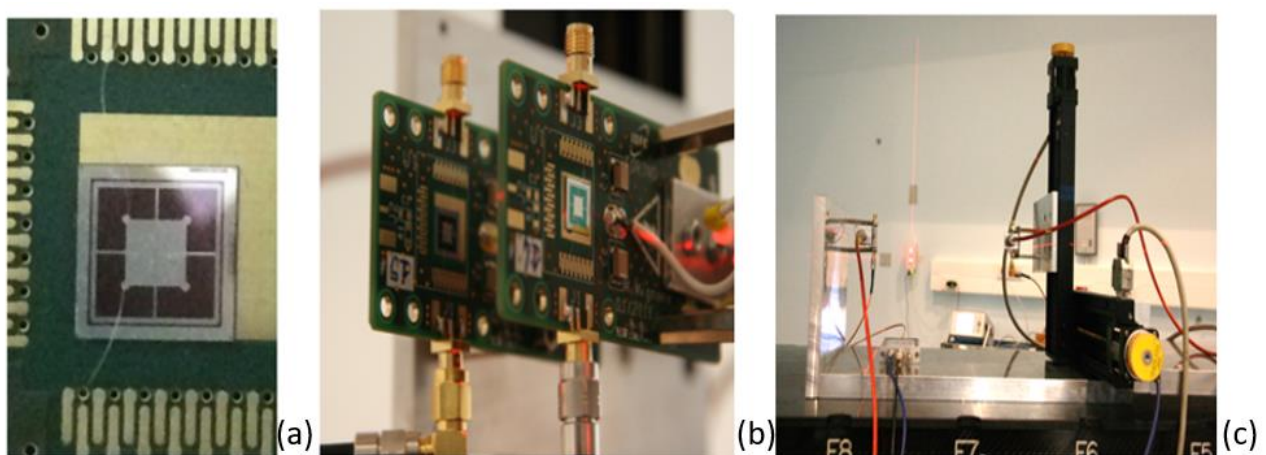


Figure 2.2: a) HPK UFSD detector segmented in 4 pads; b) the telescope made by two UFSDs readout by dedicated boards; c) mechanical support for the detector  $S_2$ , equipped with two orthogonal moving stages.



Figure 2.3: FBK UFSD detector segmented in 11 strips.

Each sensor is made up of 11 strips of  $2.2 \text{ mm}^2$  each, with  $50 \text{ }\mu\text{m}$  of active thickness (Fig. 2.3). For the experimental tests performed, only one strip per detector has been readout.

Both HPK and FBK sensors (used at CNAO and TPT tests, respectively) were mounted on HV distribution boards aligned to the beam, and the considered channel of the sensor was readout by a CIVIDEC amplifier and acquired with a digitizer. The digitizer samples the signal at  $5 \text{ GS/s}$ , with one ADC count corresponding to  $0,24 \text{ mV}$ , and for each trigger stores 1024 samples corresponding to a waveform of  $204,8 \text{ ns}$  duration. 200 samples ( $40 \text{ ns}$ ) waveform obtained from the digitizer is shown in Figure 2.4, from the signals acquired in one of tests conducted at CNAO.

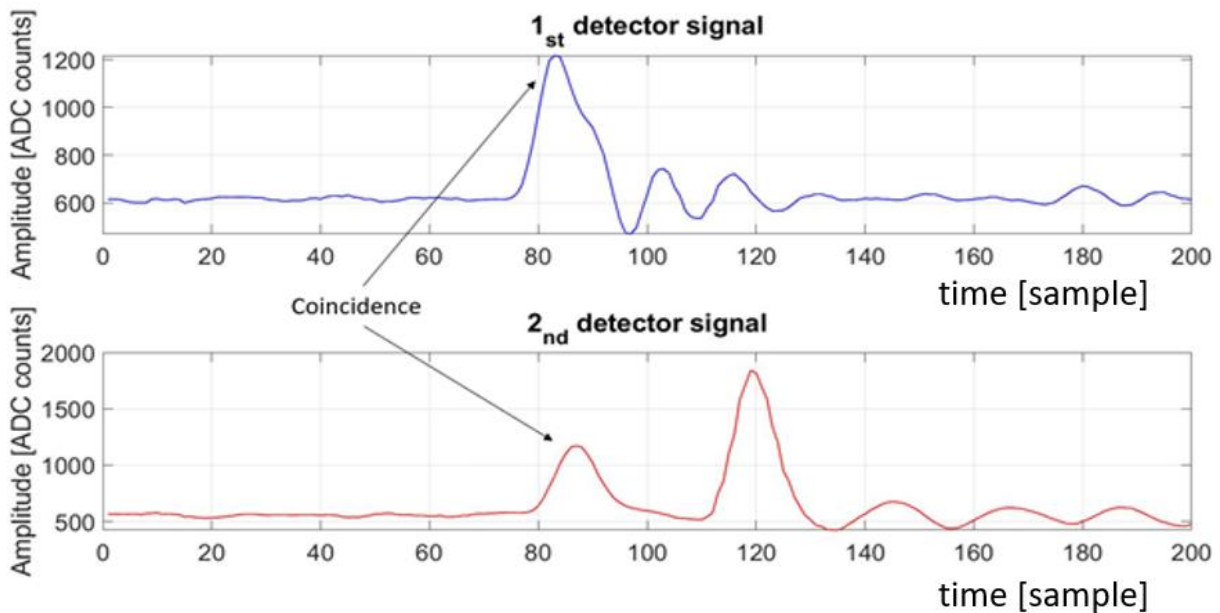


Figure 2.4: 200 samples ( $40 \text{ ns}$ ) acquired from a test conducted at CNAO at  $103.5 \text{ MeV}$ .  $7 \text{ cm}$  of distance between the two detectors. The ones indicated by the arrows are two peaks, generated by the same proton crossing the two detectors (coincidence peak).

The sensors  $S_1$  and  $S_2$  are attached to the board, anchored at the mechanical device, with rigid supports, that keeps the first sensor fixed at the isocenter (Fig. 2.2c), and allows the motion of the second detector at ten different distances (between  $S_1$  and  $S_2$ ), from 7 to 97 cm with a step of 10 cm. To align the two detectors with the beam direction, two orthogonal and movable stages has been used to support and move  $S_2$ , with a LabVIEW program (National Instruments), into a 4x4 grid spaced by 0.5 mm around the starting position.

The alignment is performed measuring the number of coincident peaks, i.e. the signals generated in  $S_1$  and  $S_2$  by the same particle (Fig. 2.4). The best alignment is defined as the position with the maximum number of coincidences (Fig. 2.5), considering the 16 occupied positions. After the alignment analysis, the acquisition can start.

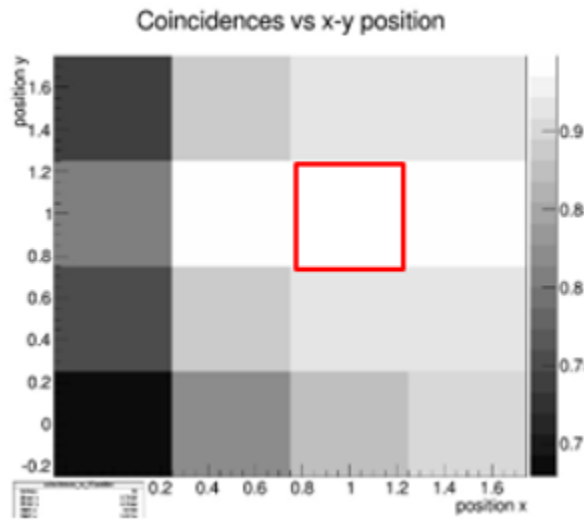


Figure 2.5: Results of the scan in position of the sensor  $S_2$  to find the best detector alignment, achieved for the grid position (1,1).

The data acquisition rate was not optimized. Because of the dead time for conversion (110  $\mu\text{s}$ ) and store the data (around 200  $\mu\text{s}$ ) of the digitizer, only a few percent of the particles delivered has been used. Thanks to the high rate of particles of this kind of treatments this is not a problem in the conducted tests, in which a significant number of coincidences has been collected. For the future translation into clinics, where the system should be able to measure the beam energy within a beam shot (few millisecond) bigger sensitive area will be used to increase the statistics (8 strips, from strip 2÷9, of Fig. 2.3 will be used).

Because of the presence of the cables and the dead time of the digitizer, the time of flight measured in this chapter is affected by a certain time offset, unknown up to this point. Therefore, the real time the particles take to cover the distance between the detectors will be expressed as  $\Delta t = TOF \pm offset$ .

## 2.3 Time of flight measurement app

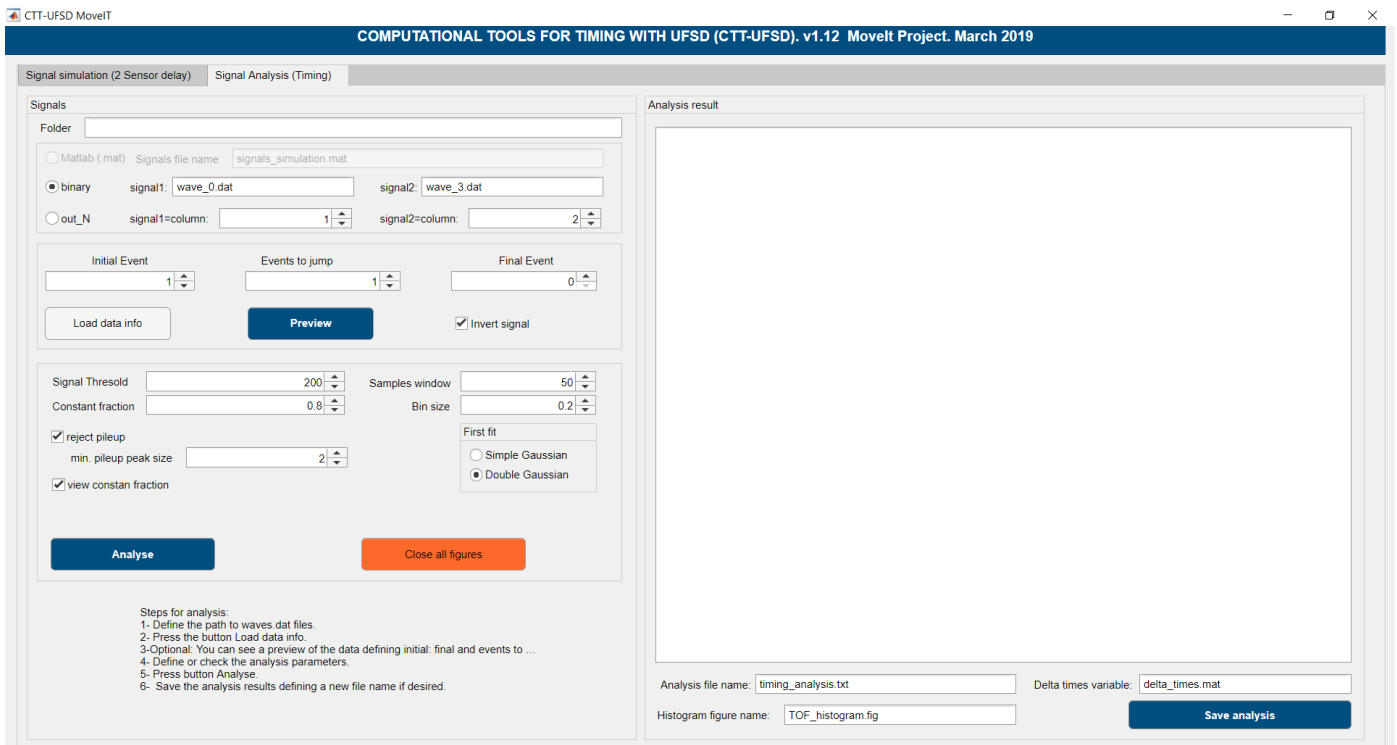


Figure 2.6: TOF measurement app interface.

Figure 2.6 shows the user interface of the TOF measurement app, explained more in detail in Appendix A.

## 2.4 Signals analysis

The raw signals acquired by the digitizer must be “cleaned”, removing the baseline due to the setup of the digitizer, that results as an offset value. The *mode* function of MATLAB recognizes the most recurring value (baseline) that is subtracted from the signal. On top of that, a threshold is decided on the app interface, and once the signal overcome this value, it is possible to detect the peak. For example, in Fig. 2.7 the threshold has been set at 200 ADC counts.

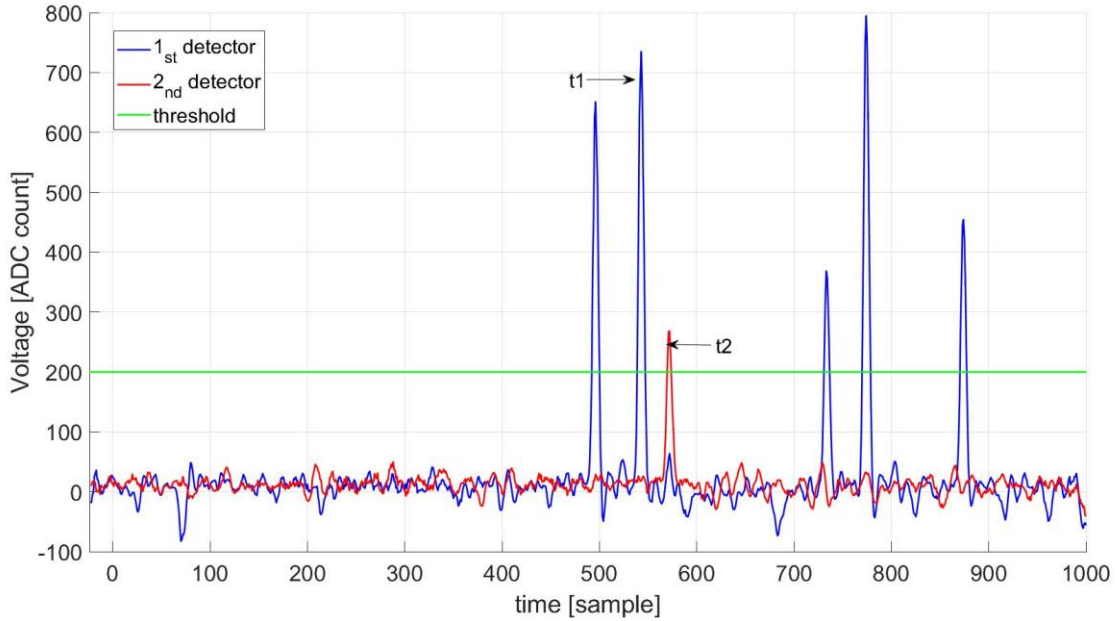


Figure 2.7: One event of the data acquired at TPT, with beam energy 182.8 MeV and 970 mm distance between  $S_2$  and  $S_1$ .

The procedure to determine the TOF starts with the determination of  $t_1$  and  $t_2$ , the exact time at which the particle crosses the sensor  $S_1$  and  $S_2$ . The technique used for this purpose is the Constant Fraction Discrimination (CFD).

The shape of the peak is strictly related to the energy of the beam, with bigger peaks coming from smaller energies, having, in these cases, more energy released in the detector (from Bethe-Bloch equation reported in chapter 1). The variability of the energy deposition (Landau distribution) leads to amplitude fluctuations and shape irregularities.

With the CFD, the arrival time is measured as the time at which the amplitude reaches a percentage of the maximum value of the peak, therefore it depends only on the rising part of the pulse. The CFD is one of the possible methods to reduce the effect of the time walk, defined as the effect that allows bigger signals to overcome a given threshold earlier than smaller ones (Fig. 2.8).

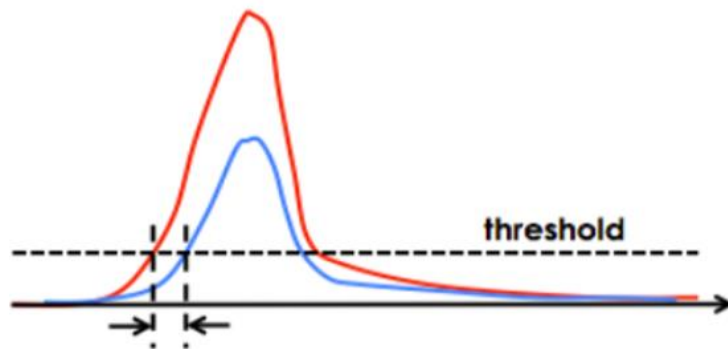


Figure 2.8: Two peaks of different amplitude crossing the threshold at different times.

The arrival time can be estimated through the leading-edge discriminator. Basically, the peak is identified when the amplitude of the signal overcomes the threshold voltage. However, because of the mentioned problem (time-walk effect), this would not be the best choice. The CFD method treats the arrival time independently from the pulse amplitude.

Taking a percentage of the maximum value reached is a way to normalize the peaks beyond their amplitude, and reduces the time walk effect, trying to define, in the most precise way, the arrival time of the particle.

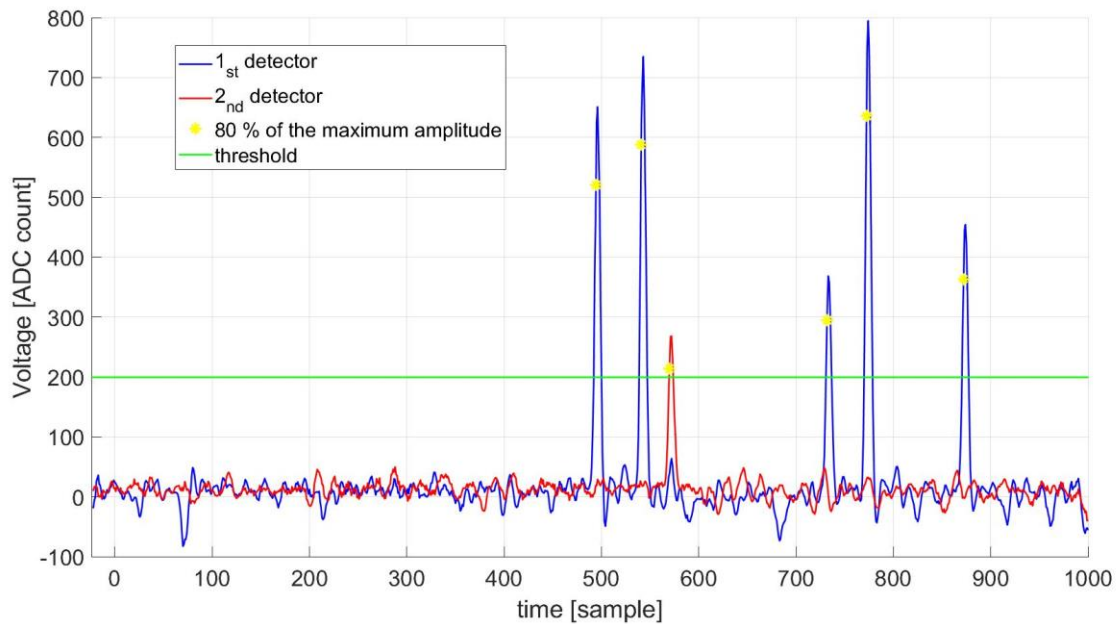


Figure 2.9: Same signals of Fig. 2.7. The yellow star marks the point of the 80% of the maximum amplitude of each peak.

Seeking the peaks in  $S_1$  is the first step of the TOF determination. For each peak generated in  $S_1$  by a proton, the signal generated by the same proton crossing the second sensor  $S_2$  should be identified (coincident peak). To do so, once the arrival time of a proton in  $S_1$  ( $t_1$ ) is located, the program focuses on search of the signals of the second sensor, opening a window of a certain number of samples (decided on the user interface). Any peak, individuated within this sample window, is considered as a coincident peak, and the program stores the difference between the two arrival times ( $t_2 - t_1$ ) for each of them.

For instance, a sample window of 50 samples (corresponding to 10 ns) could be assumed. From Figure 2.9, the first peak (blue one) is too distant from the first peak of the second sensor (red one). The distance between the two of them is bigger than 50 samples.

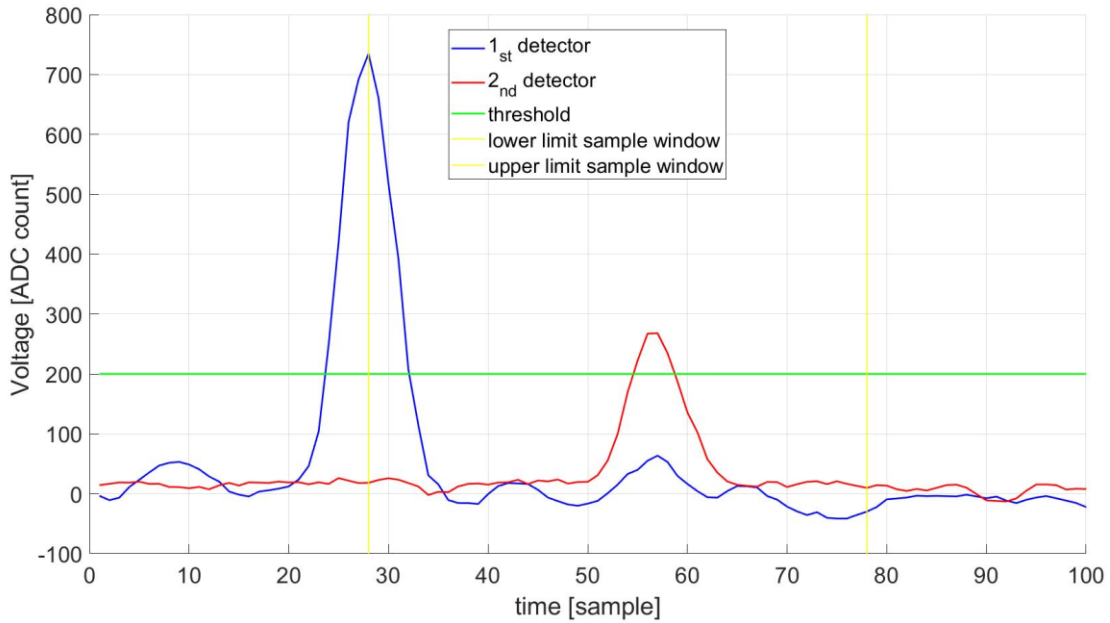


Figure 2.10: Window (yellow lines) of 50 samples used to find out the time of flight of a particle crossing the two detectors. This is a zoom over Fig. 2.7.

Instead, opening a 50 samples window (yellow lines in Fig. 2.10) from the second peak, the system takes a coincidence, with a time of flight of 29.0162 samples, or 5.80 ns. Another typical problem that must be faced reading these signals is related to the pileup.

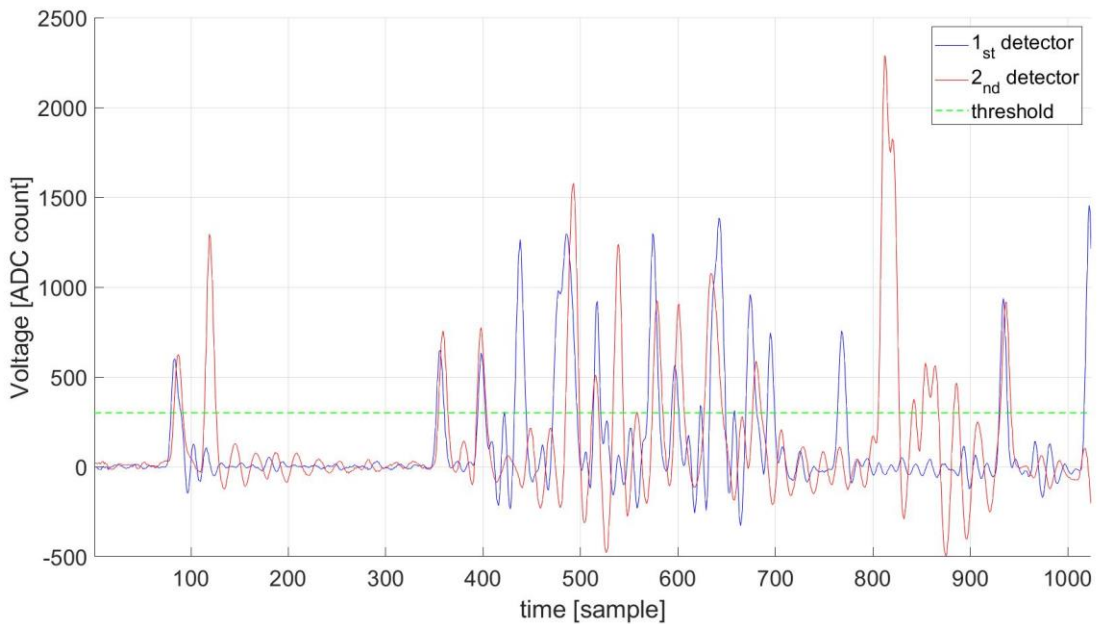


Figure 2.11: One event of the data acquired in CNAO, having 103.5 MeV beam energy and 7 cm of distance between the detectors.

The pileup happens when different protons cross the detector in a time interval smaller than the pulse time duration (system dead time) in this case 2 ns. A pileup signal is shown in Figure 2.12.

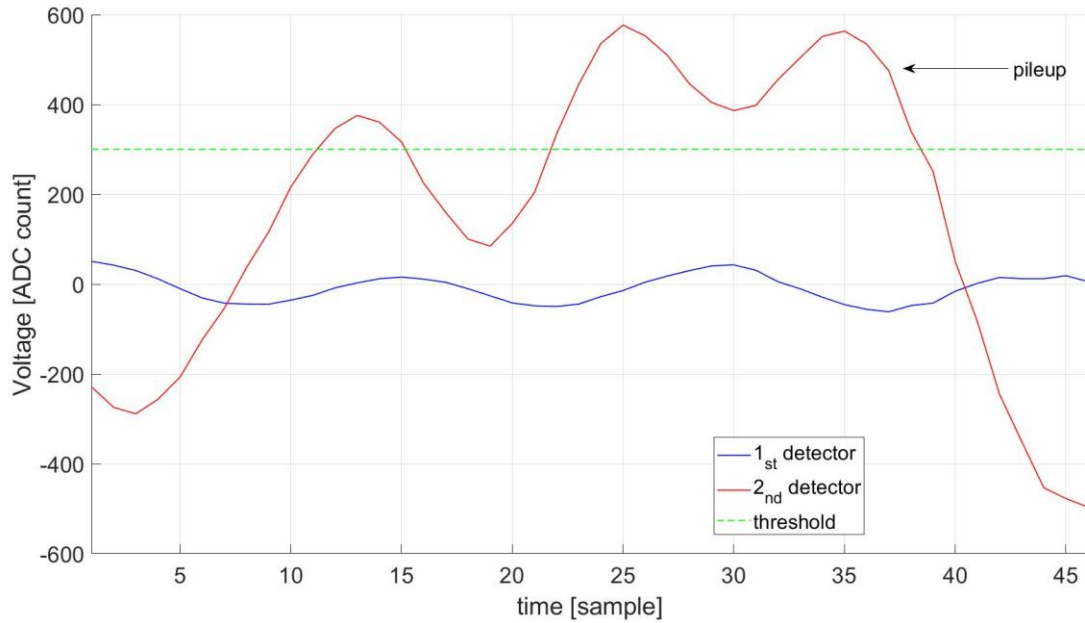


Figure 2.12: Pileup condition in the signal of the second detector. This figure is a zoom over 45 samples of Fig. 2.11.

An algorithm to take care of the pileup has been elaborated. In the situations like the one described in Figure 2.12, there is a peak that occurs during the fall of the previous one. According to the distance between these two pulses, it may be a pileup or another issue, noise generated, called jitter. The code counts the number of pulses between the “right” peak and the possible pileup. If this number is bigger respect the one setup from the user interface (minimum pileup size), the following peak is labeled as pileup, thus neglected. Otherwise, in the jitter situation, that fall is considered as a local minimum of the peak that has not already reached the maximum amplitude.

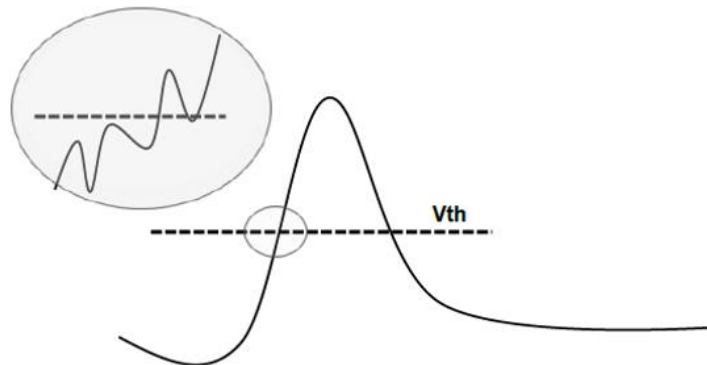


Figure 2.13: Effect of the noise on the signal. In this specific case analyzed over the moment of crossing the threshold value.

In Figure 2.13, the problem of the jitter is focused on the overcoming of the threshold, but this is something that affect in general the signal. Having discretized the peak in a finite, and small, number of points, that “local” fall may be due to this electronic noise-related effect. This is proved by one peak of the very same event of the Figure 2.11.

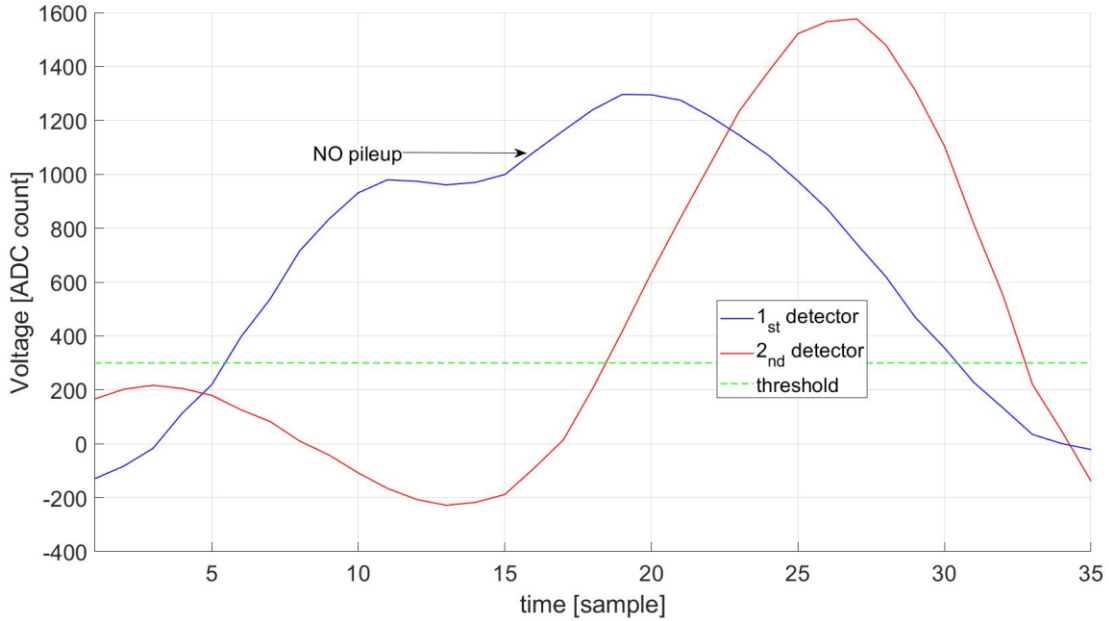


Figure 2.14: No pileup condition in the signal of the first detector. This figure is a zoom over 35 samples of Fig. 2.11, not the same ones of Fig. 2.12.

In this case, the fall lasts exactly 2 steps and then it increases again, but it is not a pileup occurrence, but a noise generated problem. Nevertheless, the choice of the number of steps “allowed” is up to the user. In the evaluated cases, the value 2 proved to be the best choice, but it depends on the noise level and on the amount of point used to discretize the peak.

## 2.5 Time of flight measurement

At this point, for each peak over threshold in  $S_1$ , a list of peaks in  $S_2$  (within the chosen time window) has been saved. In other words, for each incoming proton in  $S_1$ , a list of possible signals generated by the same proton in  $S_2$  has been saved. The CFD algorithm provides a value of time of arrival for each peak. Therefore, for each peak in  $S_1$ , a list of  $TOF_i = t_1 - t_{2i}$  where  $t_1$  is the time-of-arrival of the signal in  $t_1$  and  $t_{2i}$  is the time of arrival of the  $i$ -th possible coincident peak in  $S_2$ , is saved. The histogram of all  $\Delta t$  for all the possible coincident peaks in the two detectors is shown in Figure 2.15.

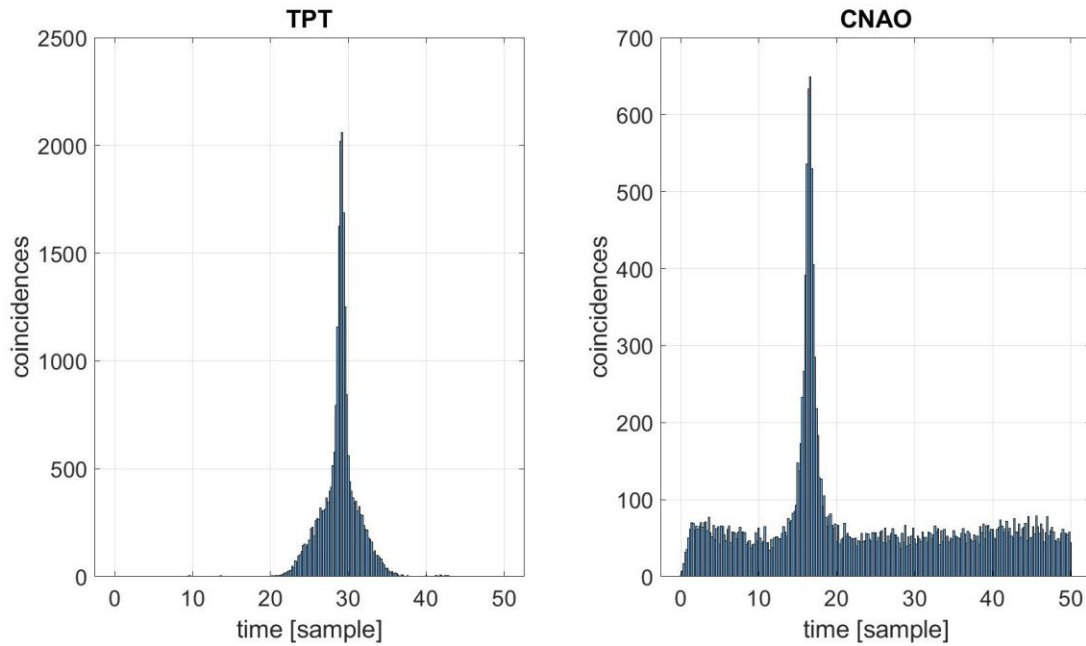


Figure 2.15: Histogram with all the coincidences collected analyzing the signals coming from two different tests. On the left-hand side, test conducted at TPT, at 182.8 MeV, with 970mm between  $S_2$  and  $S_1$ . On the right-hand side, test conducted at CNAO, at 77.6, with 37 cm between the two detectors.

Figure 2.15 shows some differences between the two histograms. The one for TPT has a widening at the base of the peak, while the one for CNAO has a constant background of coincidences. Indeed, because of the different accelerator (synchrotron in CNAO, cyclotron in TPT), the two beams have specific characteristics. In CNAO, the flux is continuous (Fig. 2.16), and this can be appreciated from the histogram (Fig. 2.15), in which there are coincidences all over the spectrum. In TPT, the beam is bunched (Fig. 2.17), having a 50% duty-cycle square wave with 100 ms period. The radiofrequency at which the particles are emitted is about 100MHz. The period, with this frequency is of 10 ns. As a consequence, every 5 ns (25 samples), there are particles coming from the accelerator. This can be appreciated in Figure 2.15, where the coincidences are spread over an interval of about 20 samples (around 4 ns).

It is worth noticing that Figure 2.17 does not show the above mentioned 10 ns period because of the dead time of the digitizer. In fact, the 200 ns acquired, and stored events are interspersed with the conversion time of the digitizer (110  $\mu$ s) and the time needed to transmit and store the data (200  $\mu$ s).

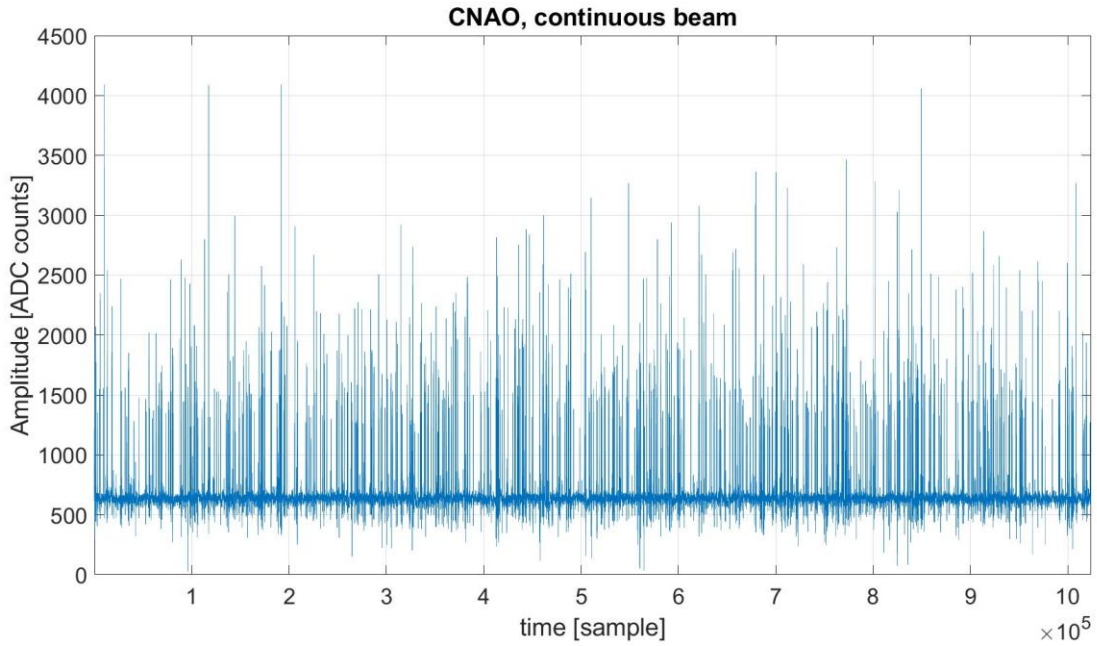


Figure 2.16: 1000 events acquired in CNAO (first detector). The signal is continuous.

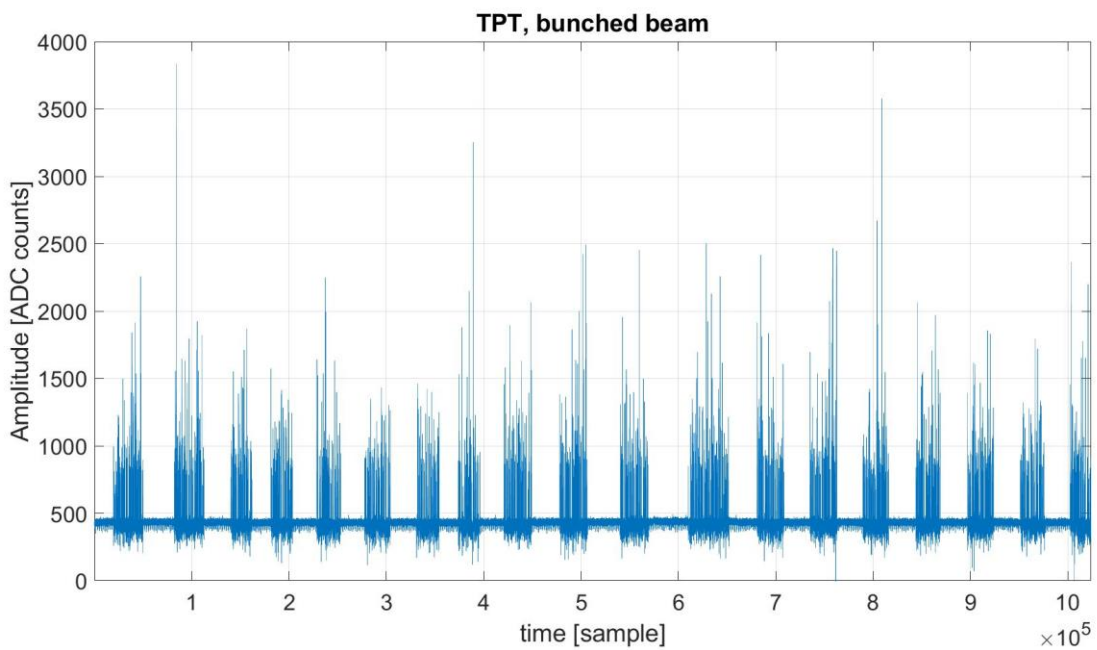


Figure 2.17: 1000 events acquired in TPT (first detector). The signal is clearly bunched.

Having this characterization of the accelerator in mind, a strategy to deal with the false coincidences should be developed. In CNAO there is an almost constant background of coincidences that must be removed. For the acquired data at TPT, instead, the coincidences of the widening at the base of the peak must be removed.

Enlarging the considered time window for the TPT case, further peaks are visible, due to the 10 ns period radiofrequency (Fig. 2.18). Those secondary peaks entirely rely on false coincidences.

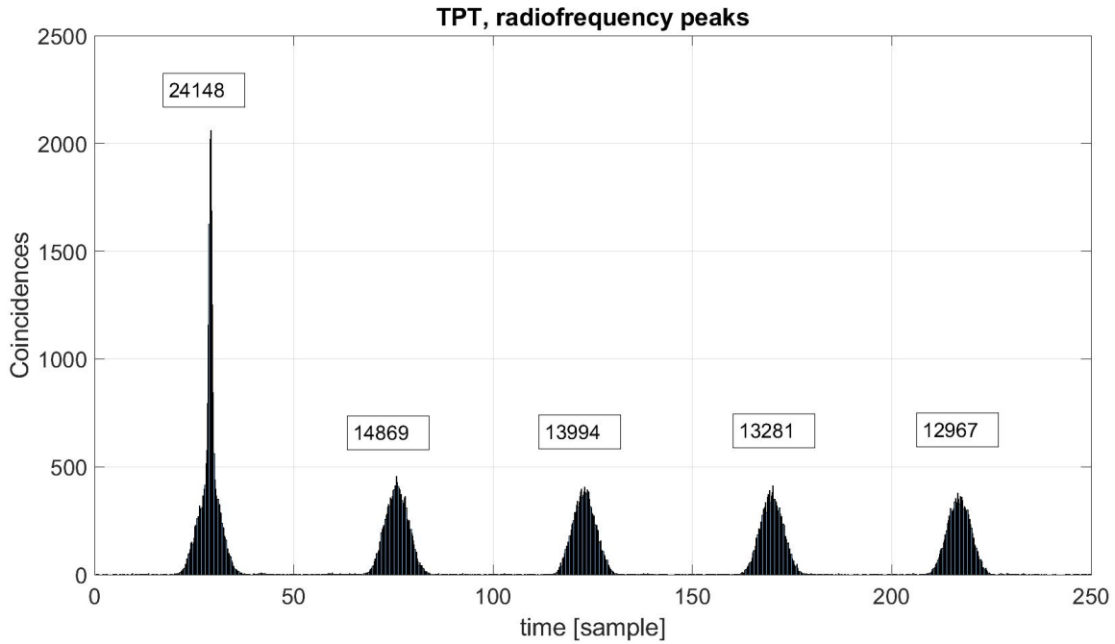


Figure 2.18: Radio frequency peaks in signals acquired in TPT, with the relative number of coincidences collected.

An additional peak can be appreciated every 10 ns, each one characterized by same dispersion and mostly the same number of coincidences. So, looking at Figure 2.19, it is clear that even at the base of the main peak (the one with the true coincidences) an additional peak can be recognized, made up of incorrect coincidences, with the same shape of those peaks on the right side of the Figure 2.18.

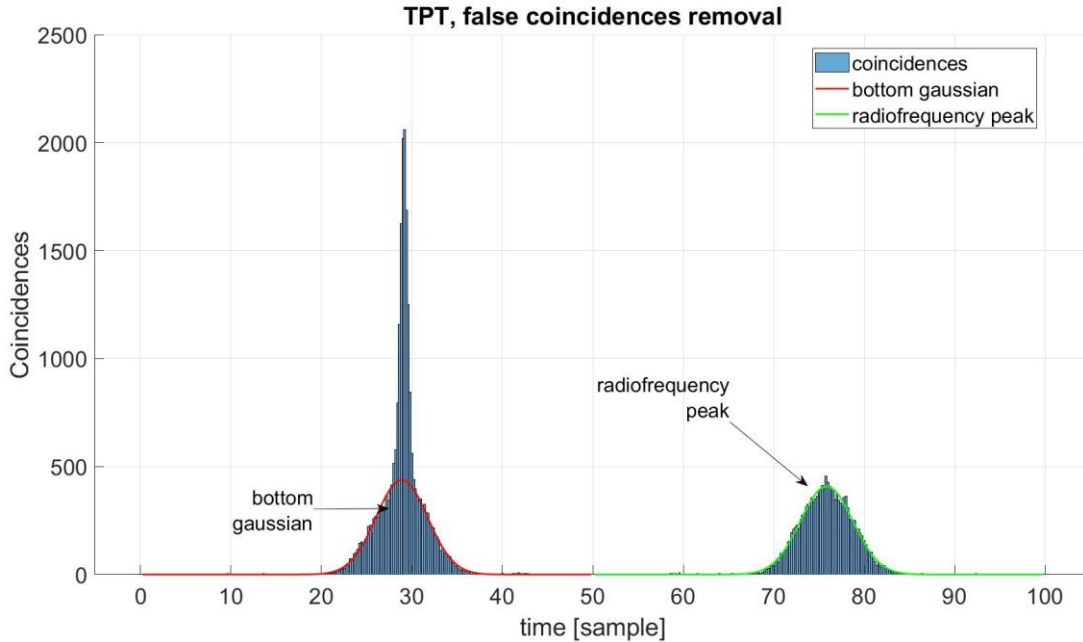


Figure 2.19: Restricted view of Figure 2.18, window of 100 samples. Around 30 samples, there is the main peak of the histogram with the red line that represents the bottom gaussian of a double gaussian fit. On the right-hand side, there is the radiofrequency peak, fitted as single gaussian (green line). The two have similar maximum amplitude and dispersions.

Two methods have been developed to remove these false coincidences, with the ultimate goal of measuring the TOF in the most precise way. Indeed, a wrong TOF, or a big error over the TOF, will affect in a bad way the energy measurement (chapter 3).

The first step of both methods is a double gaussian fit of the histogram (Fig. 2.20).

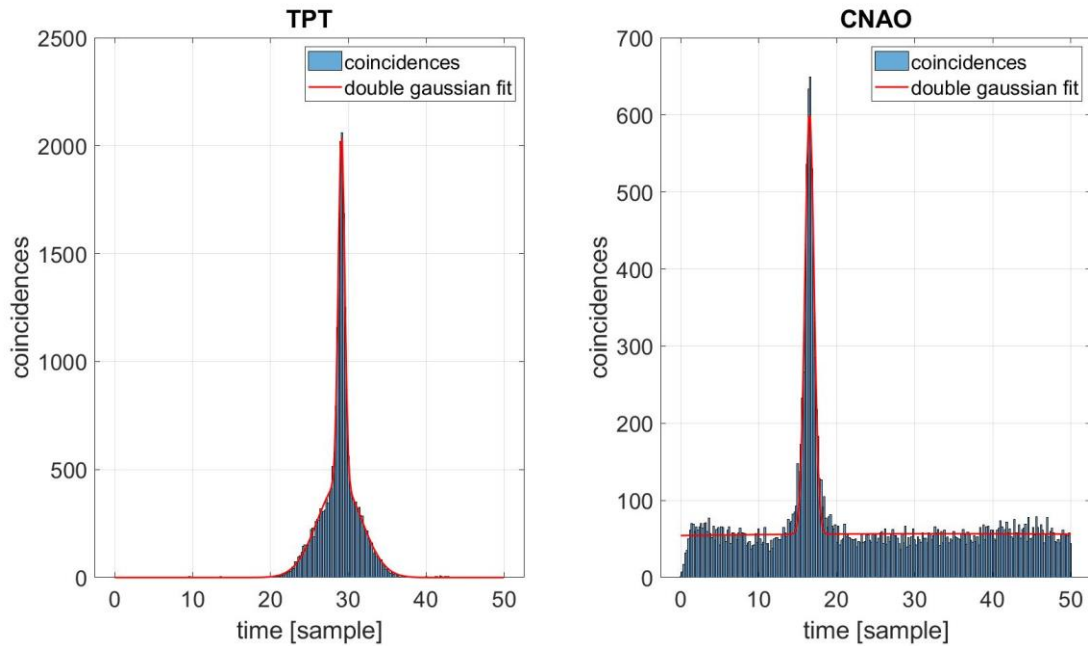


Figure 2.20: Double gaussian fit of the histogram of Fig. 2.15.

In Figure 2.21 are presented the equations coming from the two double gaussian fits (for TPT and CNAO, respectively).

```

General model Gauss2:
fit_TPT(x) = a1*exp(-((x-b1)/c1)^2) + a2*exp(-((x-b2)/c2)^2)
Coefficients (with 95% confidence bounds):
a1 =      1632  (1618, 1645)
b1 =      29.12 (29.11, 29.12)
c1 =      0.5816 (0.5757, 0.5875)
a2 =      437.9 (430.9, 444.9)
b2 =      28.88 (28.85, 28.92)
c2 =       4.035 (3.978, 4.092)
TPT

General model Gauss2:
fit_CNAO(x) = a1*exp(-((x-b1)/c1)^2) + a2*exp(-((x-b2)/c2)^2)
Coefficients (with 95% confidence bounds):
a1 =      549.7 (533.5, 565.8)
b1 =      16.5 (16.48, 16.52)
c1 =      0.8243 (0.796, 0.8527)
a2 =      56.75 (54.12, 59.38)
b2 =      34.11 (-22.03, 90.25)
c2 =     165.7 (-248.4, 579.7)
CNAO

```

Figure 2.21: Equations of the double gaussian fit of the histogram of Fig. 2.15. MATLAB provides the value for each parameter of the equation plus an upper and lower limit of a 95% confidence bound (the values in the brackets).

For the test conducted at CNAO, the second gaussian is a constant (Fig. 2.21), which represents the background of false coincidences, that are on both sides of the peak, and even at its base. For the one conducted at TPT, instead, the second gaussian represents the radiofrequency peak. After this first step, the two methods are different.

## 2.5.1 Method 1 (3-sigma method)

This first method identifies a narrow region around the mean of the peak to remove the false coincidences. It considers as “right” coincidences the ones that are within an interval around the main peak. From the mean value and the dispersion of the first gaussian of the first step (double gaussian fit), this method takes an interval of 3-sigma  $([-1.5\sigma; 1.5\sigma])$ . The width of the interval can be decided from the user interface by modifying the value of the half width. In this case, it has been set at 1.5.

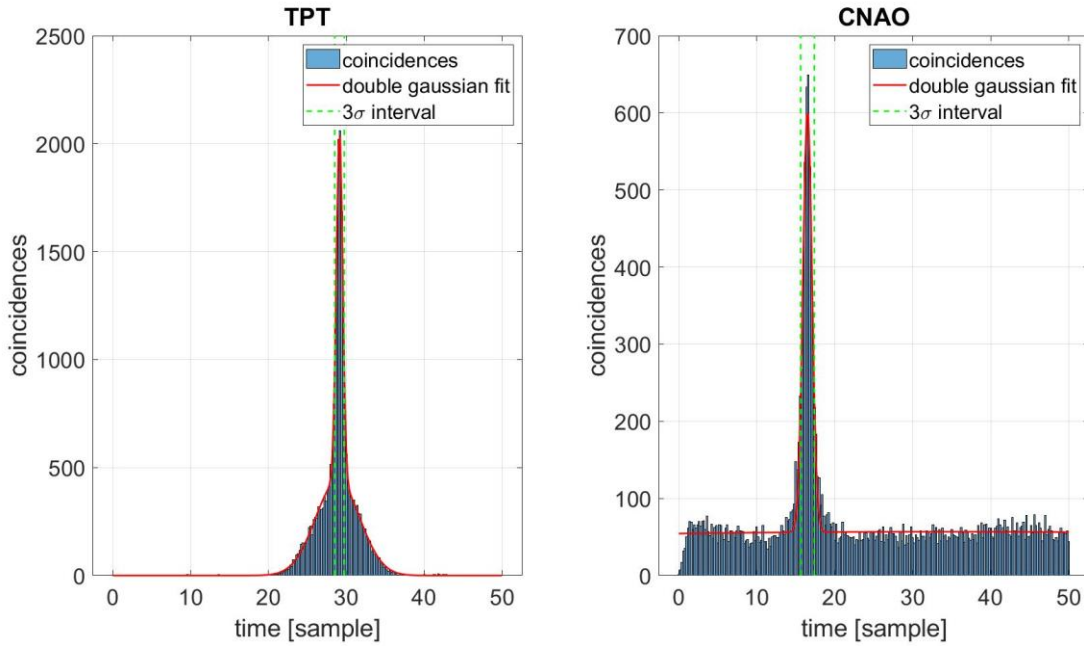


Figure 2.22: Application of the first method (3-sigma method) to treat the coincidences. The time window is narrowed around the main peak. The green dashed lines represent the upper and lower limit of the interval. The coincidences within the interval are considered for the final fit.

From a single gaussian fit of the coincidences in the interval within 3-sigma, the mean TOF, and the related error, are calculated. The TOF is the mean value of this final single gaussian fit, while the error comes from the confidence bound, provided by MATLAB (like the ones of Fig. 2.21):

$$err_{TOF} = \frac{\text{upper limit confidence bound} - TOF_{mean}}{2}$$

The major limit of this method is that, even at the base of the peak there are several false coincidences, in particular for the results of the tests conducted at TPT. To overcome this problem, a second method has been developed.

## 2.5.2 Method 2 (*second gaussian method*)

The second method tries to solve the limitation of the first one, leading to a more precise evaluation of the time of flight. As represented before, the false coincidences profile is different according to the characteristics of the beam. This affects the shape of the second gaussian of the double gaussian fit (first step of the coincidences treatment), as shown in Figure 2.23. This method removes the coincidences that are below the second gaussian from the histogram.

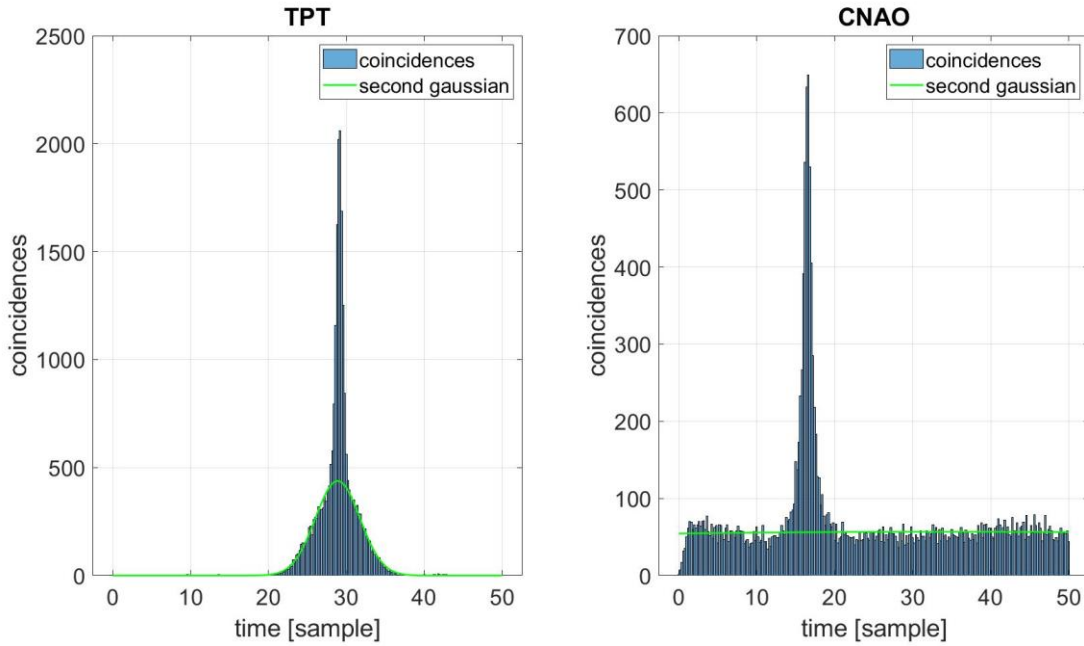


Figure 2.23: *Second gaussian of the double gaussian fit. For the tests at TPT, it has the shape of the radiofrequency peak at the base of the main peak. For the tests at CNAO, it is a constant over the background of false coincidences.*

In this way, the code removes the false coincidences following the characteristics of the beam, proving a certain adaptability. Indeed, for TPT and CNAO tests, respectively, the radiofrequency peak and the constant background are removed. The final step is a single gaussian fit of the left coincidences (Fig. 2.24), from which the mean TOF is defined, as for the *3-sigma method*, while the error is measured as:

$$err_{mean} = \frac{\sigma}{\sqrt{N}} \quad (2.3)$$

with  $N$  that stays as the number of coincidences considered for the final fit, and  $\sigma = \frac{c_1}{\sqrt{2}}$ , with  $c_1$  from the equation of the single gaussian fit (Fig. 2.25).

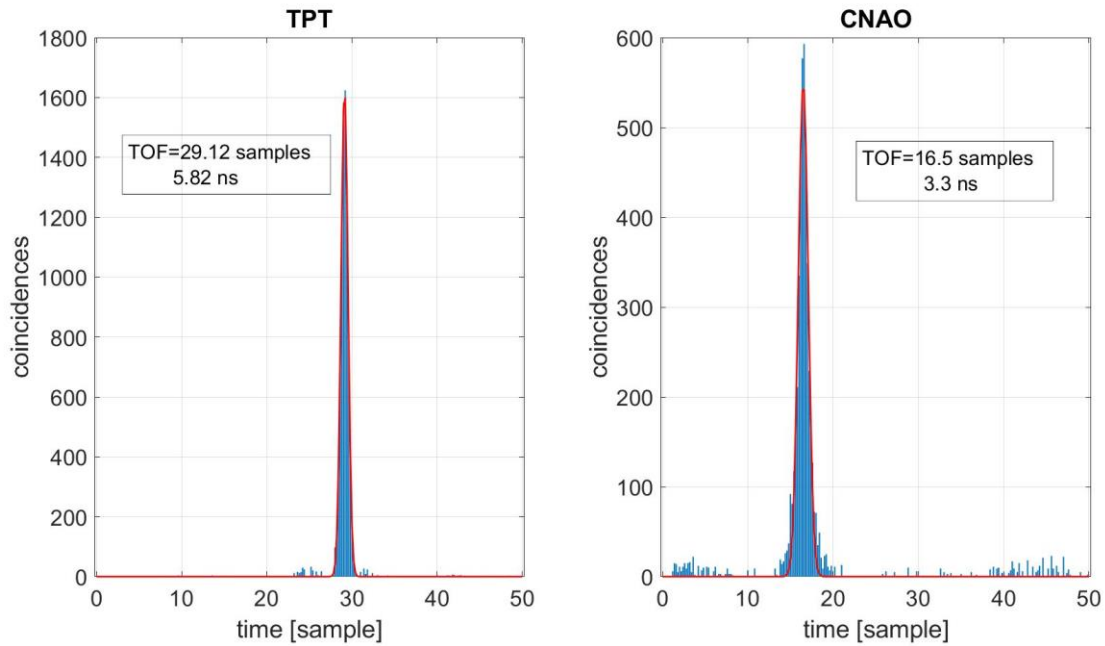


Figure 2.24: Final single gaussian fit of the left coincidences after the subtraction between the ones of the second gaussian from the histogram.

```

fit_TPT =

General model Gauss1:
fit_TPT(x) = a1*exp(-((x-b1)/c1)^2)
Coefficients (with 95% confidence bounds):
a1 =      1631 (1622, 1641)
b1 =      29.12 (29.12, 29.12)
c1 =      0.5816 (0.5778, 0.5855)

fit_CNAO =

General model Gauss1:
fit_CNAO(x) = a1*exp(-((x-b1)/c1)^2)
Coefficients (with 95% confidence bounds):
a1 =      549.7 (536.5, 562.9)
b1 =      16.5 (16.49, 16.52)
c1 =      0.8247 (0.8018, 0.8476)

```

Figure 2.25: Equations of the final single gaussian fit of the left coincidences after the subtraction.

## 2.6 Results

Table 2.1 and Figure 2.26 show the results of the tests conducted at TPT, while Table 2.2 and Figure 2.27 represent the results of the ones conducted at CNAO.

Table 2.1 : Results from the application of the first and second method to the signals acquired at TPT.

TPT		First method			Second method		
distance (mm)	Isocenter energy	TOF [ns]	TOF error [ps]	$\sigma$ [ns]	TOF [ns]	TOF error [ps]	$\sigma$ [ns]
270	68.3	2.395	2.797	0.040	2.394	0.798	0.030
270	98.5	2.023	1.480	0.053	2.024	0.765	0.058
270	147	1.693	3.172	0.066	1.694	0.539	0.066
270	182.7	1.556	5.142	0.063	1.556	0.487	0.060
270	227.3	1.422	1.422	0.084	1.422	0.445	0.093
670	68.3	6.092	2.688	0.062	6.094	1.665	0.062
670	97	5.208	0.984	0.064	5.208	1.107	0.059
670	163	4.175	3.965	0.098	4.173	0.820	0.085
670	182.7	3.993	2.968	0.070	3.992	0.573	0.066
670	222.8	3.696	2.074	0.095	3.695	0.557	0.082
670	227.3	3.664	2.462	0.102	3.664	0.488	0.080
970	68.3	8.880	8.075	0.068	8.882	2.712	0.104
970	98.5	7.589	3.161	0.071	7.589	1.435	0.063
970	147	6.354	7.759	0.083	6.352	0.890	0.072
970	163	6.084	4.968	0.098	6.083	0.914	0.079
970	182.7	5.823	2.360	0.095	5.824	0.869	0.082
970	222.8	5.400	2.542	0.111	5.402	0.756	0.092
970	227.3	5.362	4.497	0.138	5.363	0.692	0.105

Table 2.2: Results from the application of the first and second method to the signals acquired at CNAO.

CNAO		First method			Second method		
distance (mm)	Isocenter energy	TOF [ns]	TOF error [ps]	$\sigma$ [ns]	TOF [ns]	TOF error [ps]	$\sigma$ [ns]
70	58.95	0.765	3.426	0.103	0.764	1.332	0.111
70	77.6	0.692	4.799	0.110	0.691	1.239	0.120
70	103.5	0.624	3.257	0.125	0.624	1.179	0.131
70	148.5	0.551	5.293	0.152	0.554	1.575	0.161
70	226.1	0.488	5.255	0.161	0.492	1.666	0.163
370	58.95	3.724	3.900	0.117	3.725	1.897	0.122
370	77.6	3.302	2.421	0.105	3.301	1.628	0.117
370	103.5	2.921	4.763	0.113	2.921	1.588	0.120
370	148.5	2.522	4.198	0.147	2.523	1.339	0.151
370	226.1	2.161	4.558	0.159	2.161	1.621	0.162
670	58.95	6.699	6.465	0.115	6.699	2.652	0.115
670	77.6	5.922	4.642	0.124	5.922	2.202	0.119
670	103.5	5.231	5.636	0.112	5.231	1.967	0.116
670	148.5	4.518	6.169	0.158	4.520	1.941	0.159
670	226.1	3.864	4.038	0.153	3.863	1.665	0.153
970	58.95	9.667	7.015	0.120	9.666	2.953	0.113
970	77.6	8.552	12.453	0.130	8.549	2.799	0.114
970	103.5	7.551	4.819	0.122	7.548	2.796	0.120
970	148.5	6.510	5.009	0.158	6.508	2.110	0.150
970	226.1	5.557	5.741	0.154	5.557	2.036	0.155

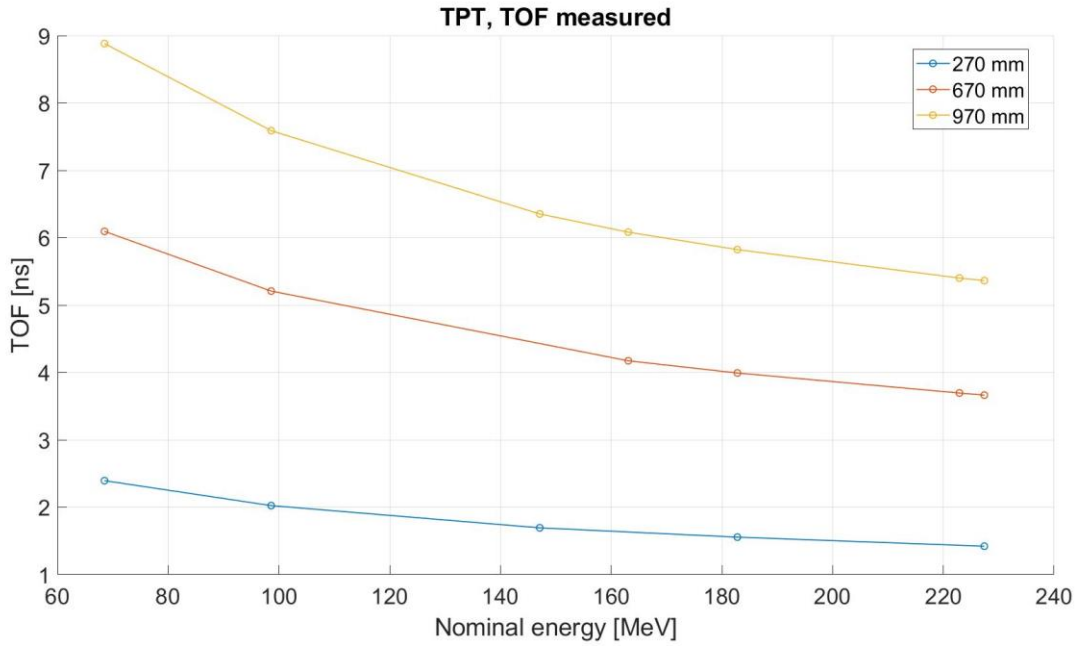


Figure 2.26: TOFs measured from the tests conducted at TPT.

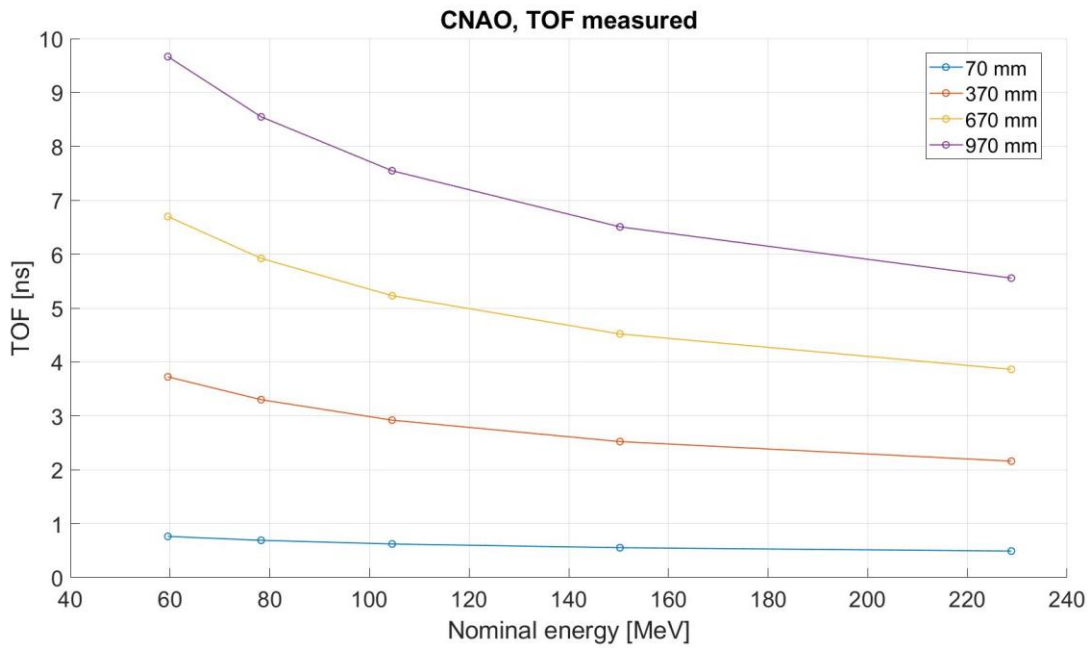


Figure 2.27: TOFs measured from the tests conducted at CNAO.

As predictable, increasing the energy the mean TOF reduces, maintaining the distance fixed. While, keeping fixed the energy and increasing the distance, the TOF increases (Fig. 2.26 and 2.27). The tables reporting the results, in terms of mean TOF and error (Table 2.1 and Table 2.2), show that the mean TOFs coming from the two methods is basically the same. But there is a difference of the error, of the order of few ps.

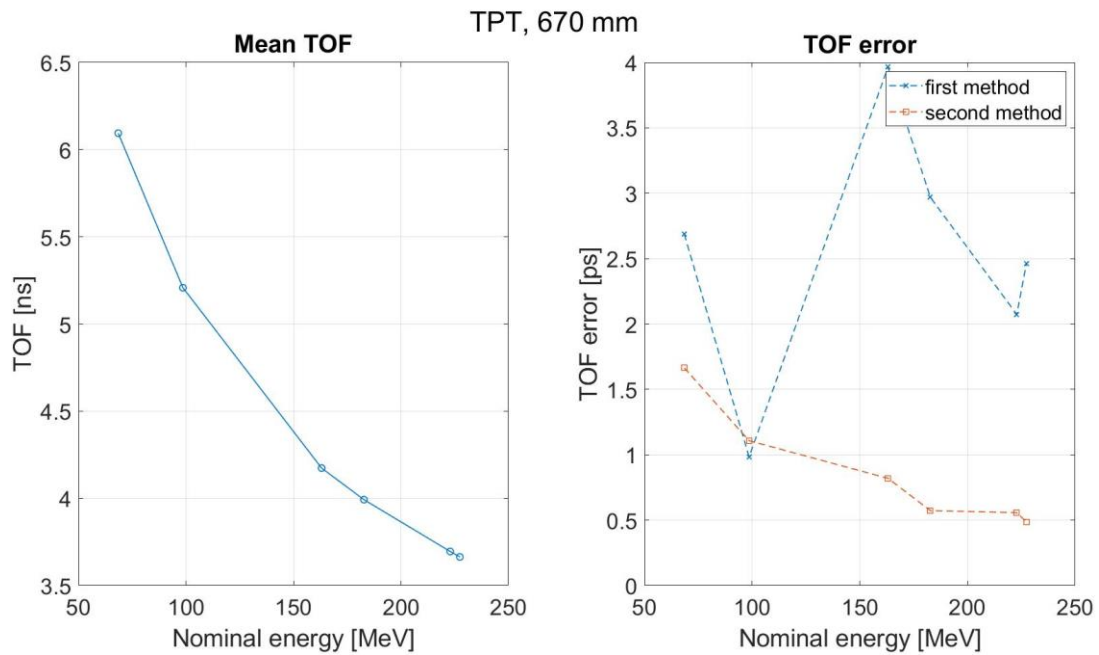


Figure 2.28: Comparison between the results of the two methods applied to treat the coincidences stored. On the left-hand side, there is the profile of the TOF measured at the different energies at which the tests have been conducted in TPT. On the right-hand side, there is the error, coming from the two methods, at each energy. Both the figures consider the case of  $S_2$  at 670 mm from  $S_1$ .

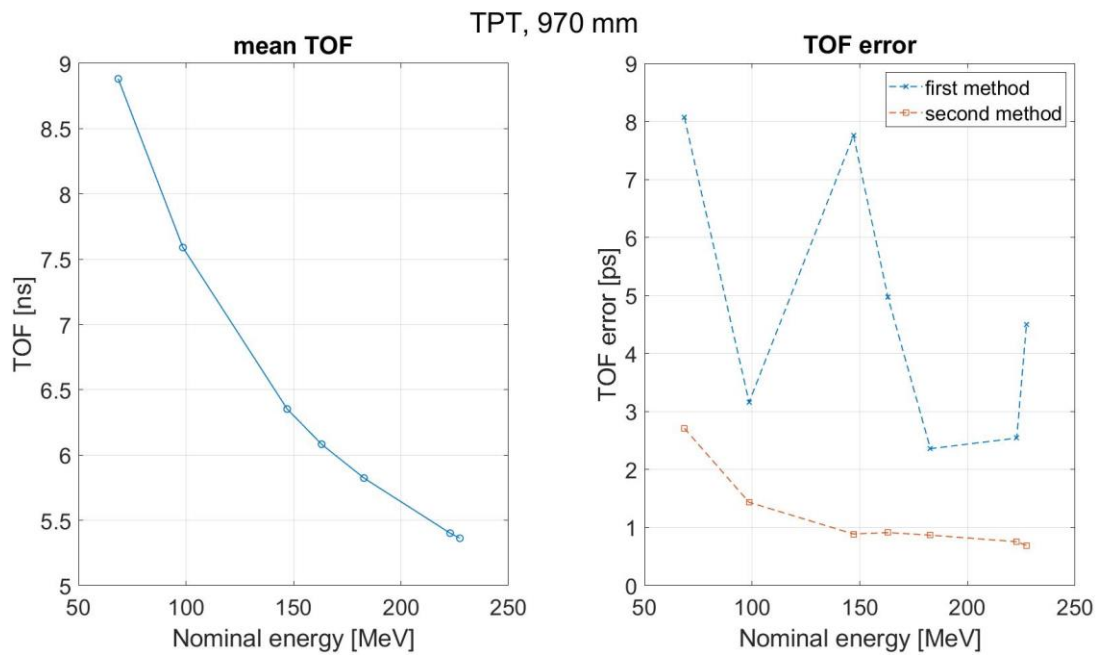


Figure 2.29: Comparison between the results of the two methods applied to treat the coincidences stored. On the left-hand side, there is the profile of the TOF measured at the different energies at which the tests have been conducted in TPT. On the right-hand side, there is the error, coming from the two methods, at each energy. Both the figures consider the case of  $S_2$  at 970 mm from  $S_1$ .

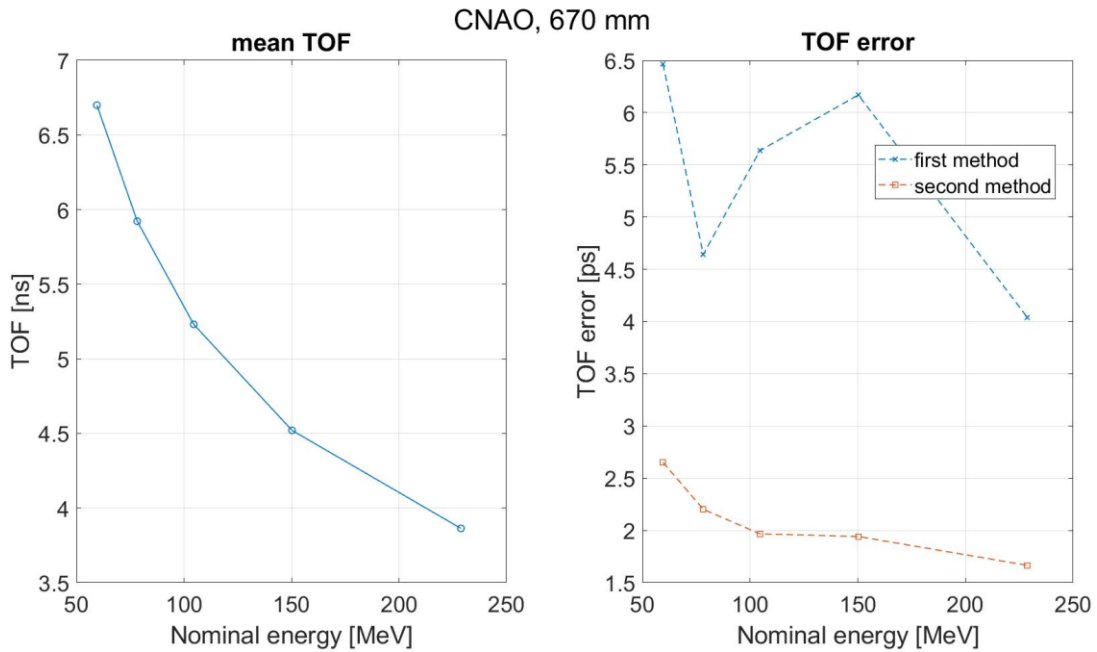


Figure 2.30: Comparison between the results of the two methods applied to treat the coincidences stored. On the left-hand side, there is the profile of the TOF measured at the different energies at which the tests have been conducted in CNAO. On the right-hand side, there is the error, coming from the two methods, at each energy. Both the figures consider the case of  $S_2$  at 670 mm from  $S_1$ .

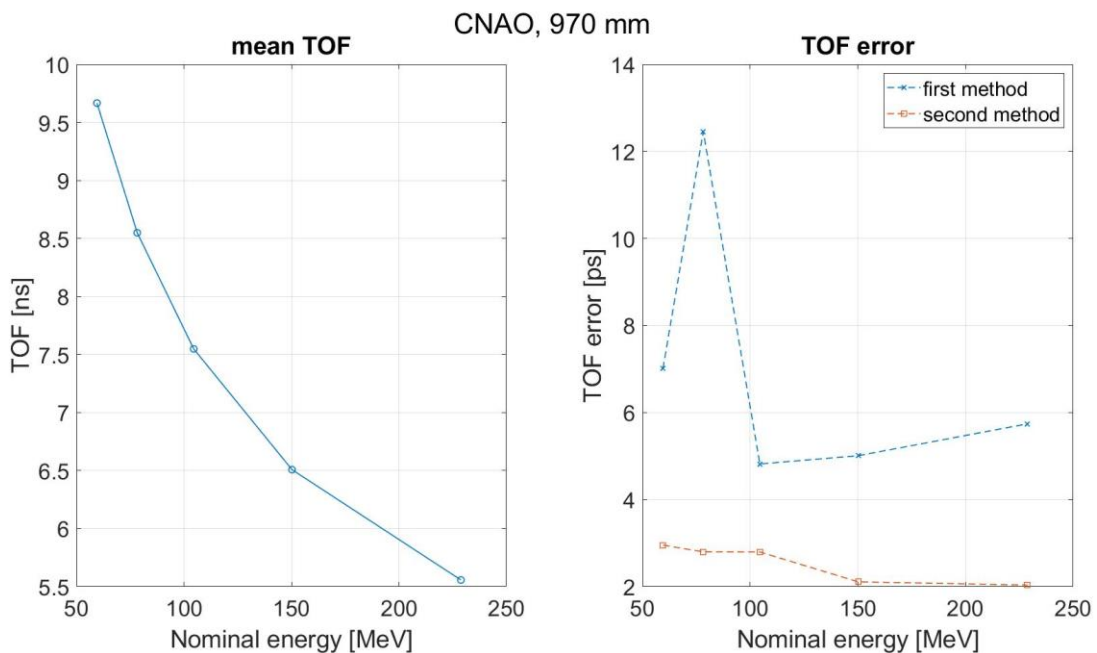


Figure 2.31: Comparison between the results of the two methods applied to treat the coincidences stored. On the left-hand side, there is the profile of the TOF measured at the different energies at which the tests have been conducted in CNAO. On the right-hand side, there is the error, coming from the two methods, at each energy. Both the figures consider the case of  $S_2$  at 970 mm from  $S_1$ .

In figures from 2.28 to 2.31 is reported the profile of the mean TOF and mean TOF error: TPT and CNAO at 67 and 97 cm, comparing the two methods. On the left-hand side there is the mean TOF, represented by just one line, instead of two (for the two methods). This is because the measured TOFs, from the *3-sigma method* and the *second gaussian method*, are pretty much the same. Indeed, the difference between these results would not be appreciable on a nanoseconds scale. On the right-hand

side there is the error on the TOF measured with the two methods, and it is possible to appreciate that the ones of the second method are always smaller than the ones of the first method. They are, mostly, of the order of few ps or even smaller, but they have a serious impact over the energy measurement, as will be clear in the next chapter. There is, in fact, a limit to the acceptable value of the TOF error to maintain the energy measured within the limit of 1 mm of water range allowable. This aspect is explained in the following chapter.

The profile of the error coming from the second method shows another important aspect. Indeed, increasing the energy, at fixed distance, the error gets smaller. This is due to the increase of the number of particles that reach the second detectors, increasing the statistics for the TOF measurement.

## 3. Calibration

### 3.1 Introduction

The beam energy is often characterized in terms of beam penetration range, with liquid water used to mimic the patient tissue (Fig. 3.1). This range is the relevant parameter in clinics. Knowing the beam energy, the range can be retrieved from the PSTAR table (National Institute of Standards and Technology) or with the Bragg-Kleeman rule [24], as:

$$R = N \cdot E^\beta \quad [cm] \quad (3.1)$$

with  $N$ , proportionality factor [ $g/cm^2 \text{ MeV}$ ] that is approximately proportional to the square root of the effective atomic mass of the medium, and  $\beta$ , an exponent factor of the kinetic energy ( $E$ ), dimensionless. In my thesis, this equation has been used, with values of  $N$  and  $\beta$  defined by the International Commission on Radiation Units and Measurements (ICRU), respectively equal to:  $0.0023 \text{ g/cm}^2 \text{ MeV}$  and  $1.75$ .

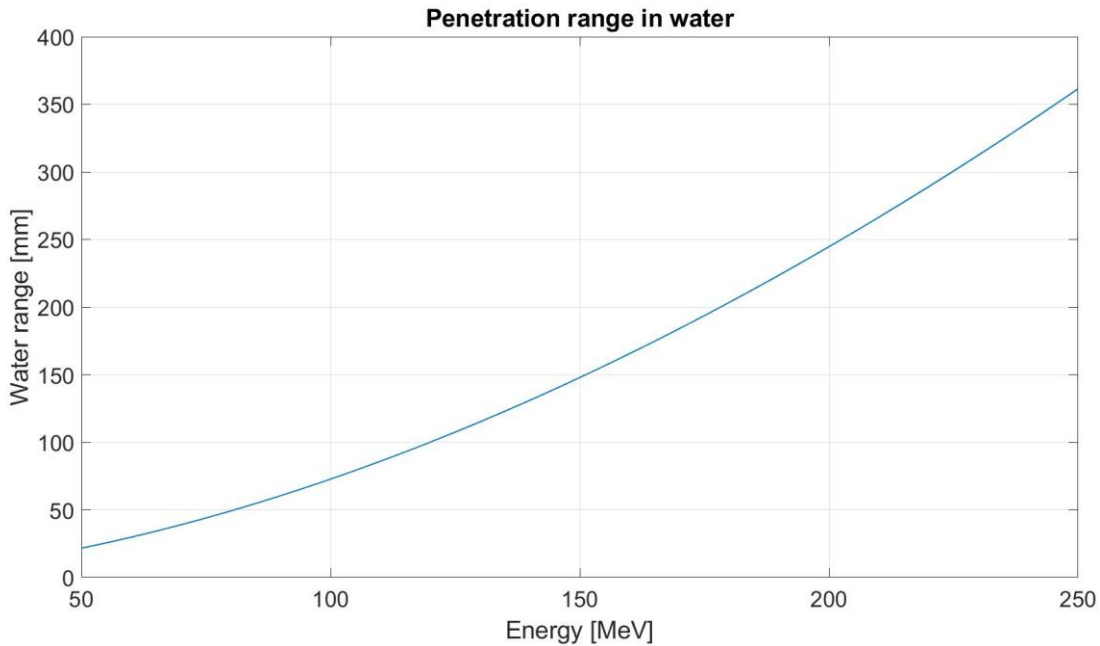


Figure 3.1: Penetration range of the proton beam through liquid water, function of the beam energy.

The clinically acceptable uncertainty on the measured range is 1 mm.

The measured range, obtained from the measured energy, is affected by the uncertainty over the measured TOF, which in turn derives from the uncertainties over the distances. To maintain the range within the limit imposed by the regulation, there is a maximum acceptable  $\sigma_{TOF}$ .

Figure 3.2 shows the profile of  $\sigma_{TOF}$  (normalized by the distance between the sensors), measured supposing 100 microns of uncertainty over the position of the detector, 0.5 MeV of uncertainty over the energy measured and a distance of 1 m between the two sensors. The maximum error over the

time of flight ranges from 4 to 50 ps per meter, and in the case of 228 MeV (i.e. the maximum clinical proton energy), it is equal to 4.5 ps.

The value of the acceptable  $\sigma_{TOF}$  decreases with an increase of the beam energy. Indeed, at high energies, the error over the TOF implies a bigger uncertainty over the penetration range, rather than small energies. Therefore, the required precision on the time of flight is smaller at bigger energies. However, by increasing the beam energy, it is worth noticing that the number of coincident peaks increases, improving the statistics, and reducing the statistical error.

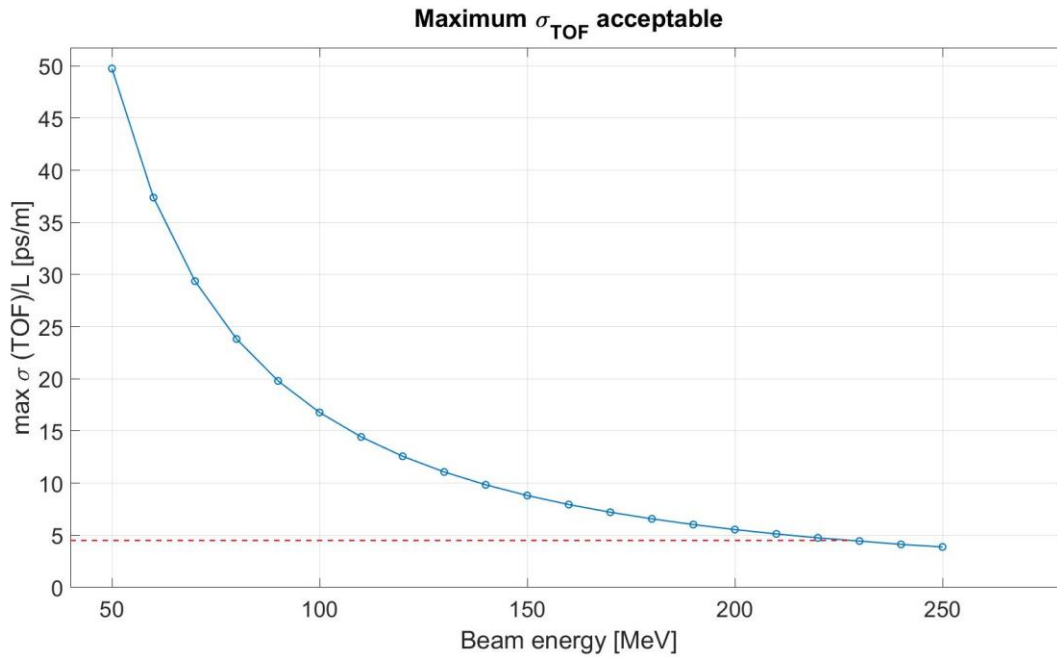


Figure 3.2: Maximum  $\sigma_{TOF}$  acceptable to keep the measured value of energy within the 1mm range in water limit imposed.

From the TOFs measured, the velocity, the kinetic energy and the range could be obtained as described in the following section 3.2.

Considering the setup used during the data acquisition (sec 2.2), the main sources of error are the systematic errors related to the distance between the sensors and to the time offset, due to the cables and digitizer. The structure that holds the detectors guarantees a precision of the order of tens of  $\mu\text{m}$ , but there is the possibility of a tilt of the detector. Therefore, the system must be calibrated in terms of distance and offset.

Two possible ways to calibrate the system have been investigated and will be described in the following sections. The first one relies on the knowledge of the values of the nominal energies, provided by the facilities (*absolute method*), while the second one, named *relative method*, is independent from the nominal energies values.

## 3.2 Energy measurement

Before going into the details of the calibration, some comments about the energy measurement must be provided.

Figure 3.3 shows the scheme of the device, where  $S_1$  is the first sensor,  $S_2$  is the second sensor,  $L$  is the distance between the two of them, and  $d$  is the thickness of the sensor.

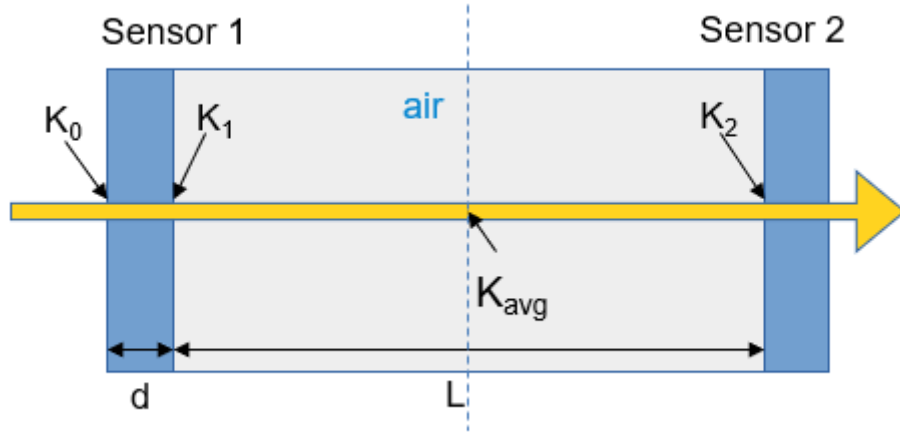


Figure 3.3: Naming the energy between  $S_2$  and  $S_1$ .  $K_0$  is the energy at the isocenter. The beam loses energy going through the first detector ( $K_1$ ) and through air, covering the distance  $L$ .  $K_2$  is the energy before the second detector, and  $K_{avg}$  is the average energy over that distance.

Knowing the distance ( $L$ ) and the time of flight ( $\Delta t$ ), the velocity goes as:

$$v_{avg} = \frac{L}{\Delta t} \quad (2.1)$$

In this specific case, because of the wires and the digitizer, there is a certain *offset* to be defined:

$$v_{avg} = \frac{L}{(TOF - offset)} \quad (2.1)$$

The goal is to find out  $K_1$  and  $K_0$  (the energy at the isocenter), knowing that there is a certain energy loss in the air and in the silicon. Because of the energy loss in silicon,  $K_1$  is lower than  $K_0$  and because of the energy loss in air,  $K_2$  is lower than  $K_1$ .

The dependency between velocity and kinetic energy is not linear. But, as demonstrated in Appendix B, in the small interval of energy loss (from  $K_0$  to  $K_2$ ), it can be approximated as linear. Therefore, it is possible to measure the average energy from the average velocity:

$$K_{avg} \cong E_0 \left( \frac{1}{\sqrt{1 - \left(\frac{v_{avg}}{c}\right)^2}} - 1 \right) \quad (3.2)$$

A Monte Carlo simulation shows that, having a really small loss of energy in the air,  $K_2$  is equal to:

$$K_2(L) \cong K_1 - \left(\frac{S_{air}}{\rho}\right)_{avg} \cdot \rho_{air} \cdot L \quad (3.3)$$

where the mass stopping power of the air is approximated as  $\left(\frac{S_{air}}{\rho}\right)_{avg} \cdot \rho$ . To estimate the average  $\left(\frac{S_{air}}{\rho}\right)_{avg}$ , the total mass stopping power, in the interval 50-230 MeV, has been measured from the

PSTAR database of the National Institute of Standards and Technology (NIST), for air and silicon, and fitted to the equation proposed by [25]:

$$\left(\frac{S_{air}}{\rho}\right)_{avg} = y_{air} + A_{air}K^{(-p_{air})}$$

with  $y, A$  and  $p$  (for silicon and air) that are obtained from the exponential fitting of the data. The equations to obtain the energy at the isocenter ( $K_0$ ) from the TOF evaluated between  $S_1$  and  $S_2$ , the distance between the sensors, and the *offset*, are summarized in the following:

$$v_{avg} = \frac{L}{TOF - offset} \quad (2.1)$$

$$K_{avg} \cong E_0 \left( \frac{1}{\sqrt{1 - \left(\frac{v_{avg}}{c}\right)^2}} - 1 \right) \quad (3.2)$$

$$K_1 = K_{avg} + (y_{air} + A_{air}K_{avg}^{(-p_{air})})_{air} \cdot \rho_{air} \cdot \frac{L}{2} \quad (3.4)$$

$$K_0 = K_1 + (y_{si} + A_{si}K_1^{(-p_{si})})_{si} \cdot \rho_{si} \cdot d \quad (3.5)$$

with Equation 3.4 that calculates the energy after the first sensor, considering the energy loss in air, and Equation 3.5, for the energy at the isocenter, considering the energy loss going through the first sensor.

### 3.3 Absolute method

For the *absolute approach*, assuming the nominal energies known, the system is calibrated through a  $\chi^2$  minimization (*minuit* function of ROOT [26]) using the measured TOFs. This method was adopted for the analysis of the first data acquired at CNAO, where the error on the energies values provided by the facilities (0.1 MeV) were by far smaller than the expected systematic error on the positions of the sensors. Therefore, this approach calibrates the system using the nominal energies as input, and the distances and time offset as results:

$$\chi^2(offset, d_j) = \sum_{i,j} \left\{ \frac{(TOF_{ij} - offset) - TOF(K_i, d_j)}{\sigma_{TOF_{ij}}} \right\}^2 \quad (3.6)$$

where  $K_i$  are the nominal energies corrected for the energy loss in the first detector and in air (explained in the previous section), while *offset* and distances ( $d_j$ ) are the free parameters of the minimization.

$$TOF(K_i, d_j) = \frac{(K_i + E_0)d_j}{c\sqrt{(K_i + E_0)^2 - m^2c^4}} \quad (3.7)$$

In Equation 3.7,  $E_0$  is the rest proton energy,  $c$  is the light speed and  $m$  is the proton mass. The process involves different values of  $d_j$  and *offset*, and the final results (four distances and time offset) are the ones that minimize  $\chi^2$ .

The distances and the time offset could be then used in Equation 2.1 to obtain the value of the unknown energies from the measured TOF values.

### 3.3.1 Results

Table 3.1 Results of the calibration of the system adopting the absolute approach, using the TOFs measured from the tests conducted at CNAO.

Parameter	Value	Error
d1 [mm]	65.8	0.032
d2 [mm]	364.13	0.039
d3 [mm]	665.05	0.042
d4 [mm]	965.24	0.046
offset [ps]	0.117	0.003

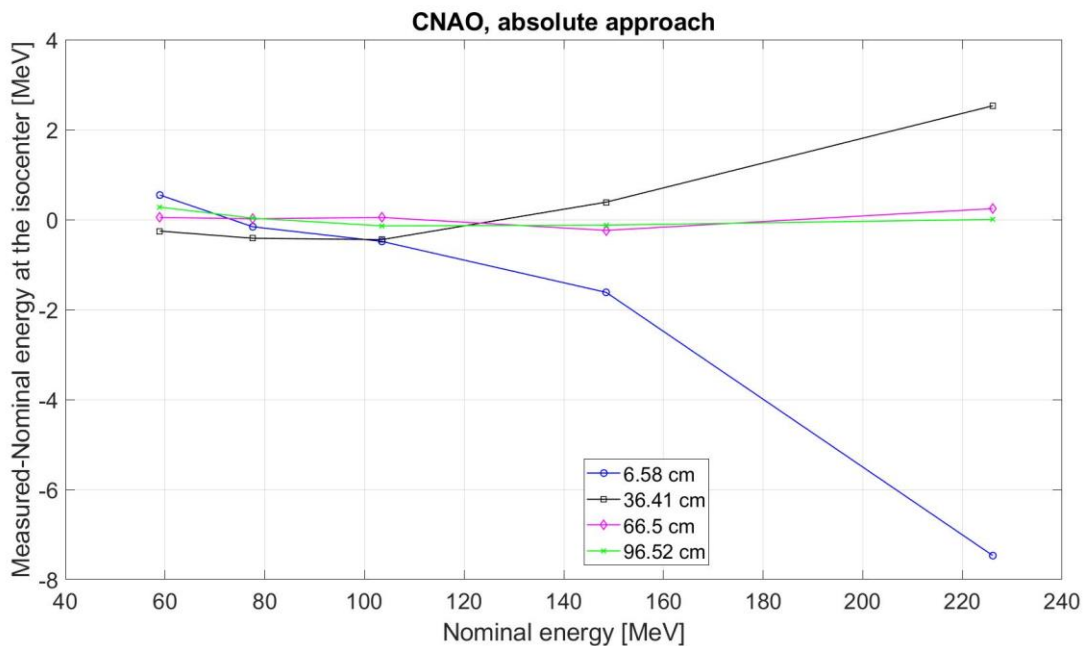


Figure 3.4: Difference between the measured and the nominal energy. The beam energy has been measured with the distances and the time offset resulting from the calibration of the system, adopting the absolute approach.  $\Delta E$  gets smaller increasing the distance.

Figure 3.4 shows the behavior of the difference between the measured and nominal energy at the isocenter (CNAO tests). As expected, the energy residual decreases with a grow of the distance between the detectors. In particular, for the last two positions involved in the acquisition (67 and 97 cm), the measured energy is very close to the nominal one.

From the energy, the penetration range in water can be measured and compared with the one coming from the nominal energies (Fig. 3.5).

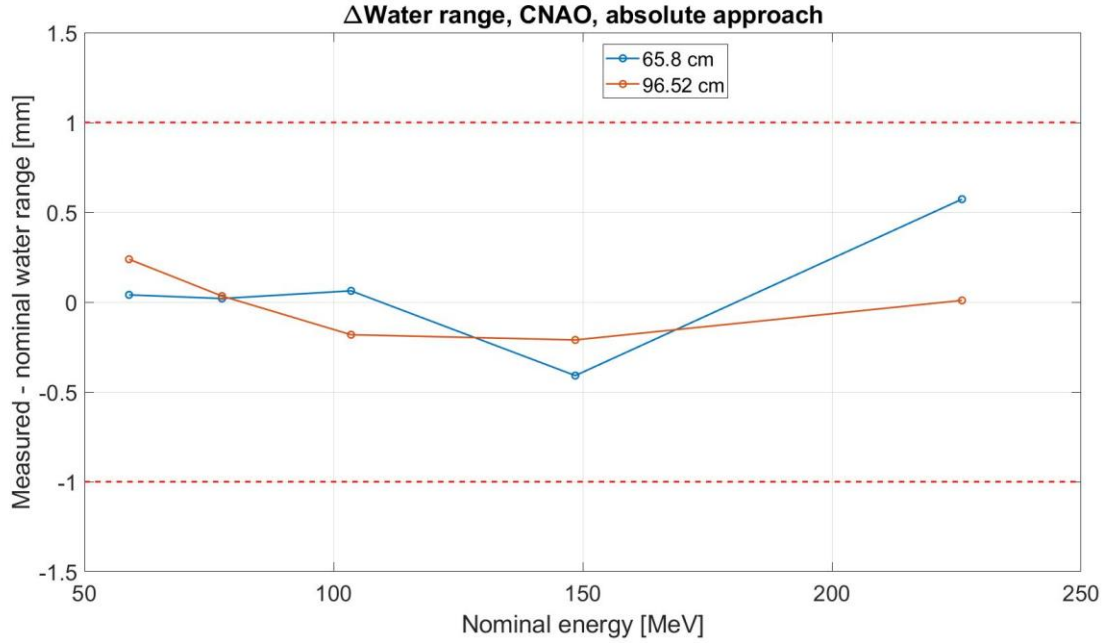


Figure 3.5:  $\Delta$ water range, from the measured (calibration with the absolute approach) and nominal energy, at the two bigger distances (67 and 97cm, nominal distances). All the points of the figure are within the limit of 1mm, imposed by the regulation, from the nominal range.

The difference is always in the interval  $[-1;1]$ , therefore the limit imposed by the regulation is satisfied.

### 3.4 Relative method

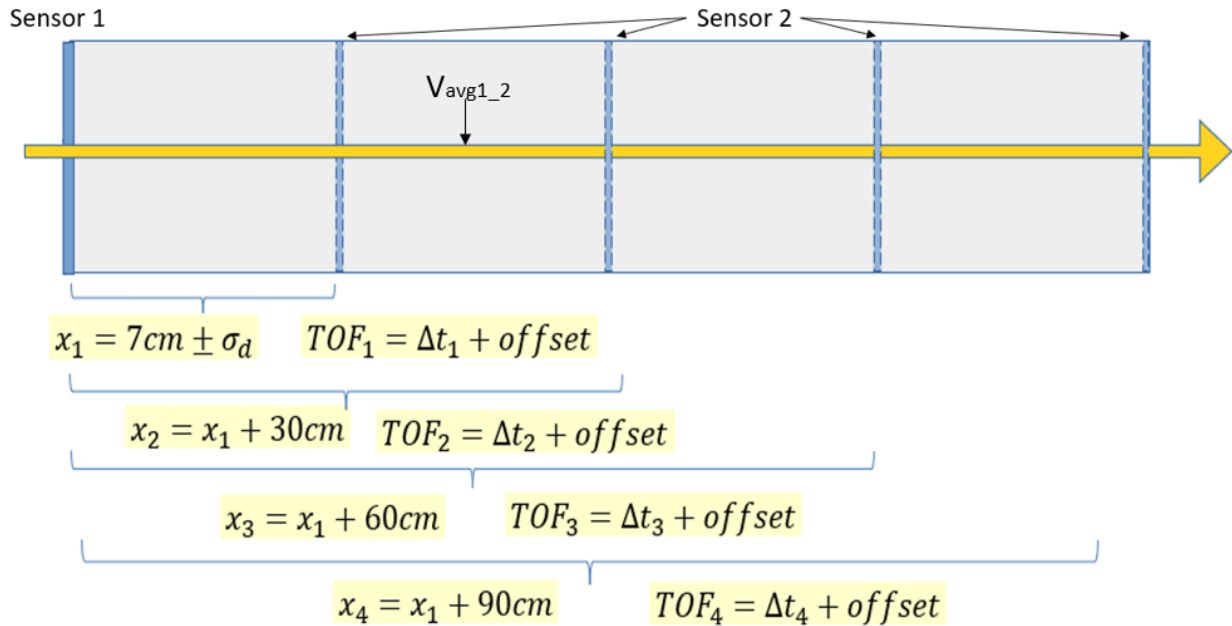


Figure 3.6: Schematic view of the mechanical device with the second sensor  $S_2$ , free to move from  $x_1$  to  $x_4$ . For any position has been measured the TOF, between  $S_2$  and  $S_1$ .  $V_{avg1_2}$  is the average velocity of the particles between two positions of  $S_2$ . TOF is the measured time of flight that is affected by a time offset, which can be positive or negative.

Figure 3.6 considers the setup of the tests conducted in CNAO (7,37,67 and 97 cm), with a constant  $\Delta x$  of 30 cm, but the same scheme could be adapted to the TPT tests.

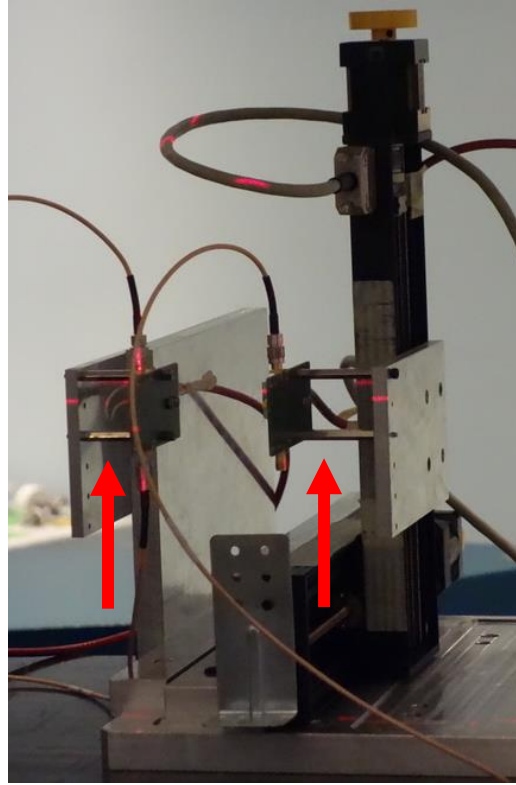


Figure 3.7: Picture of the prototype system used for the data acquisition. On the left-hand side there is the first detector ( $S_1$ ) and on the right-hand side the second detector ( $S_2$ ). The two are attached to a passive board, mounted on spacers (red arrows) and sustained by a rigid support. This structure leads to uncertainties over the positioning of the two sensors, in particular for  $x_1$ , first distance allowed by the mechanical system.

As already mentioned in chapter 2, it is worth reminding that the mechanical system of the TOF telescope used for the tests consists in a rigid support with 10 grooves for precise positioning of  $S_2$  at ten different distances from  $S_1$ , which is kept fixed (Fig. 3.7). As pointed out by the arrows in Figure 3.7, the boards with the sensors are mounted on spacers. This makes the first distance ( $x_1$ ) affected by a great uncertainty, while the  $\Delta x$ , i.e. the displacement among the first positions and the second, the third, etc..., are very well known, as they rely on the grooves of the rigid support.

The *relative approach* takes advantage of the different positions of  $S_2$ , that are all expressed as function of  $x_1$  plus the correspondent  $\Delta x$ , which is well known, to remove the dependence on the time offset from the equation of the average velocity (Eq. 2.1).

Every position of sensor 2 can be expressed as function of  $x_1$  (i.e.  $x_2 = x_1 + \Delta x$ ), assuming as known the  $\Delta x$  between the positions. These distances ( $x_2$ ,  $x_3$ , etc...) have been called measured distances, because they rely on the measured  $\Delta x$ . The velocity of the particles has been measured as:

$$v_{avg_{.12}} = \frac{x_2 - x_1}{TOF_2 - TOF_1} = \frac{(x_1 + 30cm) - x_1}{(\Delta t_2 + offset) - \Delta t_1 + offset} = \frac{30cm}{\Delta t_2 - \Delta t_1} = \frac{30cm}{(t_{2x_2} - t_1) - (t_{2x_1} - t_1)} \quad (3.8)$$

$$= \frac{30cm}{t_{2x_2} - t_{2x_1}}$$

where  $v_{avg_{.12}}$  is the average velocity of the particles at half distance between the two positions of  $S_2$ ,  $x_1$  and  $x_2$  (Fig. 3.6).

In general, this method tries to reduce as possible the number of nominal parameters provided as input to generalize the process. Because of this approach, the calibration method has only two free

parameters,  $x_1$  and the *offset*. This is the natural following step from the first method (*absolute* one), being independent from the nominal energies. Thinking about the new prototype system for the data acquisition and at the possibility to test it in different facilities, this method allows the energy estimation of the beam without introducing any nominal parameter in the analysis but relying only on the  $\Delta x$  between the positions of  $S_2$ .

The tests have been conducted at several positions and energies (4 positions and 5 energies in CNAO, 3 positions and different energies for each distance in TPT), and for each of them the TOF is measured using the method described in the previous chapter and implemented in the MATLAB application described in Appendix A. This calibration method has been developed using the TOF values measured at all the available positions (4 for CNAO and 3 for TPT) for 2 energies. The remaining energies were used to test the method. The ones in Table 3.2 are the TOFs measured from the tests conducted at CNAO.

Table 3.2: CNAO tests. For any distance of  $S_2$  there are 5 tests at different energies. In the third column, there is the measured TOF and the related error (fourth column).

Isocenter energy [MeV]	Distance $S_2$ - $S_1$ [cm]	TOF [ns]	TOF error [ps]
58.95	7	0.764	1.332
58.95	37	3.725	1.897
58.95	67	6.699	2.652
58.95	97	9.666	2.953
77.6	7	0.691	1.239
77.6	37	3.301	1.628
77.6	67	5.922	2.202
77.6	97	8.549	2.799
103.5	7	0.624	1.179
103.5	37	2.921	1.588
103.5	67	5.231	1.967
103.5	97	7.548	2.796
148.5	7	0.554	1.575
148.5	37	2.523	1.339
148.5	67	4.520	1.941
148.5	97	6.508	2.110
226.1	7	0.492	1.666
226.1	37	2.161	1.621
226.1	67	3.863	1.665
226.1	97	5.557	2.036

For each beam energy, any possible combination of the positions is considered (6 combinations per 1 energy, without repetitions). Considering two beam energies, this leads to 12 combinations.

$$\begin{aligned}
 \text{Energy}_1: & \quad v_{avg\_12}, v_{avg\_13}, v_{avg\_14}, v_{avg\_23}, v_{avg\_24}, v_{avg\_34} \\
 \text{Energy}_2: & \quad v_{avg\_12}, v_{avg\_13}, v_{avg\_14}, v_{avg\_23}, v_{avg\_24}, v_{avg\_34}
 \end{aligned}$$

For each combination of positions (like  $x_1$  and  $x_2$ ), taking the TOFs measured from two tests conducted at the same energy (like Energy<sub>1</sub>),  $v_{avg\_12}$  is the velocity measured at half distance between the two positions of S<sub>2</sub>. The energy in this point and the energy loss going from the first detector to this distance can be measured using Equation 3.2 and Equation 3.4, arriving to the energy right after the first detector,  $K_1$ .

For example, taking the tests conducted at 58.95 MeV,  $TOF_1$  and  $TOF_2$  are the time of flights measured at the first two positions, with  $x_2$  expressed as  $x_1 + \Delta x$ .

$$v_{avg\_12} = \frac{x_2 - x_1}{TOF_2 - TOF_1} \longrightarrow E_k \cong E_0 \left( \frac{1}{\sqrt{1 - \left(\frac{v_{avg}}{c}\right)^2}} - 1 \right) \longrightarrow K_1 = E_k + \left( \frac{S}{\rho} (K_{avg}) \right)_{air} \cdot \rho_{air} \cdot l$$

$E_k$  is the energy between the two positions of S<sub>2</sub>. It is measured with the same equation of  $K_{avg}$  (energy between S<sub>1</sub> and S<sub>2</sub>, Eq. 3.2). With  $l$  that stays as the distance between the first detector and the middle point between the two positions of S<sub>2</sub>.

The energy after the first sensor ( $K_1$ ) is equal to 58.93 MeV, and it should be equal for all the tests conducted at that energy (58.95 MeV), and it is used to measure the four distances of S<sub>2</sub>:

$$d = v (TOF - offset) \quad (3.9)$$

For each distance in Equation 3.9, the value of the average velocity between S<sub>1</sub> and that position of S<sub>2</sub> is calculated as:

$$v(K_{avg}) = c \sqrt{1 - \frac{E_0^2}{(E_0 + K_{avg})^2}} \quad (3.10)$$

with  $K_{avg}$ :

$$K_{avg}(L) \cong K_1 - \left( \frac{S}{\rho} (K_1) \right)_{air} \cdot \rho_{air} \cdot \frac{L}{2} \quad (3.4)$$

considering the proper L, expressed as  $x_1$  plus  $\Delta x$ .

In this way, the four distances,  $d_1, d_2, d_3$  and  $d_4$  can be measured. They are called calculated distances:

$$d_1(offset) = {}^{12}_K v_1 \Delta t_1 = {}^{12}_K v_1 (TOF_1 - offset)$$

$$d_2(offset) = {}^{12}_K v_1 (TOF_2 - offset)$$

$$d_3(offset) = {}^{12}_K v_1 (TOF_3 - offset)$$

$$d_4(offset) = {}^{12}_K v_1 (TOF_4 - offset)$$

with  ${}^{12}_K v_1$  that represents the velocity measured from  $K_{avg}$  (Eq. 3.10), coming from the combination of TOFs at  $x_1$  and  $x_2$ , and  $\Delta t$  is the real time of flight, removing the time offset. These calculated distances are then compared with the measured values, obtaining the residuals.

Summarizing, from one combination (of  $x_1$  and  $x_2$ ), four distances have been measured. Considering two energies (Energy<sub>1</sub> and Energy<sub>1</sub>) and 12 combinations of positions, there will be 48 distances computed, and 48 residuals could be summed.

Two different minimizations have been employed: Ordinary least squares (OLS) minimization, and weighted least squares (WLS), with the residuals that count for their error.

Weighted least squares

$${}_{K}^{1,2} res(x_1, offset) = \sum_{i=1}^4 \left( \frac{d_i - x_i}{\sigma_i} \right)^2 \quad (3.11)$$

Ordinary least squares

$${}_{K}^{1,2} res(x_1, offset) = \sum_{i=1}^4 (d_i - x_i)^2 \quad (3.12)$$

$$Res(x_1, offset) = \sum_{K_{min}}^{K_{max}} \sum_{m=1}^4 \sum_{n>m}^4 m_K^n res(x_1, offset) \quad (3.13)$$

This process will be repeated by varying  $x_1$  and *offset* within a defined range. At the end, there is a point in the multidimensional plane defined by the ranges of variability of the first distance and time offset, which identifies the combination of  $x_1$  and *offset* that minimizes the residual (weighted or not).

This approach calculates the residuals between the distances calculated from the measured TOF (as it will be detailed in the following) and the ones measured (as  $x_1$ ,  $x_2 = x_1 + \Delta x$ ,  $x_3 = x_2 + 2\Delta x$ , etc...) for each combination of  $x_1$  and *offset* of the chosen interval. The outcomes are  $x_1$  and *offset*, corresponding to the minimum value of the residual, with the other positions that are expressed as function of  $x_1$  plus a certain  $\Delta x$  (30 cm for CNAO, in TPT it is not constant).

### 3.4.1 Results

Applying the OLS and WLS minimization, using the beam energies defined in the Appendix C, the calibration can be performed (Fig. 3.8 and Fig. 3.9).

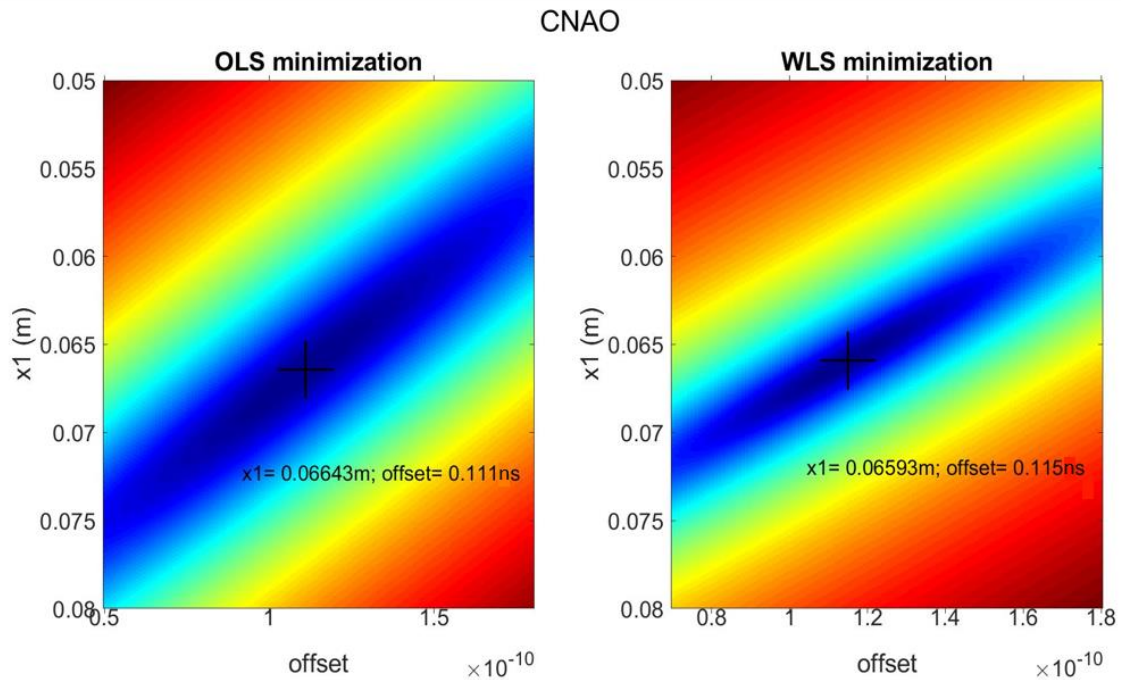


Figure 3.8: Results of the calibration, with the relative approach (OLS and WLS minimization), of the tests conducted at CNAO. From the  $x_1$  and time offset interval, there is a point that minimize the residual.

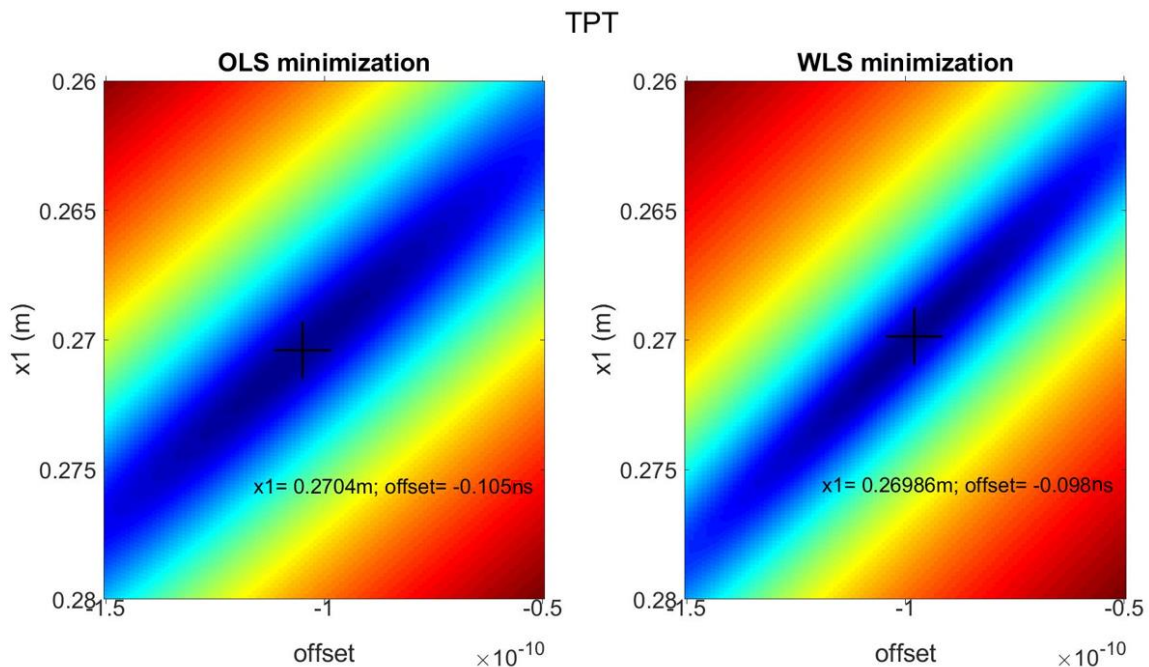


Figure 3.9: Results of the calibration, with the relative approach (OLS and WLS minimization), of the tests conducted at TPT. From the  $x_1$  and time offset interval, there is a point that minimize the residual.

Table 3.3: Results of the calibration for CNAO and TPT. The outcomes are the  $x_1$  [mm] and offset [ps].

	CNAO		TPT	
	OLS	WLS	OLS	WLS
<b><math>x_1</math> [mm]</b>	66.43	65.93	270.4	269.86
<b>offset [ps]</b>	111	115	-105	-98

All the results, in terms of first distance of  $S_2(x_1)$  and *offset*, free parameters of the calibration, are shown in Table 3.3. It is worth explaining that the time offset in TPT is negative because of an inversion of the cables during the testing.

As previously mentioned, with these results is now possible to measure the beam energy, with  $\Delta t$  (of Eq. 2.1), that takes into account the time offset, and the distance of the sensor  $S_2$  expressed  $x_1$  as plus a certain  $\Delta x$  that depends on its position. Because of the very small difference between what obtained with OLS and WLS minimization, also the energies are expected to be very close among them.

### 3.4.1.1 Pavia therapy center tests results

In CNAO,  $\Delta x$  is constant and equal to 30 cm.

For both approaches (OLS and WLS), the two free parameters can range between:

- $5 \text{ cm} < x_1 < 8 \text{ cm}$ ;
- $70 \text{ ps} < \text{offset} < 180 \text{ ps}$ .

The distances, function of  $x_1$ , are expressed as:

- $x_2 = x_1 + \Delta x$ ;
- $x_3 = x_1 + 2\Delta x$ ;
- $x_4 = x_1 + 3\Delta x$ .

Table 3.4 and Table 3.5 collects, respectively, the energies measured with the outcomes of the calibration of the system (CNAO tests), and the difference with respect to the nominal values.

Table 3.4: CNAO K0 energies. These represent the energy at the isocenter (right before S1), measured using  $x_1$  and offset from the OLS minimization.

OLS				WLS			
Distances [cm]				Distances [cm]			
6.64	36.64	66.64	96.64	6.59	36.59	66.59	96.59
Measured energies [MeV]				Measured energies [MeV]			
59.48	59.28	59.14	59.30	59.30	59.25	59.12	59.29
77.22	77.94	77.80	77.72	77.11	77.93	77.79	77.71
102.37	104.05	103.76	103.46	102.44	104.06	103.77	103.47
145.22	150.29	148.51	148.48	145.76	150.40	148.57	148.52
214.56	230.75	226.62	226.18	216.32	231.13	226.82	226.31

Table 3.5: Differences between nominal and measured energies at the isocenter (K0), with the OLS and WLS minimization.

Isocenter Energy [MeV]	OLS				WLS			
	Distances [cm]				Distances [cm]			
	6.64	36.64	66.64	96.64	6.59	36.59	66.59	96.59
	Energy difference [MeV]				Energy difference [MeV]			
58.95	0.53	0.33	0.19	0.35	0.35	0.30	0.17	0.34
77.6	-0.38	0.34	0.20	0.12	-0.49	0.33	0.19	0.11
103.5	-1.13	0.55	0.26	-0.04	-1.06	0.56	0.27	-0.04
148.5	-3.28	1.79	0.01	-0.02	-2.74	1.90	0.07	0.02
226.1	-11.54	4.65	0.52	0.08	-9.78	5.03	0.72	0.21

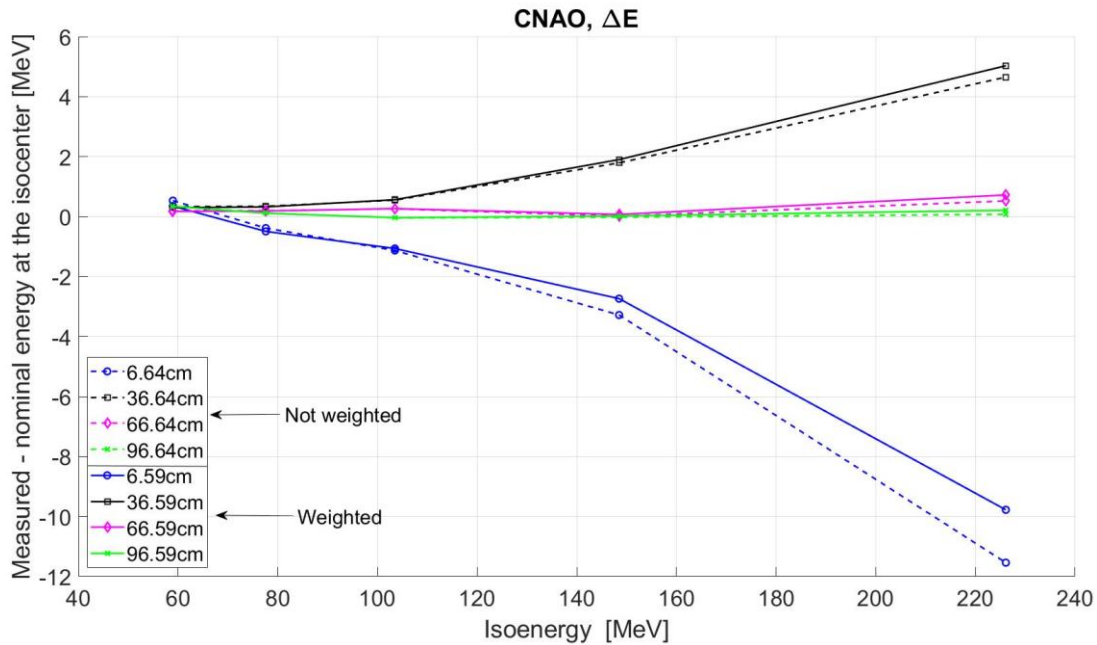


Figure 3.10: Difference between the measured energies (OLS and WLS minimization) and the nominal ones, at the isocenter. The four lines represent the behavior of  $\Delta E$ , according to the nominal energy, varying the distance of  $S_2$ . Continuous lines are the outcome of the WLS minimization, while the dashed lines are outcome of the OLS minimization. Increasing the distance there is an improvement of the results.

As expected, the behaviour of the  $\Delta E$  is pretty much the same for the two methods, and it decreases with bigger distances (Fig. 3.10). The results, for the OLS and WLS results, are pretty much the same. In the very first part of this chapter (Fig. 3.2), it was represented the maximum uncertainty over the TOF to keep the penetration range of the measured energy within 1mm from the range of the nominal energy. That figure (Fig. 3.2) shows the behaviour of  $\sigma_{TOF}$ , function of the energy, with a reduction of the acceptable error increasing the energy (a small difference in the energy, at high levels, leads to big changes in the penetration range). Figure 3.11 compares the obtained results, translated in terms of range, with the requirement on  $\sigma_{TOF}$ .

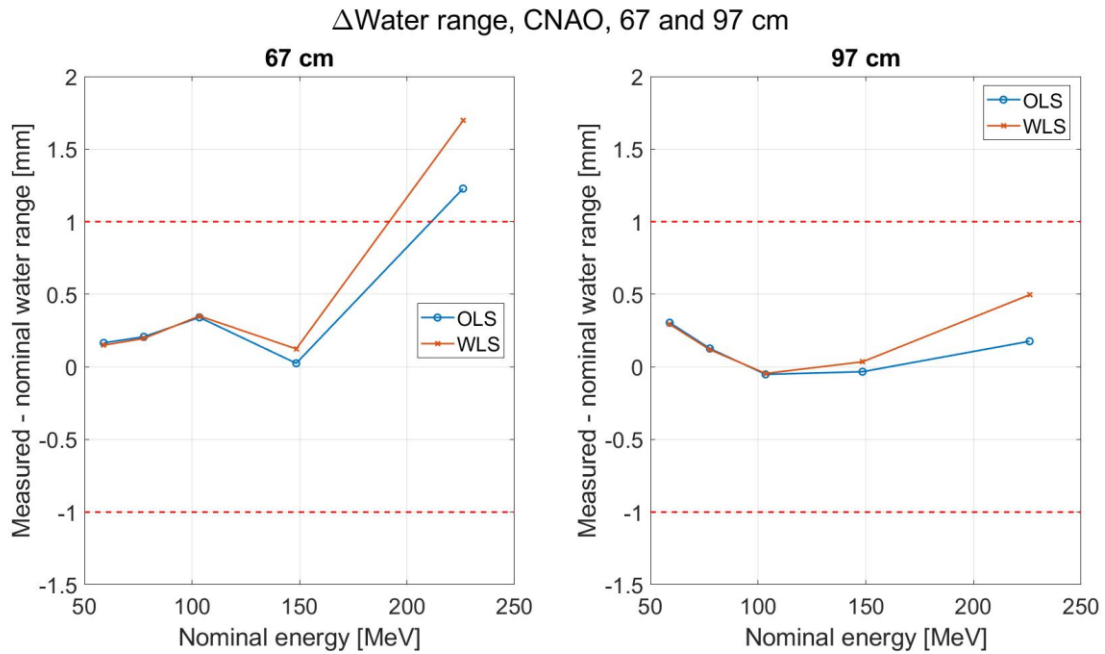


Figure 3.11: Difference of the water range (mm) measured from the nominal and measured energy, at 67 and 97cm (distance between  $S_2$  and  $S_1$ ), in CNAO. The two subplots report the results obtained through OLS and WLS minimization, respectively, blue and orange line.

The water range is always within the limit except for 228 MeV at 67 cm, while at 97 cm there are no issues at all. This makes sense, considering that, Figure 3.2 is normalized respect to the distance. The maximum acceptable error on the TOF (calculated in that case with multiple assumptions about the uncertainty of position and kinetic energy) decreases, decreasing the distance (Fig. 3.12). Even though, by decreasing the distance between the sensors the number of coincident peaks increases, improving the statistics and reducing the statistical error.

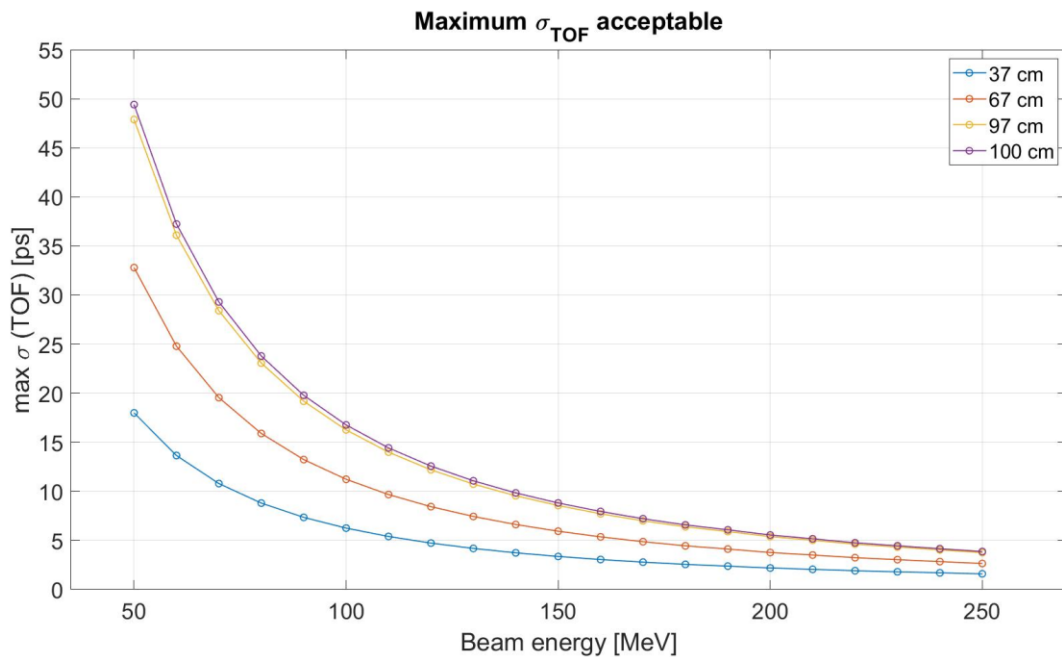


Figure 3.12: Evolution of the maximum error, over the TOF, acceptable to keep the water range within 1mm from the nominal one. The four lines describe the behavior of the maximum  $\sigma_{TOF}$  acceptable varying the distance (between  $S_2$  and  $S_1$ ). The TOF measured at small distances (more affected by uncertainties) must satisfy more tight requirements, while at bigger distances, having a mitigated effected of the uncertainties over the distance, the allowable error increases.

### 3.4.1.2 Trento therapy center tests results

The same structure of the CNAO results is proposed for TPT. The only difference between the tests performed at CNAO is related to the nominal distances: 27cm, 67cm and 97cm, and to the energies.

Table 3.6: Nominal energy at the three distances, TPT.

27 cm	67 cm	97 cm
68.3	68.3	68.3
98.5	97	97
147	-	147
-	163	163
182.7	182.7	182.7
-	222.8	222.8
227.3	227.3	227.3

For these two cases, the two free parameters can range between:

- $26 \text{ cm} < x_1 < 28 \text{ cm}$ ;
- $-50 \text{ ps} < \text{offset} < -150 \text{ ps}$ .

The distances, function of  $x_1$ , are expressed as:

- $x_2 = x_1 + 40 \text{ cm}$ ;
- $x_3 = x_1 + 70 \text{ cm}$ .

This time  $\Delta x$  is not constant.

Even though the method is exactly the same of the one applied to the tests of CNAO, it is worth mentioning that the nominal energies provided by TPT are affected by a greater error (around 0.5 MeV), as they are measured with the Giraffe detector [14].

Table 3.7 and Table 3.8 collects, respectively, the energies measured with the outcomes of the calibration of the system (TPT tests), and the difference with respect to the nominal values.

Table 3.7: TPT K0 energies. These represent the energy at the isocenter (right before SI), measured using  $x_1$  and offset from the OLS minimization.

OLS			WLS		
Distances [cm]			Distances [cm]		
27.04	67.04	97.04	26.98	66.98	96.98
Measured energies [MeV]			Measured energies [MeV]		
68.184	68.397	68.314	68.305	68.445	68.347
97.983	96.576	96.569	98.277	96.69	96.647
146.545	-	146.406	147.229	-	146.598
-	162.476	162.962	-	162.819	163.2
179.189	181.676	182.059	180.230	182.105	182.356
-	222.336	222.071	-	222.974	222.51
224.497	227.633	226.394	226.118	228.301	226.849

Table 3.8: Difference between measured energy and the nominal one, in TPT. At the smallest distance (27 cm), the second nominal level of energy is 98.5 MeV, instead of 97 MeV.

Isocenter Energy [MeV]	OLS			WLS		
	Distances [cm]			Distances [cm]		
	27.04	67.04	97.04	26.98	66.98	96.98
	Energy difference [MeV]			Energy difference [MeV]		
68.3	-0.116	0.970	0.014	0.005	0.145	0.047
97	-0.517	-0.424	-0.431	-0.223	-0.310	-0.353
147	-0.465	-	-0.594	0.229	-	-0.402
163	-	-0.524	-0.038	-	-0.181	0.200
182.7	-3.511	-1.024	-0.641	-2.470	-0.595	-0.344
222.8	-	-0.464	-0.729	-	0.174	-0.290
227.3	-2.803	0.333	-0.906	-1.182	1.010	-0.451

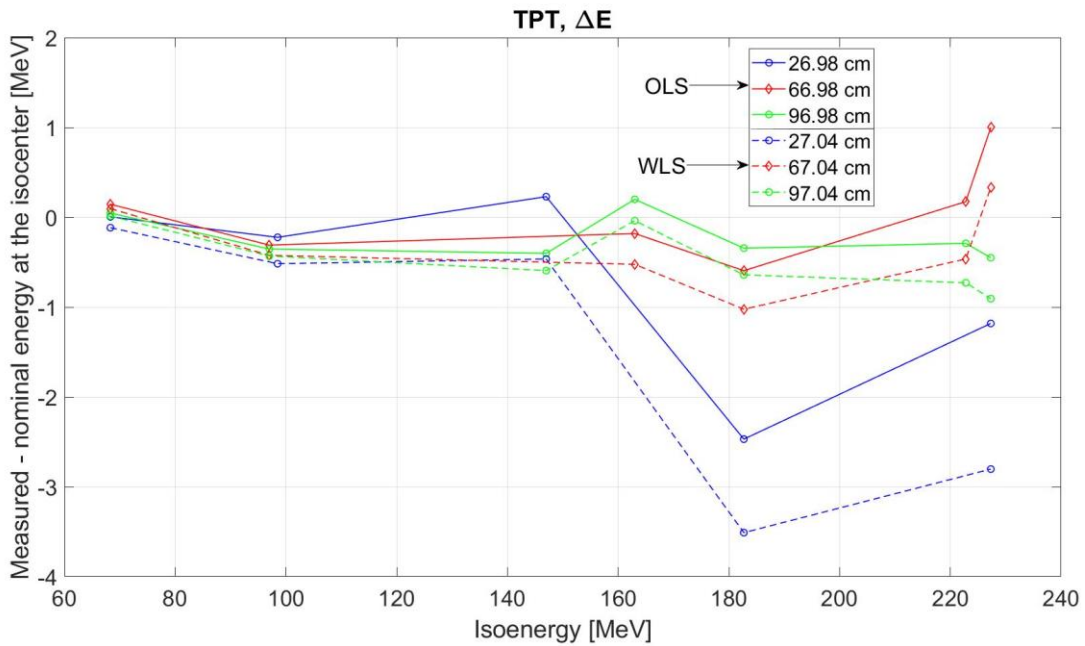


Figure 3.13: Comparison between OLS and WLS about the difference between measured and nominal energy.

As for CNAO, the trend is a decrease in the difference between the measured and the nominal energy, increasing the distance (Fig. 3.13). This time, though, the absolute value of these results is bigger. Therefore, the expected water range is supposed to be over 1mm for many points.

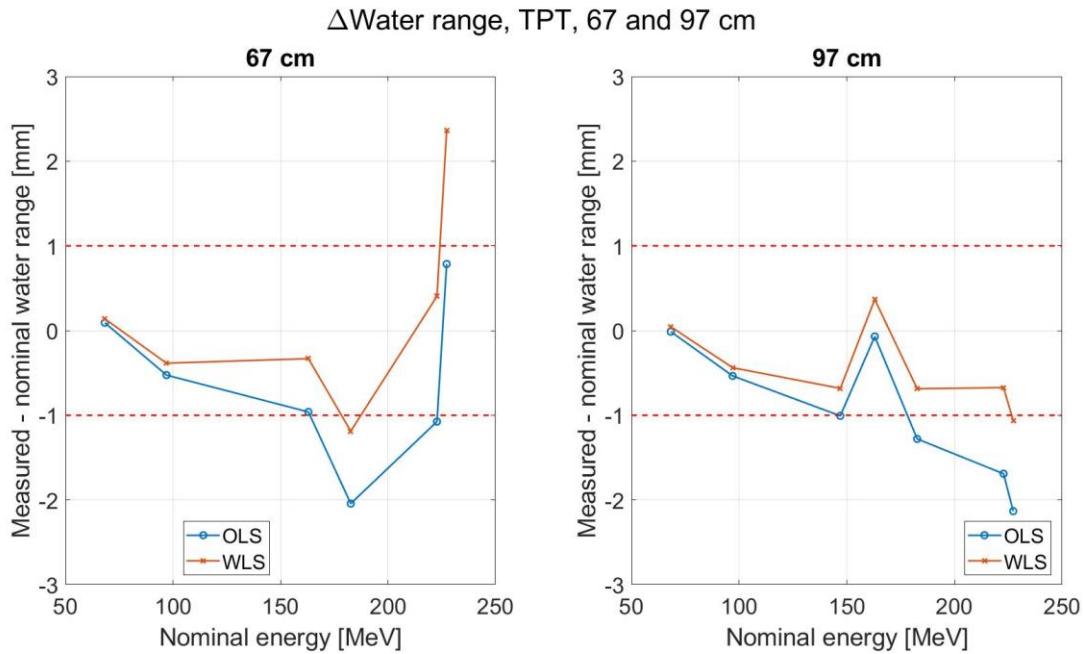


Figure 3.14: Difference of the water range (mm) calculated from the measured and nominal energies, at 67 and 97cm (distance between  $S_2$  and  $S_1$ ), in TPT. The two subplots report the results obtained through OLS and WLS minimization, respectively, blue and orange line.

There are several points outside the limit, at the two distances (Fig. 3.14). Even though, the results look better at 97 cm than 67 cm. There is no one clear winner method, between OLS and WLS minimization, but still, the important aspect is that, through each of them, it is possible to go back to the original energy of the beam with good results.

Despite the results, theoretically speaking, the weighted minimization should be more accurate than the other method because the residual is also weighted over its own error. This reduces the possibility of having a minimum inside the residual matrix (coming from the distance  $x_1$  and *offset* range imposed) that does not reflect the exact condition of the system and reduces the possibility of having different minimums to choose from.

The main future application of this device is the online measurement of the beam energy, so it is crucial to speed up every aspect of the whole analysis, for example reducing the data sets for *offset* and  $x_1$ , but at the same time keeping the precision of the analysis, reducing the probability of having wrong, or just not that accurate results. In this situation, the WLS minimization can make the difference with respect to the OLS one.

Main limit of this approach is that the code is not considering any error over  $x_1$  and *offset* coming from the minimization.

It is worth a comparison (Fig. 3.15) between the results of the *absolute* and *relative* (WLS) approach, at the maximum distance (97cm) of the CNAO tests.

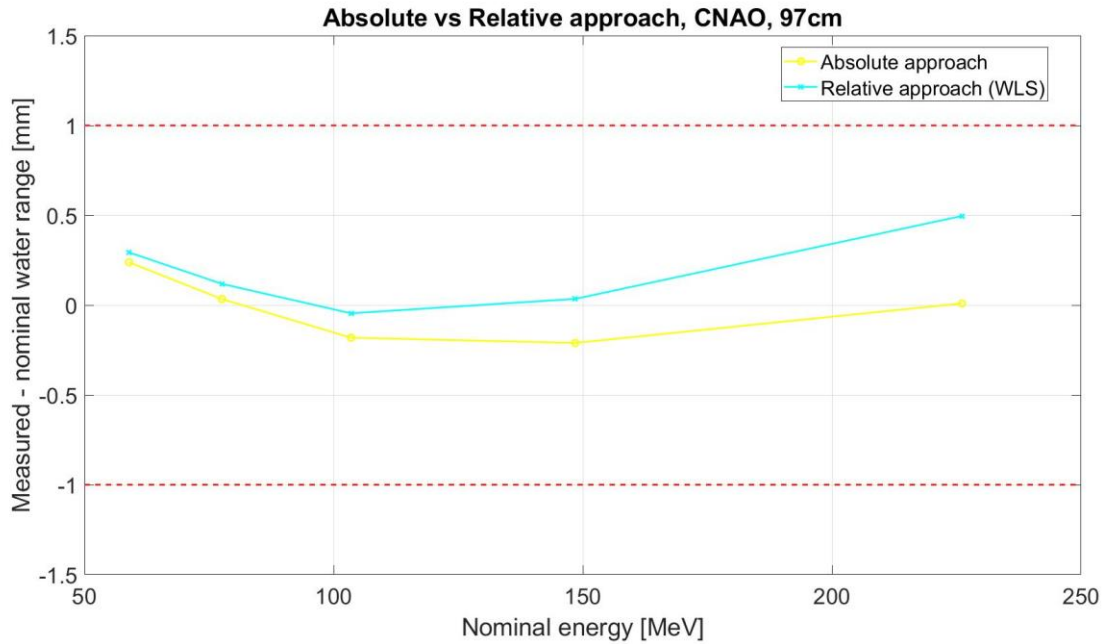


Figure 3.15: Comparison between the  $\Delta$ water range from the measured energies, adopting the two calibration methods: absolute approach (yellow line) and relative approach, WLS minimization, (blue line). All the points of the graph are in the limit of 1mm, but the ones coming from the absolute approach are, in general, closer to 0.

The *absolute approach* leads to better results rather than the *relative* one. Even though, as treated in the introduction, using the nominal energies is not the optimal way and it is far from the ultimate goal of the device that is, without inserting nominal parameters, the evaluation the beam energy. On the other side, the *relative approach*, whether if OLS or WLS minimization, with the uncertainties that are present over the TOF and the distance, is not always able to measure the energy with the required precision.

## 4. 16 strips simulation and analysis

### 4.1 Introduction

In the previous chapters, only 1 channel per sensor was considered.

Two different sensors have been used in CNAO (a sensor made of 4 pads of  $3 \times 3 \text{ mm}^2$  each) and in TPT (a sensor made of 11 strips of  $2 \text{ mm}^2$  each). The idea of going from the pad geometry to the strip one is related to the pileup issue. Discretizing the area, it is possible to reduce the probability of having the crossing of multiple particles within the sensor dead time. The strip sensor used in TPT is a sort of evolution of the one used in CNAO and has been specifically designed for this project. Because of the available readout boards, only 1 channel from the available channels (4 in the sensor used at CNAO and 11 in the sensors used at TPT) was readout in the tests performed.

A dedicated readout board is being designed to allow the reading of 8 strips in the final sensor (3 out of the 11 strips are test strip and will not be used on the beam). This will allow reducing the time needed to align the sensors and the acquisition time to collect the needed statistics, speeding up the process of the evaluation of the beam energy, but also to characterize the spread out of the flux.

The future acquisition of data at TPT or CNAO will involve 16 signals, 8 per detector, therefore the preparation of a tool able to extract the results from that amount of data is required, as well as for the first tests conducted it was necessary the preparation of the code described in the second chapter, once again developed using MATLAB 2018b.

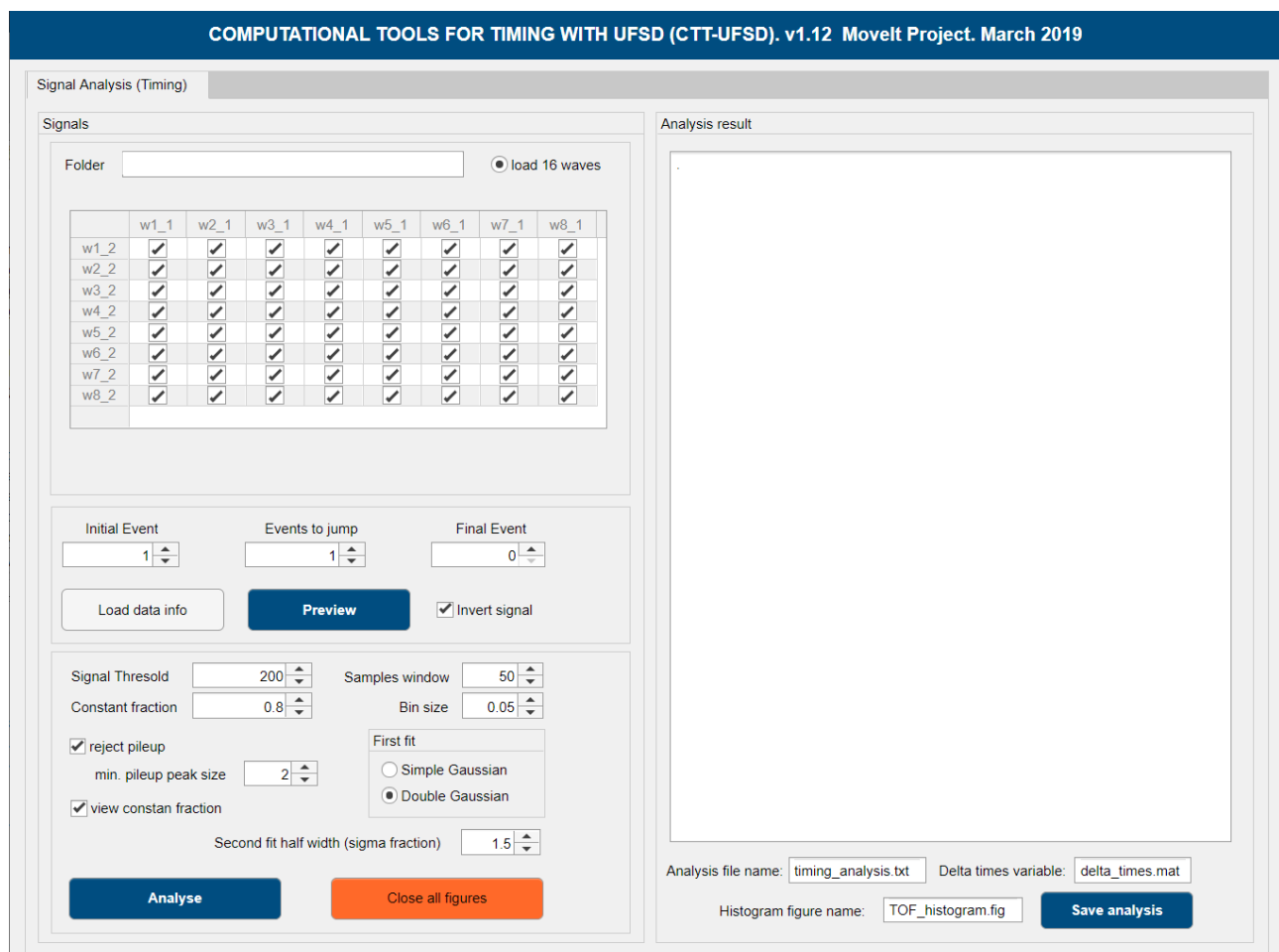


Figure 4.1: Interface of the TOF measurement app.

A MATLAB application (the user interface is shown in Fig. 4.1, explained more in detail in Appendix D) is being developed to allow measuring the time of flight of simulated or experimentally acquired data from 8 channels per sensor. This application allows considering not just the strips that are one in front of the other, but all of them. Therefore, any possible coincidence is captured. For example, checking all the boxes on the main diagonal is a way to limit the analysis to the facing strips only, or by checking all of them, any possible combination is taken into consideration, like one proton that crossing the second strip of the first sensor arrives to the ninth strip of the second sensor. The application has been conceived to allow the off-line analysis of the data coming from the test facilities, and, hopefully, for the online measurements during future tests. Another MATLAB app has been developed to produce the simulated data needed (Fig. 4.2, Appendix E) to develop and validate the app for the analysis of the 16 channels. In this chapter there is a description of the methods developed and implemented in both apps, even though, the code for the analysis of the signals is pretty much the same of the one of the second chapter. Different analysis will be conducted trying to define the best setup for the measurement app (taking all the combinations together, facing strips and strip-by-strip analysis), and applying the two methods for the coincidences treatment, *3-sigma method* and *second gaussian method*. Then, there is a short analysis about the use of the measurement app to evaluate a possible misalignment of the detectors and a validation of the calibration method explained in the third chapter.

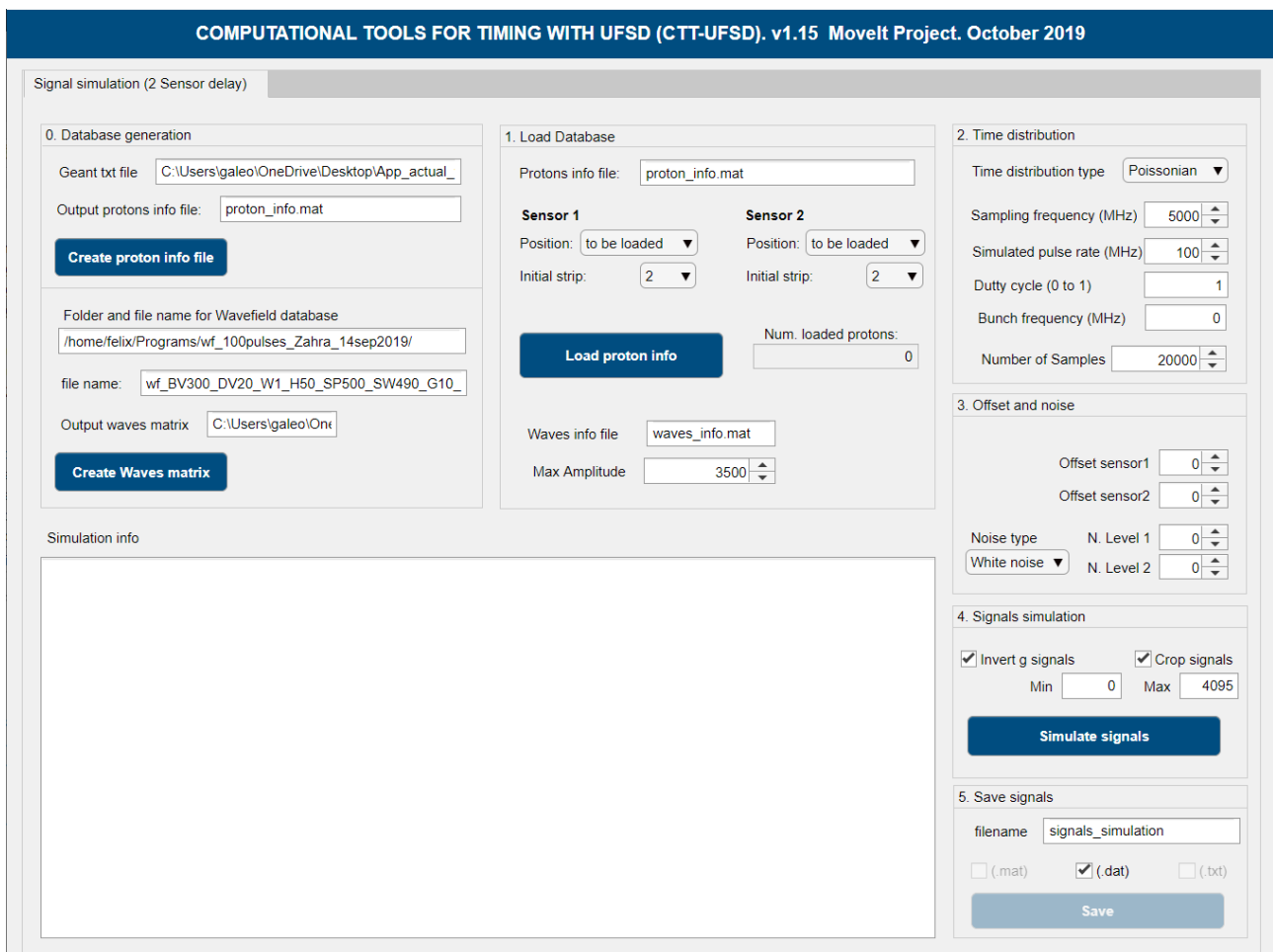


Figure 4.2: Interface of the TOF simulation app.

## 4.2 Signal simulation

To build the 16 strips simulation app there are some files required: the simulation coming from Geant4 [27] and the shape of the peaks from Weightfield2 [28]. In the following sections there is a description of the inputs (Geant4 and Weightfield2 simulations) required by the simulation app.

### 4.2.1 Geant4 simulation

The first input required for the signal simulation app is the simulation coming from Geant4, performed at different beam energies (62, 150, 227 MeV) and 15 positions: from 0.1 mm up to 1000 mm, with a specific distribution of the flux (a gaussian centered in 0,0) and a fixed number of protons: 2 million. These positions are required to simulate the distance between  $S_1$  and  $S_2$ . In 0 is positioned the first detector (total thickness of  $100\mu\text{m}$ ), to simulate the energy loss through silicon. Then, the information about the protons, at each position, is acquired by the so-called, *sensitive detectors*, of the same dimension of the detector. This has been made to not compromise the energy, and the path, of the particles of the simulation. By imposing the presence of a real detector in each position the beam would be deflected.

At the end of the simulation there should be a .txt file containing all the information for each proton (or any other particle generated by the interaction between protons and detector).

In the .txt file, there is the particle ID (a number that identifies each specific particle), the coordinates (x, y and z) at which it is crossing the detector, energy and time of flight required to cover that distance from the position 0.

The three coordinates are:

- z, the distance from the origin;
- y, the position over the height of the detector;
- x, the position over the width of the detector.

The coordinates x and y represent the position of the proton at that specific z, so knowing the dimension of the detectors described in the simulation, in a symmetric position with respect to the origin, it is possible to establish in which strip the particle is going through. There is, of course, the possibility of having values of x and y that do not fall within the dimension of the detector, representing particles that are not crossing the sensor. The event number of the proton, together with the strip and time of flight per each position are collected within a matrix, that is the actual input of the simulation app.

Figure 4.3 represents the path of just few protons, coming from the Geant simulation.

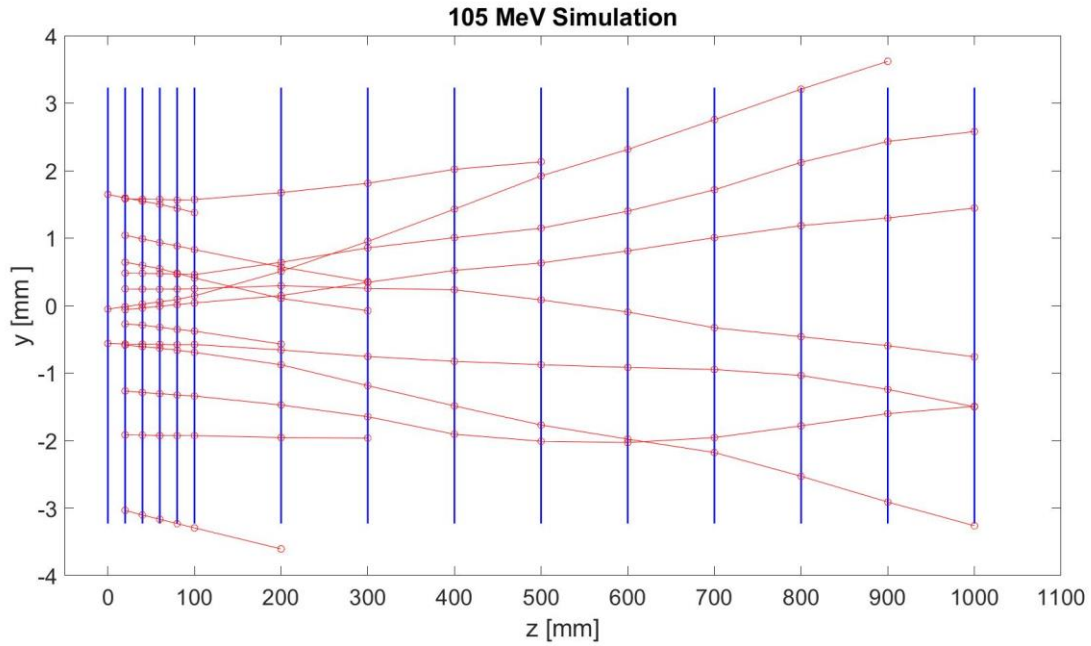


Figure 4.3: 105 MeV simulated protons (red lines) going through detectors at 15 positions (blue vertical lines). The z-axis represents the distance of the detector from the isocenter, at 0. While the y-axis goes over the height of the detectors. This is an example of one of the simulation conducted in Geant4.

#### 4.2.2 Weightfield2 simulation

The other input information is related to the shape of the peaks, as generated by the sensor. A set of 1000 peaks have been generated, for this analysis, with a duration of 2 ns, as the ones of the experimental tests conducted (chapter 2).

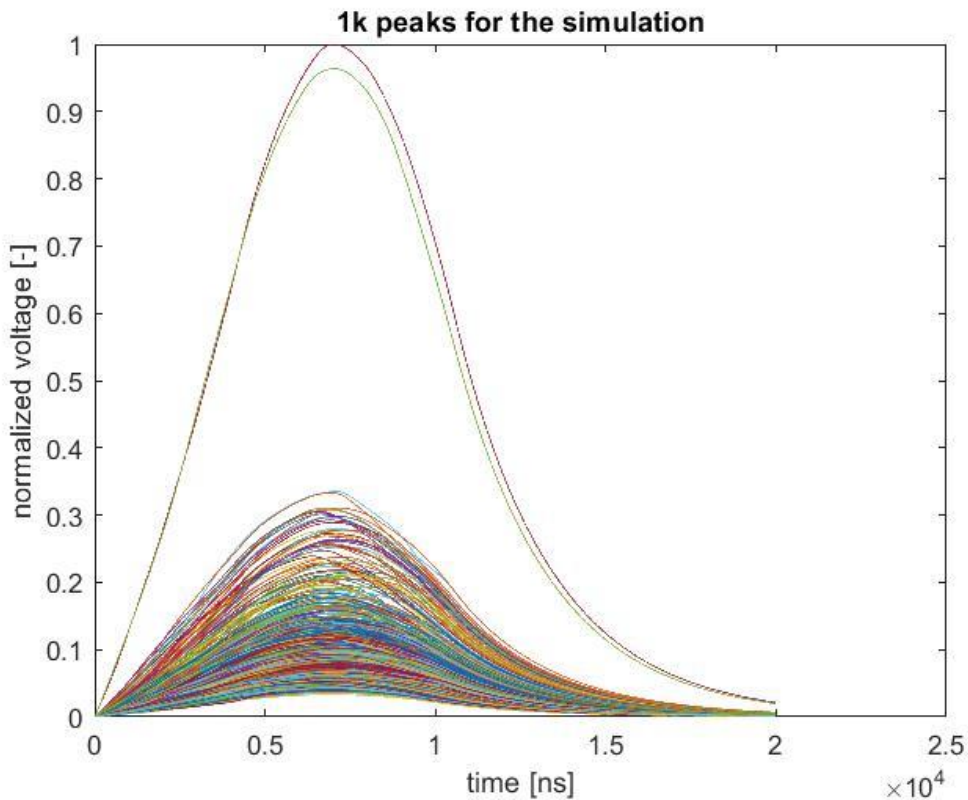


Figure 4.4: 1 thousand simulated peaks with Weightfield2, normalized respect to the maximum amplitude.

Figure 4.4 shows 1 thousand peaks, normalized over the maximum amplitude, extracted from a wider range of 20 ns interval of observation. There is a certain range of amplitudes, with the chance of having some peaks way bigger than the average. This may lead to some problems in the signals simulation, therefore they must go through a proper process.

From the maximum amplitude of each peak a histogram can be generated (Fig. 4.5).

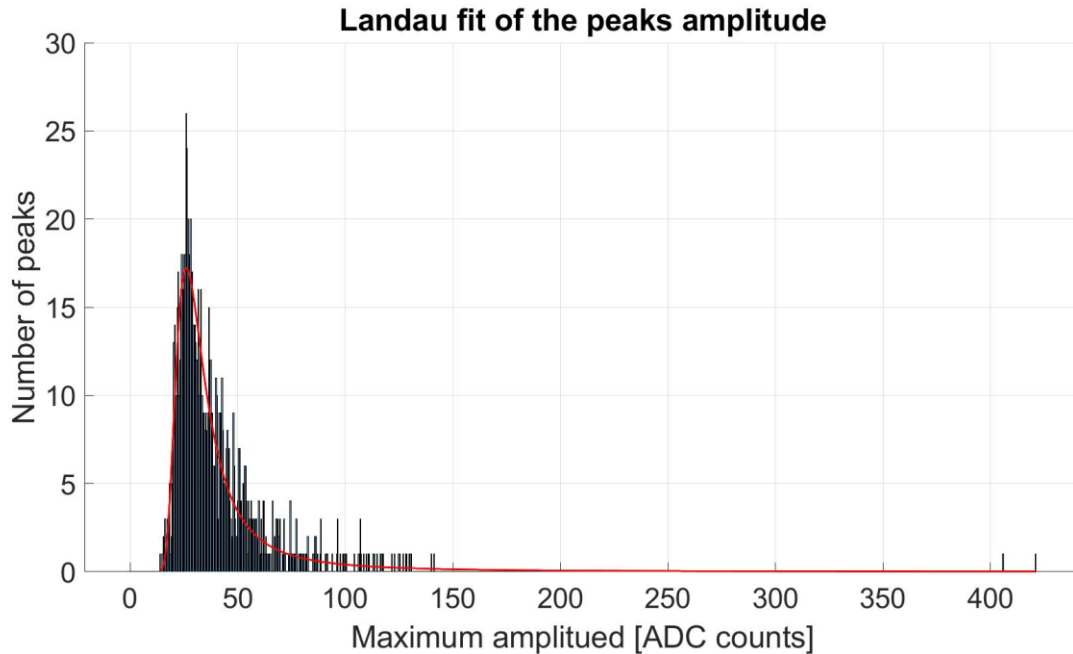


Figure 4.5: Histogram collecting the amplitude of each simulated peak (Fig. 3.4). The red line is the Landau fit of these points.

Fitting to a Landau, it is possible to obtain the most probable value (MPV, 26 ADC counts). All the peaks are normalized with respect to the MPV. Therefore, from the app interface, the mean amplitude of the peak can be set up, and it is multiplied times these normalized peaks, preserving the shape of the peak and allowing to simulate peaks of different amplitude. Without this process (normalizing all the generated peaks with respect to the maximum amplitude), there would be the possibility of having peaks too small. Not even sufficiently high to overcome the threshold.

### 4.2.3 Simulation method

At this point is possible to proceed with the signals simulation, that takes all the parameters from the app interface, such as noise, sample rate, number of samples etc., the required inputs from the Geant4 and Weightfield2 simulations, and generates the signals, then evaluated with the measurement app. The base of the process is the generation of a vector, following the Poisson distribution, in which the time interval between two successive peaks is reported, expressed in samples (Fig. 4.6). This simulates the signal of the first detector.

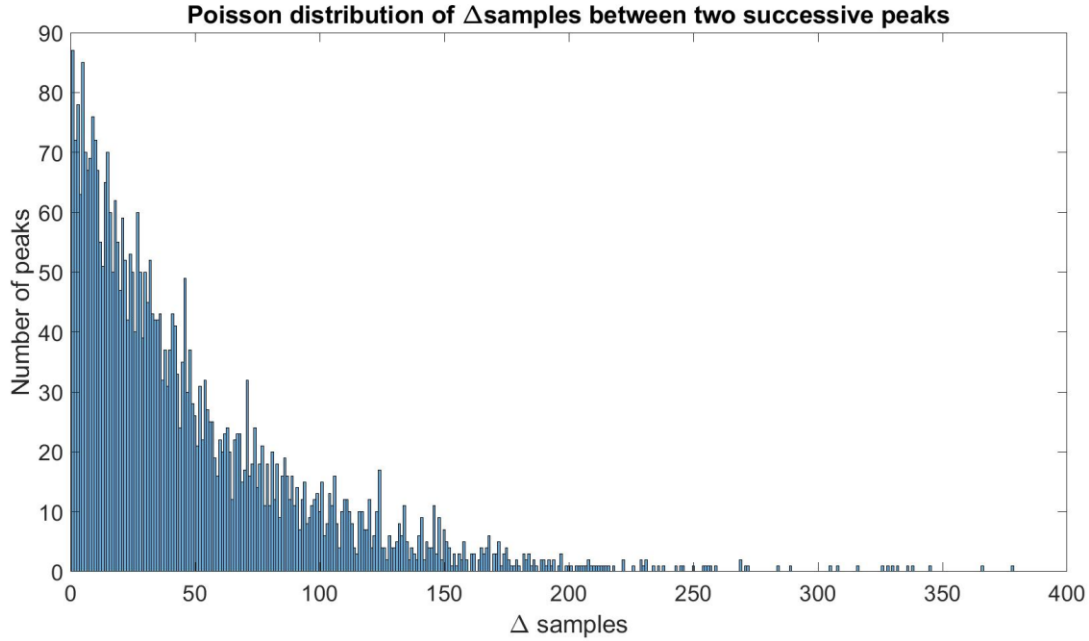


Figure 4.6:  $\Delta$ samples, for a pulse rate of 100 MHz, 5000 MHz of sampling frequency and 200000 samples.

This vector has a length that depends on the parameter set up from the app interface, and it is equal to the number of pulses, decided by the pulse frequency, number of samples and on the sampling frequency:

$$\text{Number of pulses} = \frac{\text{Frequency}_{pulses} \cdot \text{Number}_{samples}}{\text{Frequency}_{sampling}}$$

with:

- Pulse frequency, in MHz, consider the number of pulses per unit of time;
- Number of samples is related to the number of events acquired (1 event is equal to 1024 samples). So, in general, this parameter describes how much it lasts the simulated acquisition;
- Sampling frequency is the number of samples per second. In this case, trying to simulate the acquisition of the digitizer (any 0.2 ns), the sampling frequency must be 5000 MHz. In general, this parameter is involved in the discretization of a continuous signal.

Knowing the time intervals between two successive peaks, it is possible to determine the arrival time of each peak of the first sensor, generating the vector that is the base of the simulation with a length defined as the cumulative sum of all these arrival times (*cumsum* function of MATLAB). All this information, in terms of arrival time, duration of the peak, and time interval between two successive peaks, are translated into a vector (*waveform*). This vector is initialized to 0. Every time there is a peak, in a certain number of positions of the vector, related to the duration of the peak (10 samples, as default), is added 1. The first index of this series of 1 is individuated from the arrival time of each peak. In case of two or more peaks overlapped (pileup), in those positions 1 is added per each peak considered.

To simulate the conditions of the signals experimentally acquired in CNAO and TPT (mostly related to the type of accelerator, as discussed in chapter 2), this *waveform* vector, containing the information about the time disposition of the peaks can be generated in a continuous way (CNAO) or in a bunched structure (TPT), with the bunch frequency, in MHz, that can be modified on the app interface.

Therefore, the entire simulation process is contained inside a loop that scroll over this *waveform* vector. Any time there is a 1 (or 2, or more), the code goes inside the matrix coming from the Geant4 simulation and takes the strips at which the proton (or protons, according to the number inside the vector) is crossing the detector in those positions (set up at the beginning of the process), and the

times of flight. The peaks are generated in the signals of the crossing strips. For the next incoming proton (from the *waveform* vector), the code takes the next row of the matrix. The shape of this peak comes from the 1000 peaks, generated with Weighfield2.

To simulate the digitizer acquisition, the total number of samples, decided on the user interface, is divided times 1024 (1 event, for the digitizer) and rounded. This time, instead of having 2 signals per 1 event (1 strip per detector, chapter 2), there are 16 signals per 1 event (8 strips per detector), like in Fig. 4.7.

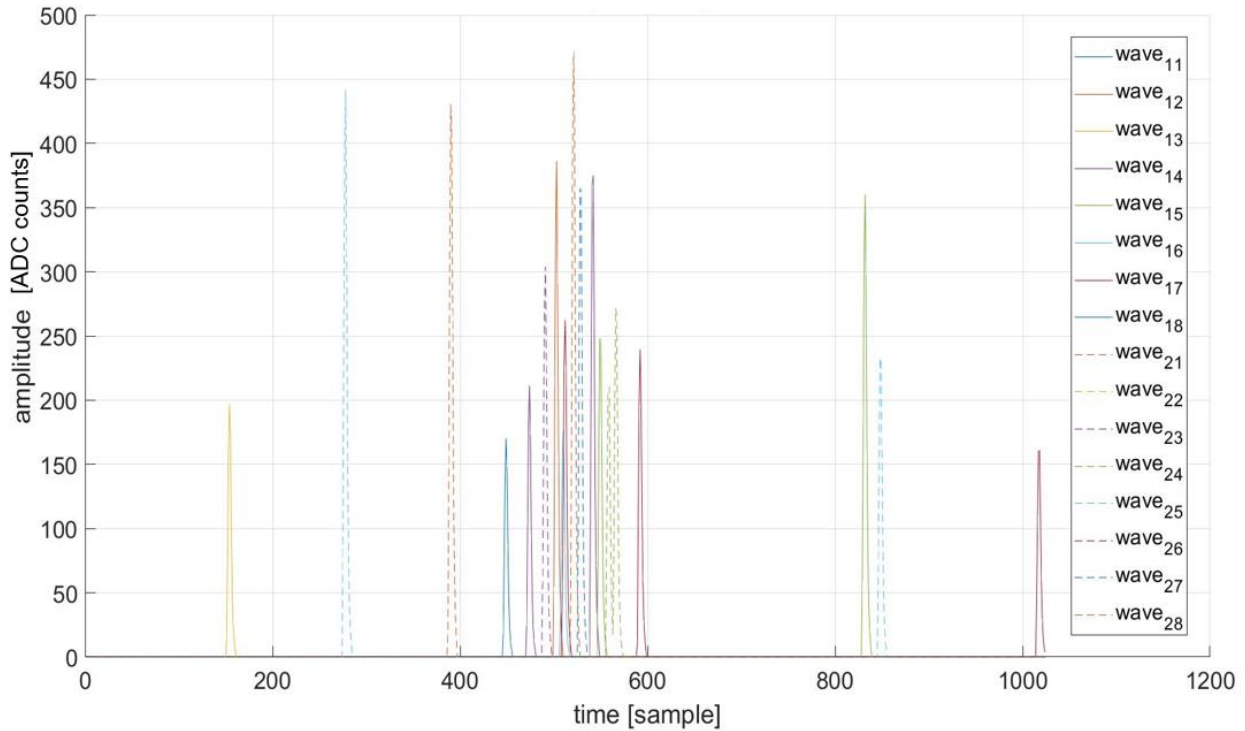


Figure 4.7: One event (1024 samples) of the simulation at 227 MeV. The two detectors are in positions: 0.1 mm and 600 mm.

At the end of the simulation, according to the parameters reported above (pulse rate and number of samples), a certain quantity of the protons coming from the simulation has been used. If, because of the parameters set up, the simulation requires a number of particles bigger than the one simulated, it stops once the whole Geant4 matrix has been used. The coincidences and the TOF between the strips of the two detectors of the simulation are assumed to be the reference value to compare the results of the measurement app.

The TOF measured from the simulation consider any possible combination between the strips of the first and second sensor. Any time the code recognizes a coincident signal, stores the correspondent time of flight in a matrix, 8x8. The rows of this matrix represent the strips of the first detector, the columns represent the strips of the second one. The final time of flight can be measured putting together all these values together (and divided over the total number of coincidences), or it can be measured box-by-box (strip-by-strip analysis). The latter takes the sum of all the TOFs stored over the coincidences for that combination. For example, from the simulation at 227 MeV, with S<sub>1</sub> and S<sub>2</sub>, respectively, at 0.1 and 600mm, the coincidences profile is represented by Fig. 4.8.

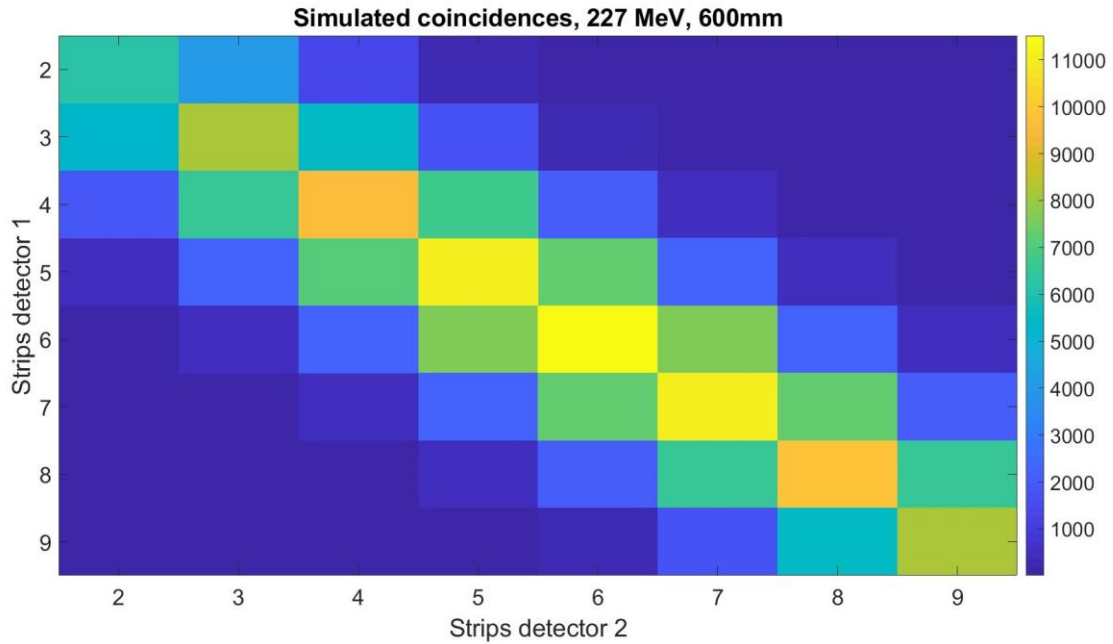


Figure 4.8: Simulated coincidences at 227 MeV, with  $S_1$  and  $S_2$  respectively at 0.1 mm and 600 mm. On the y-axis there are the strips of the first sensor, and x-axis the strips of the second sensor. On the main diagonal there are the facing strips combinations.

In Figure 4.8, as expected, the regions over the main diagonal experiences a bigger number of coincidences (on the main diagonal there are the facing strips), that decreases going to the peripheral area. Meaning that, the probability of going through a specific strip of the first sensor and reaching the same strip on the second sensor is much bigger than having a certain deflection and goes somewhere else. As an evidence of this kind of behavior, considering the upper right and lower left edge of the picture, there are less than 10 combinations each (they represent, respectively, strip2-strip9 and vice versa), while going closer to the main diagonal there is a quite rapid increase of the number of coincidences. Another pattern that can be noticed is directly on the main diagonal.

The flux generated by the simulation has the shape of a narrow gaussian centered over a detector of 11 strips (Fig. 4.9). Therefore, the maximum number of coincidences is expected on the combination over the strip 6 of the two sensors. In this case, because of the experimental nature of the strip 1, 10 and 11, it has been examined the behavior of the strips going from 2 up to 9, leading to a non-symmetric profile of the number of coincidences that are obtained.

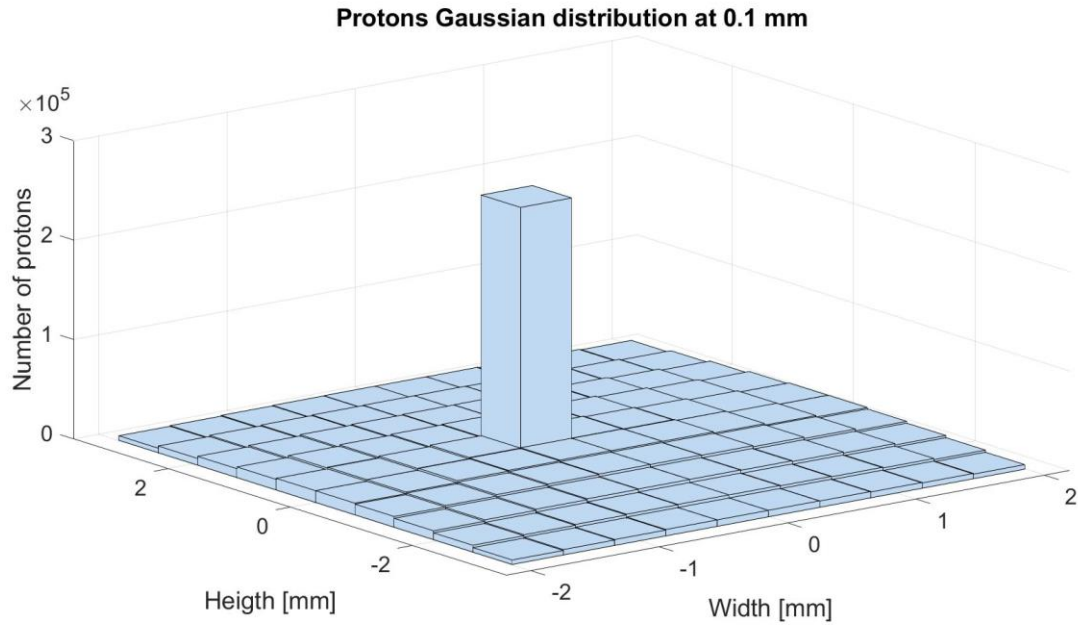


Figure 4.9: Gaussian distribution of the protons at 0.1 mm from the nozzle. The histogram collects how many protons are going through that specific region of the detector, without considering the strips arrangement.

For each combination of strips, the TOF is reported (Fig. 4.10). It is measured as the sum of all the TOFs stored over the number of coincidences detected (per each combination).

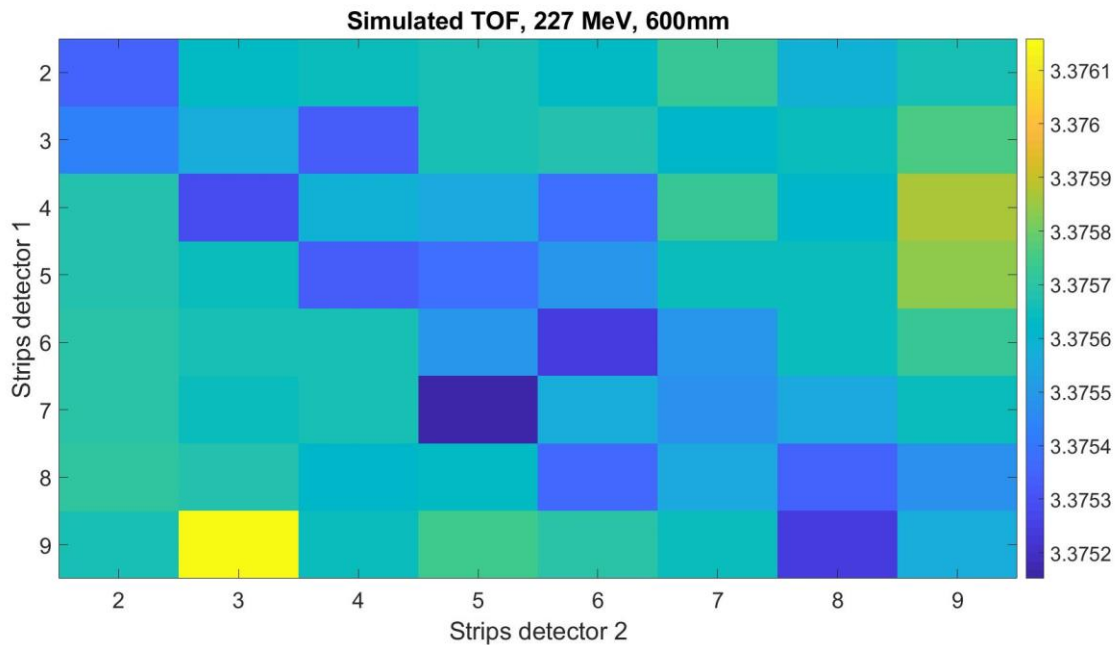


Figure 4.10: Simulated TOF, at 227 MeV, with  $S_1$  at 0.1 mm and  $S_2$  at 600 mm.

The oscillation in the value of the time of flight is very small (Fig. 4.10). The minimum value is 3.3752 ns and the maximum value is 3.3761, with a range of 0.9 ps. The mean TOF comes as the sum of all the TOFs stored, for any combination, over the total number of coincidences detected. This TOF, now, must be compared with the one coming from the analysis.

### 4.3 Time of flight measurement recap

The simulation stores the 16 signals (8 per detector) inside binary files reproducing the functioning of the digitizer (each strips of the two sensor generates a .dat file). As result, the analysis application treats these files, in input, as if they were directly produced by the experimental acquisition in one of the two mentioned facilities.

Like in the second chapter, the functioning of the code, about how to treat the signals, is basically the same. It goes through the signals of the first detector, and once a peak is detected, open a window of a certain number of samples (decided by the user on the app interface), and check if there are peaks in any other strip of the second detector, and eventually it stores them.

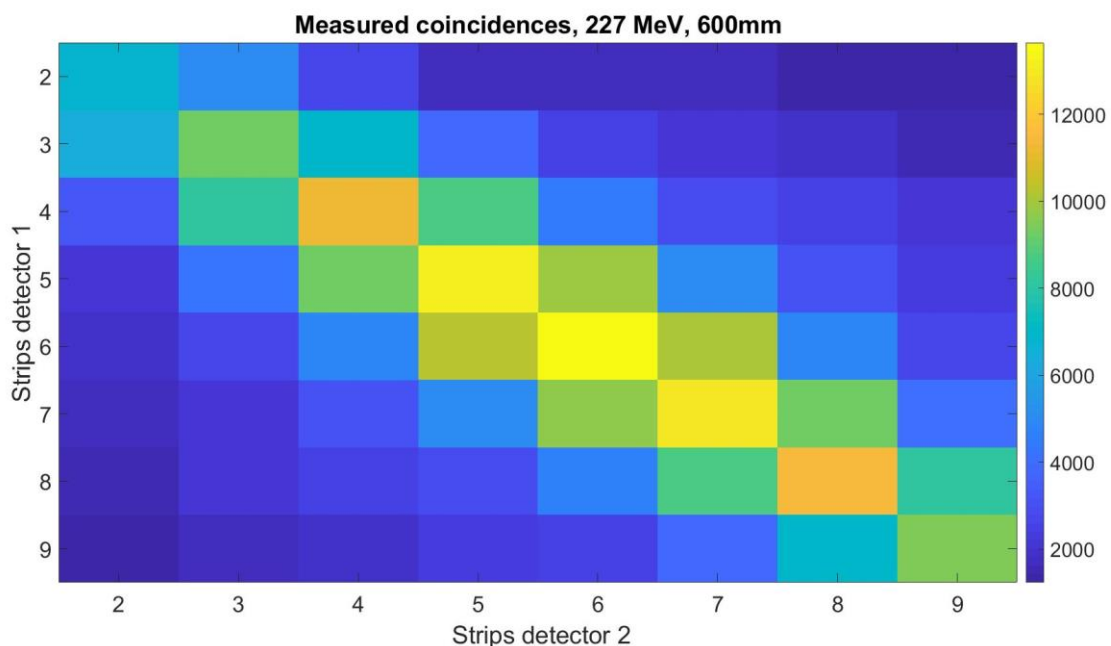


Figure 4.11: Measured number of coincidences per each combination of strips of first and second sensor. The analyzed data come from the simulation at 227 MeV, between 0.1 mm and 600 mm.

The main limit is that it does not know exactly where to look for. Consequently, a lot of false coincidences have been collected. That is why, looking at the previous picture (Fig. 4.11), with the number of coincidences per combination, from the measurement and the ones of the simulation (Fig. 4.8), there is a consistent difference. Even in the combinations very far from the main diagonal (facing strips) there are over 1000 coincidences.

Once again, there are two methods to get rid of the wrong time of flights, define the mean TOF and reduce the related error. To make a comparison, both methods (the same ones of the second chapter) have been employed, namely:

- the *3-sigma method*;
- the *second gaussian method*.

One element in common, between the analysis made up with both of them is related to some main features of the acquisition that have been assumed. First, there is no noise or offset; secondly, the acquisition is assumed to be constant, in terms of incoming particles, simulating the acquisition experienced in CNAO.

In the following section a short recap of the two methods to treat the coincidences and measure the TOF is given.

### 4.3.1 Method 1 (3-sigma method)

The first step of the method 1 is a double gaussian of the histogram that collects all the coincidences stored, from any combinations of strip (Fig. 4.12).

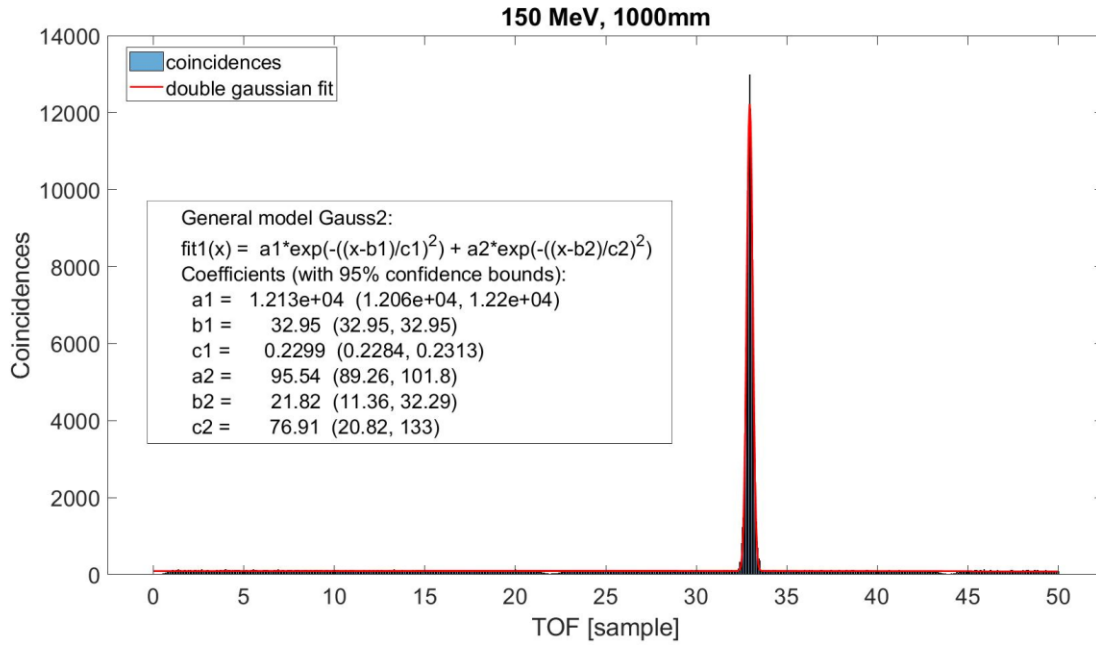


Figure 4.12: Histogram that collects all the TOF stored during the analysis of the signals. The first step of the 3-sigma method is the double gaussian fit of these bins. The equation of the fit is reported.

The code takes  $\sigma$  of the upper gaussian (fit1.c1/ $\sqrt{2}$ , Fig. 4.12) and generates an interval of  $[-1.5 \sigma; +1.5 \sigma]$  around the mean value (fit1.b1 of Fig. 4.12). With the coincidences that lay inside that interval another gaussian fit (single), is applied (Fig. 4.13), from which the mean TOF and related error are defined (Fig. 4.14).

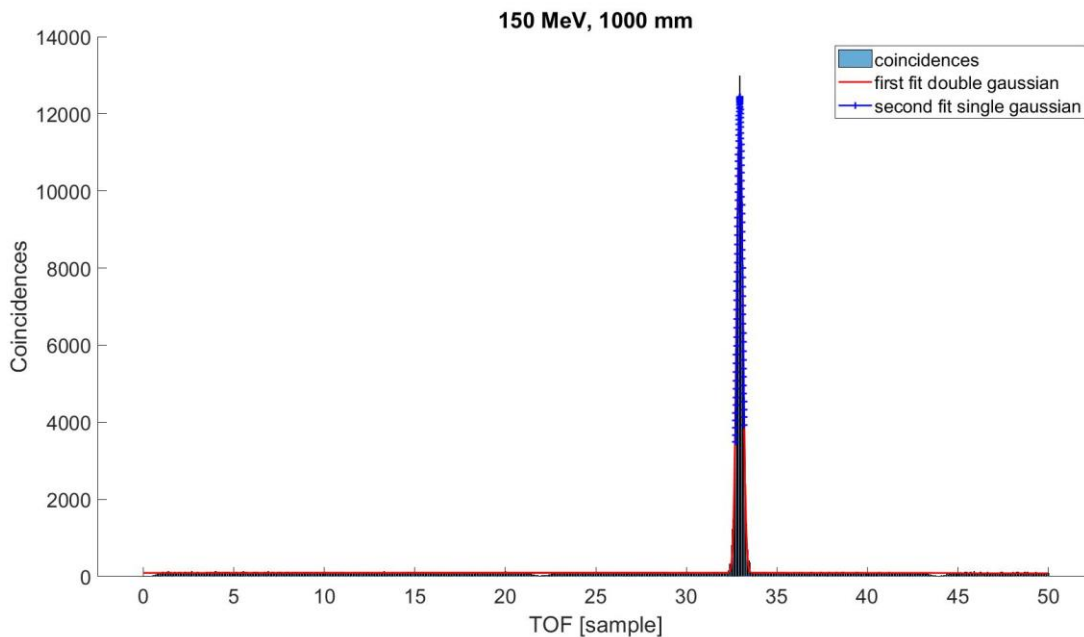


Figure 4.13: Next step of this method, a single gaussian fit (blue line) of the coincidences within the 3-sigma interval.

```

fit2 =

General model Gauss1:
fit2(x) = a1*exp(-((x-b1)/c1)^2)
Coefficients (with 95% confidence bounds):
a1 = 1.244e+04 (1.173e+04, 1.315e+04)
b1 = 32.96 (32.95, 32.97)
c1 = 0.2203 (0.1996, 0.2411)

```

Figure 4.14: Single gaussian fit of the coincidences lay within the interval around the main peak of the histogram (blue line of Fig. 4.13).

The mean TOF is the fit2.b1 of Fig. 4.14, mean value of the final gaussian fit. The error is defined as:

$$err_{TOF} = \frac{\text{upper limit confidence bound} - TOF_{mean}}{2}$$

### 4.3.2 Method 2 (second gaussian method)

Like for the previous approach, this method involves a first double gaussian fit of the coincidences of the histogram (Fig. 4.15), using all the possible combinations between the strips of the two sensors,

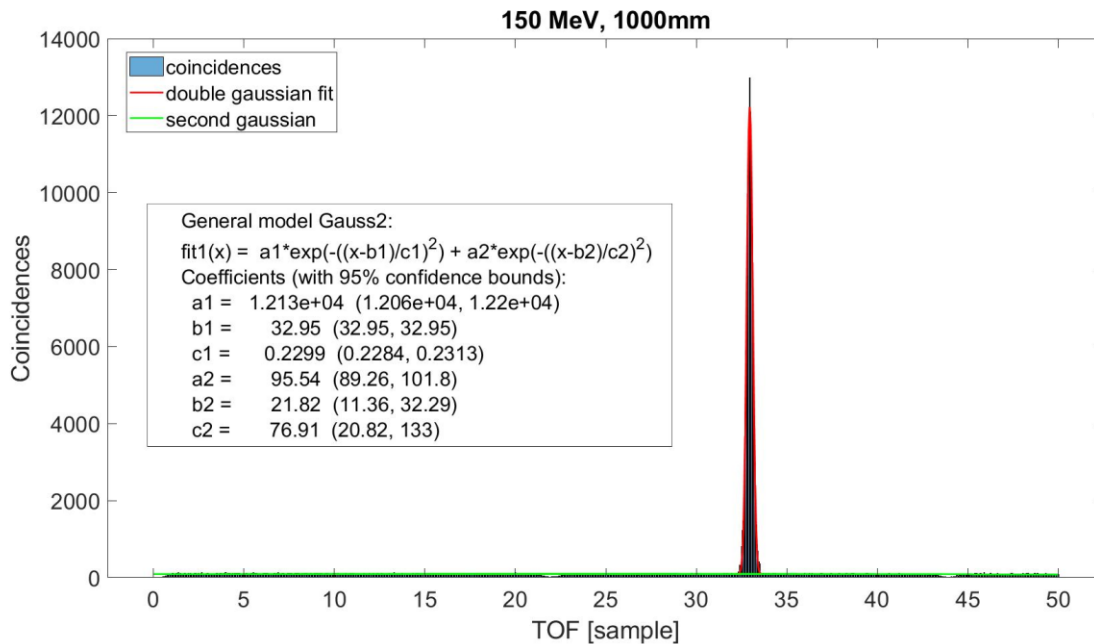


Figure 4.15: Histogram collecting each TOF measured at 150 MeV, with  $S_1$  at 0.1 mm and  $S_2$  at 1000 mm. The red curve represents the double gaussian fit. The horizontal green line is the background level (the bottom gaussian).

The double gaussian fit is the same of the previous method (Fig. 4.12).

The method makes the subtraction between the entire amount of coincidences and the second gaussian of the double gaussian fit,  $a_2 \cdot \exp(-((x - b_2)/c_2)^2)$  of Figure 4.15. Applied to this specific case, having a continuous beam, the second gaussian is a straight line (constant background, green line of Fig. 4.15). After the removal of these coincidences, a second, single gaussian, fit is applied to the remaining ones (Fig. 4.16).

The mean TOF is the mean value of the single gaussian fit, and the error is defined as:

$$err_{mean} = \frac{\sigma}{\sqrt{N}} \quad (2.3)$$

with N equal to the number of coincidences used for the gaussian fit (final one) and  $\sigma$  from the equation of the fit that MATLAB supplies (as  $\frac{c_1}{\sqrt{2}}$ ).

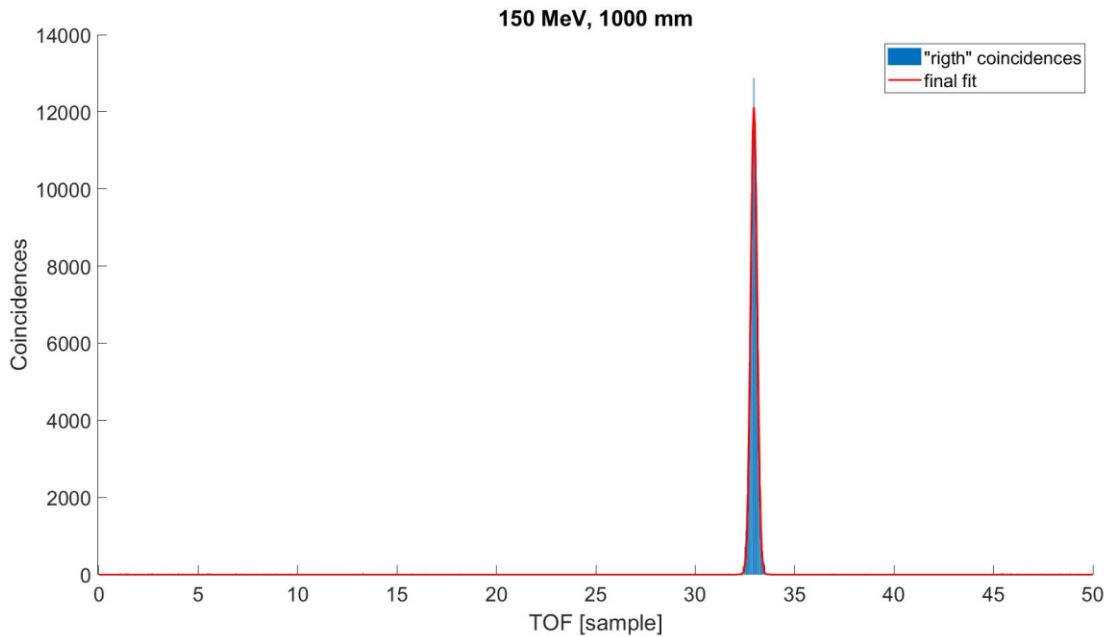


Figure 4.16: Histogram after the second gaussian removal . Finally, a single gaussian fit is applied to determine mean value and mean error.

### 4.3.3 Results

#### 4.3.3.1 Measured results vs simulated results

After the measurements with the analysis app, it is possible to compare the results in terms of difference of TOFs. The ones coming from the simulation are assumed to be exact, and by looking at the  $\Delta TOF$ , the precision of the study of the signals can be established.

Figure 4.17 shows the relation between the exact TOFs and the ones coming from the examinations with the second gaussian method, collecting all the coincidences coming from any combination.

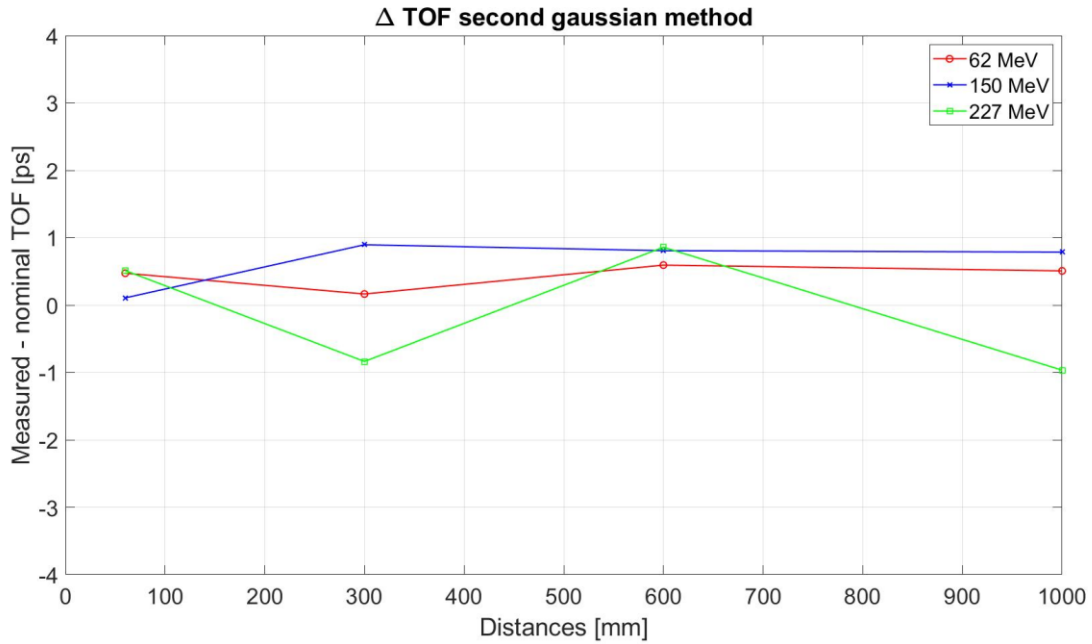


Figure 4.17: Difference between the TOFs measured with the second gaussian method and the ones coming from the simulation.

The  $\Delta TOF$  is always in the range  $[-1;1]$  (Fig. 4.17), even though, there is no clear trend, related to the distance or the energy. For the other method (*3-sigma method*), the  $\Delta TOF$  is bigger, reaching also 2 ps, however also these results are really close the exact ones (Fig. 4.18).

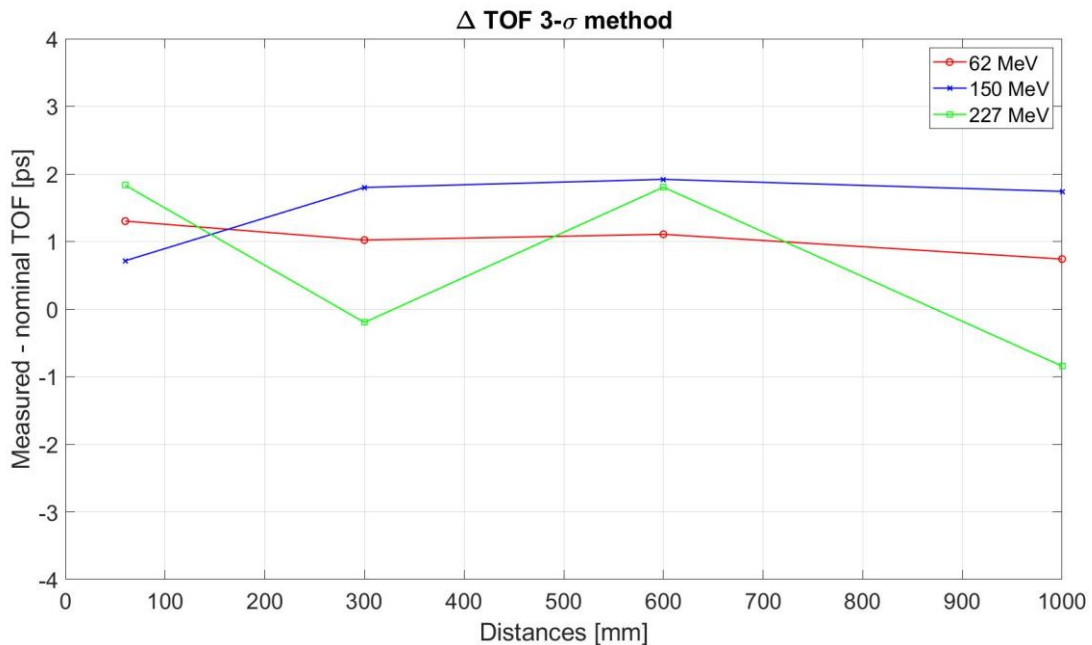


Figure 4.18: Difference between the TOFs measured with the 3-sigma method and the ones coming from the simulation.

Even in this case there is no clear trend for the  $\Delta TOF$ . These results were obtained measuring the TOF by collecting all the coincidences together (from any combination).

Two different approaches may be adopted:

- Facing strips analysis;
- Strip-by-strip analysis;

### 4.3.4 Facing strip analysis

The advantage of using 16 strips to measure the time of flight is linked to the ability of collecting many more coincidences rather than using just two strips. But, of course, using all of them, taking 64 possible combinations, as shown before, there is the risk of giving too much credit to coincidences and relative times that are not useful at all. Therefore, one important analysis can be the TOF study using only the facing strips. Meaning that, once a peak is found in one of the strips of the first sensor, instead of opening the sample window in all the strips of the second sensor, the code just looks inside the signal of the facing strip, leading to a faster study.

The facing strip analysis has been conducted using the TOF with *second gaussian method* (proved to be more precise).

	w1_1	w2_1	w3_1	w4_1	w5_1	w6_1	w7_1	w8_1
w1_2	<input checked="" type="checkbox"/>	<input type="checkbox"/>	<input type="checkbox"/>	<input type="checkbox"/>	<input type="checkbox"/>	<input type="checkbox"/>	<input type="checkbox"/>	<input type="checkbox"/>
w2_2	<input type="checkbox"/>	<input checked="" type="checkbox"/>	<input type="checkbox"/>	<input type="checkbox"/>	<input type="checkbox"/>	<input type="checkbox"/>	<input type="checkbox"/>	<input type="checkbox"/>
w3_2	<input type="checkbox"/>	<input type="checkbox"/>	<input checked="" type="checkbox"/>	<input type="checkbox"/>	<input type="checkbox"/>	<input type="checkbox"/>	<input type="checkbox"/>	<input type="checkbox"/>
w4_2	<input type="checkbox"/>	<input type="checkbox"/>	<input type="checkbox"/>	<input checked="" type="checkbox"/>	<input type="checkbox"/>	<input type="checkbox"/>	<input type="checkbox"/>	<input type="checkbox"/>
w5_2	<input type="checkbox"/>	<input type="checkbox"/>	<input type="checkbox"/>	<input type="checkbox"/>	<input checked="" type="checkbox"/>	<input type="checkbox"/>	<input type="checkbox"/>	<input type="checkbox"/>
w6_2	<input type="checkbox"/>	<input checked="" type="checkbox"/>	<input type="checkbox"/>	<input type="checkbox"/>				
w7_2	<input type="checkbox"/>	<input checked="" type="checkbox"/>	<input type="checkbox"/>					
w8_2	<input type="checkbox"/>	<input checked="" type="checkbox"/>						

Figure 4.19: Section of the TOF measurement app. By checking all the boxes on the main diagonal, the analysis focuses on the facing strips.

In the app, only the boxes on the main diagonal are checked (Fig. 4.19).

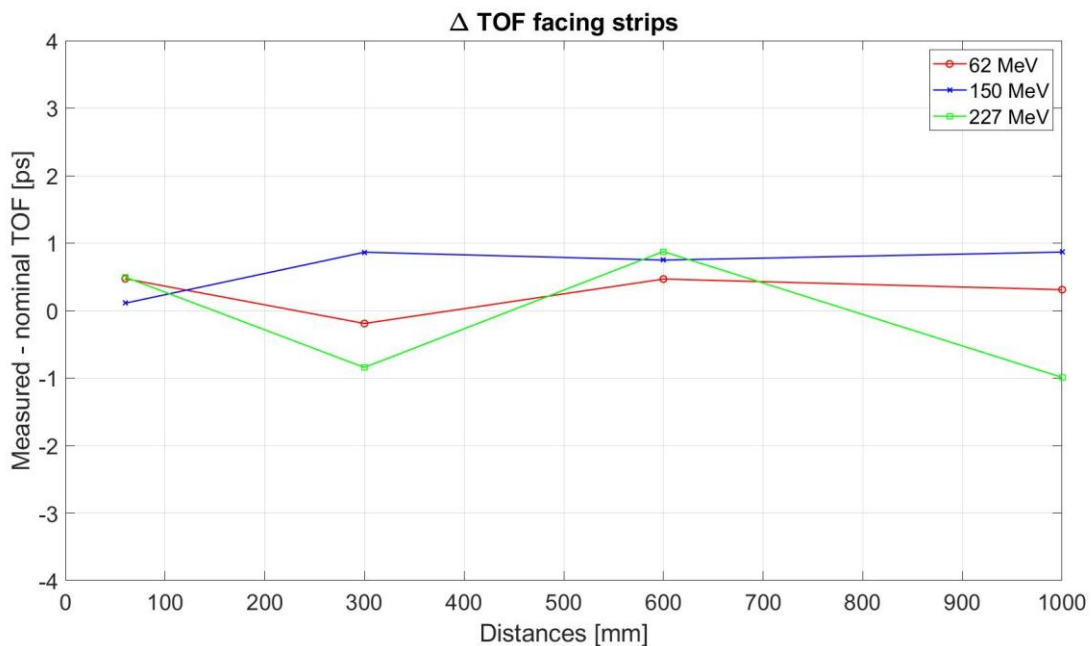


Figure 4.20: Difference between the TOFs measured with the second gaussian method (coincidences from the facing strips only) and the ones coming from the simulation.

The outcomes (Fig. 4.20) are similar, even equal, to the ones coming from the *second gaussian method* for the 64 combinations (Fig. 4.17), that, indeed, removes all the “wrong” coincidences, that comes mostly from the combinations of strips not one in front of the other.

In general, this examination proved that not always is necessary to study all the combinations, but just the facing strips, because, in particular at small distances and high energy, the probability of having a deflection of the normal trajectory of the particles is very small. Furthermore, this analysis is faster than the previous ones.

### 4.3.5 Strip-by-strip analysis

The strip-by-strip analysis is interesting when the measurement involves bigger distances and smaller energies, because in these situations, there is a certain spread out of the flux, with an increase of the probability that the proton crossing a certain strip of the first detector of being deflected.

In these situations, the number of coincidences starts to homogenize over the dimensions of the detector (and even beyond, going over target and not being certified). And when it comes, it is important to maintain a certain level of precision over the evaluation of the TOF, paying attention also at the most improbable combinations of strips.

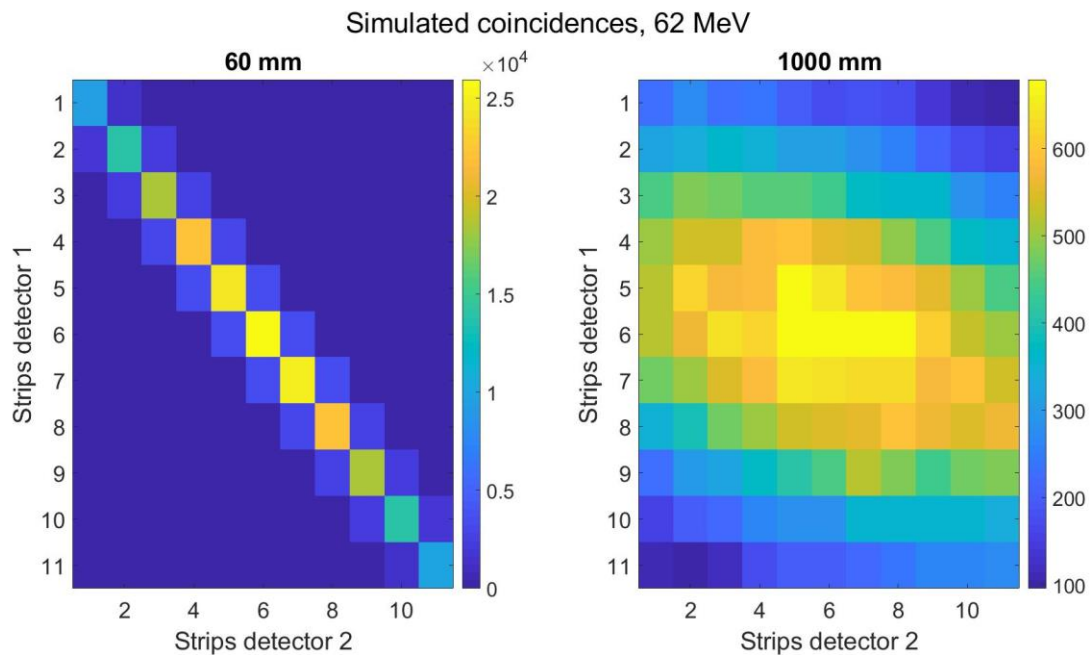


Figure 4.21: Comparison between the distribution of coincidences, simulated, with  $S_2$  at 60 mm and 1000 mm.  $S_1$  is fixed at 0.1 mm.

Figure 4.21 shows the coincidences coming from the simulation at 62 MeV with  $S_2$  positioned at 60 and 1000mm. The following legend has been followed (strip detector 2, strip detector 1), like (x,y) coordinates. In the combination (6,6) at 60 mm there are 26000 coincidences, and at 1000 mm, in the same box there are 671 coincidences.

The number of coincidences, in the peripheral regions increases. In the combination (9,2), at 60 mm there is only 1 coincidence, while at 1000 mm they are more than 200. These are the result of the simulation, so every time of flight stored is “correct”. Doing the same kind of analysis with the results of the TOF measurement app, it should be possible to appreciate the same behavior, but in this case, most of the TOFs stored in that locations will be very different than the expected ones. At least, the hope would be that, increasing the distance, the number of right coincidences inside the most improbable combinations is bigger.

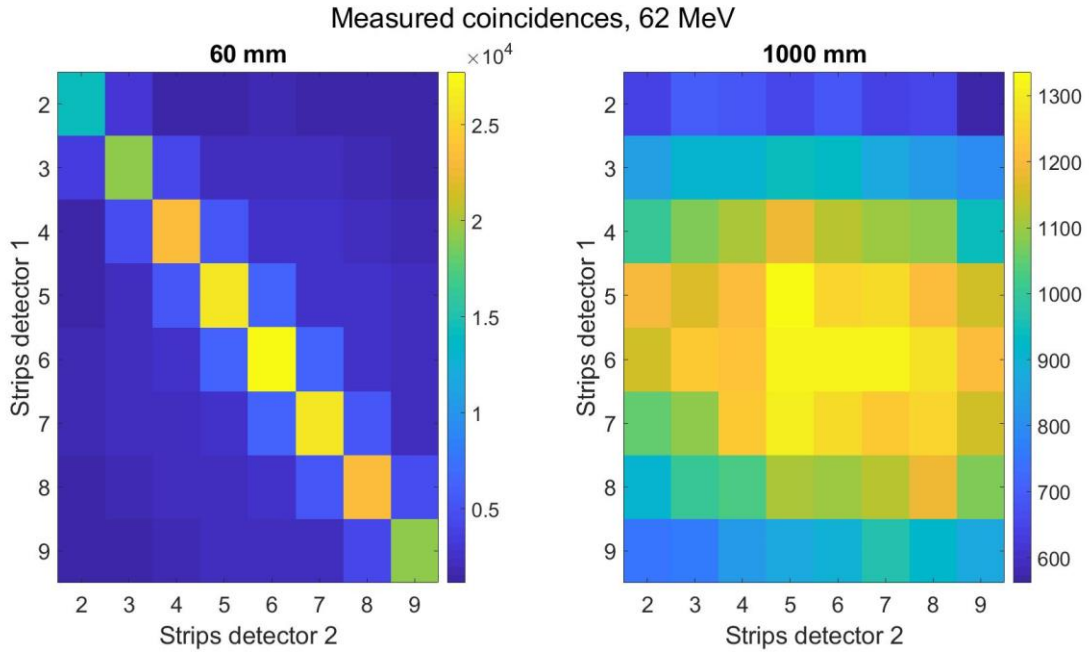


Figure 4.22: Comparison between the distribution of coincidences, measured, with  $S_2$  at 60 mm and 1000 mm.  $S_1$  is fixed at 0.1 mm.

The measured coincidences are represented by Figure 4.22. Looking at the same points as before, there are, for the combination (6,6), at 60 mm 27750 coincidences, and 1322 at 1000 mm. For the combination (9,2), at 60 mm there are 1151 coincidences and at 1000 mm they are 560.

Knowing the results of the simulation (that would not be available in case of experimental data acquired on the field), it is easy to say that of those 1151 coincidences (from (9,2) at 60 mm) just one is correct. As well as the almost 2 thousand coincidences wrong in (6,6).

Doing the ratio:

- $\frac{\text{Simulated coincidences } 60 \text{ mm}, (6,6)}{\text{Measured coincidences } 60 \text{ mm } (6,6)} = \frac{26000}{27750} = 93.7 \%$
- $\frac{\text{Simulated coincidences } 60 \text{ mm}, (9,2)}{\text{Measured coincidences } 60 \text{ mm } (9,2)} = \frac{1}{1151} = 0.087 \%$
- $\frac{\text{Simulated coincidences } 1000 \text{ mm}, (6,6)}{\text{Measured coincidences } 1000 \text{ mm } (6,6)} = \frac{671}{1322} = 50.76 \%$
- $\frac{\text{Simulated coincidences } 1000 \text{ mm}, (9,2)}{\text{Measured coincidences } 1000 \text{ mm } (9,2)} = \frac{209}{560} = 37.32 \%$

These number shows that at small distances, the percentage of “correct” coincidences over the main diagonal, stored by the measurement app, is almost 100%, and there is no point in looking at the peripheral boxes. Therefore, the measurement can be done using the facing strips only. The only risk related to this approach is that, at bigger distances, the number of values stored inside the main diagonal falls and it may lead to a not precise evaluation of the time of flight. Indeed, the calculated percentages for the combinations (6,6) show a decrease of 40% of the “correct” coincidences stored over the facing strips. Therefore, it could be useful to consider all the possible combinations. This homogenization of the “correct” coincidences over the dimensions of the detector is represented in figures 4.23 and 4.24.

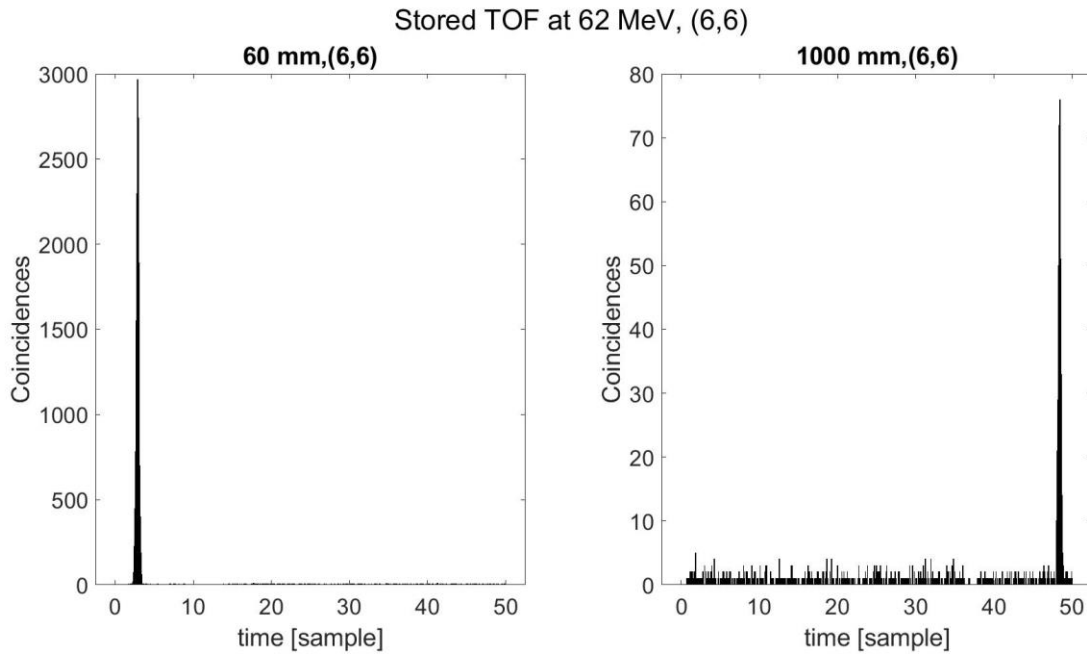


Figure 4.23: Histograms collecting the measured TOF at two different positions of  $S_2$ , same combination of strips, (6,6). On the left-hand side,  $S_2$  is at 60 mm. On the right-hand side,  $S_2$  is at 1000 mm. The strips 6, for both the sensors, is the one with the higher rate of protons.

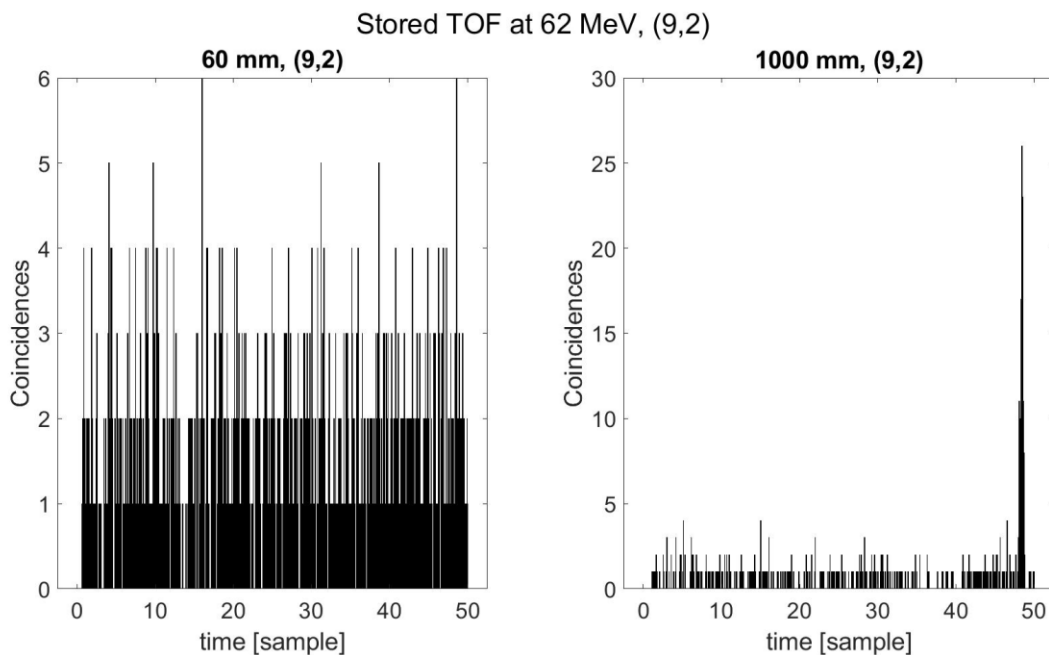


Figure 4.24: Histograms collecting the measured TOF at two different positions of  $S_2$ , same combination of strips, (9,2). On the left-hand side,  $S_2$  is at 60 mm. On the right-hand side,  $S_2$  is at 1000 mm. The combination is, ninth strip of first detector and second strip of second sensor. Is one the poorest combination, in terms of stored coincidences.

There is, though, a limit to this kind of approach. Using the *second gaussian method* for any combinations leads, mostly treating the peripheral boxes, to strange results and MATLAB errors, due to the lack of a sufficiently high number of coincidences. In this case, due to the short distance between the two detectors, the majority of the coincidences is concentrated over the main diagonal, and over some other combinations adjacent. Because of this, for the strip-by-strip analysis, the code has been modified. Basically, the “usual” *second gaussian method* has been employed to treat the data of the main diagonal, and on the two diagonals adjacent (in which the expected number of

coincidences is sufficiently high). But, for all the other combinations, there is a certain threshold that must be fulfilled. Indeed, for the first double gaussian fit, only the bins with more than 10 coincidences are considered. After the removal of the constant background, only the bins with at least 5 coincidences are involved in the final single gaussian fit. At the end of this process, if the resulting TOF is smaller than 0 or bigger than 10 ns (impossible, having set a sample window of 10 ns), it is forced to 0.

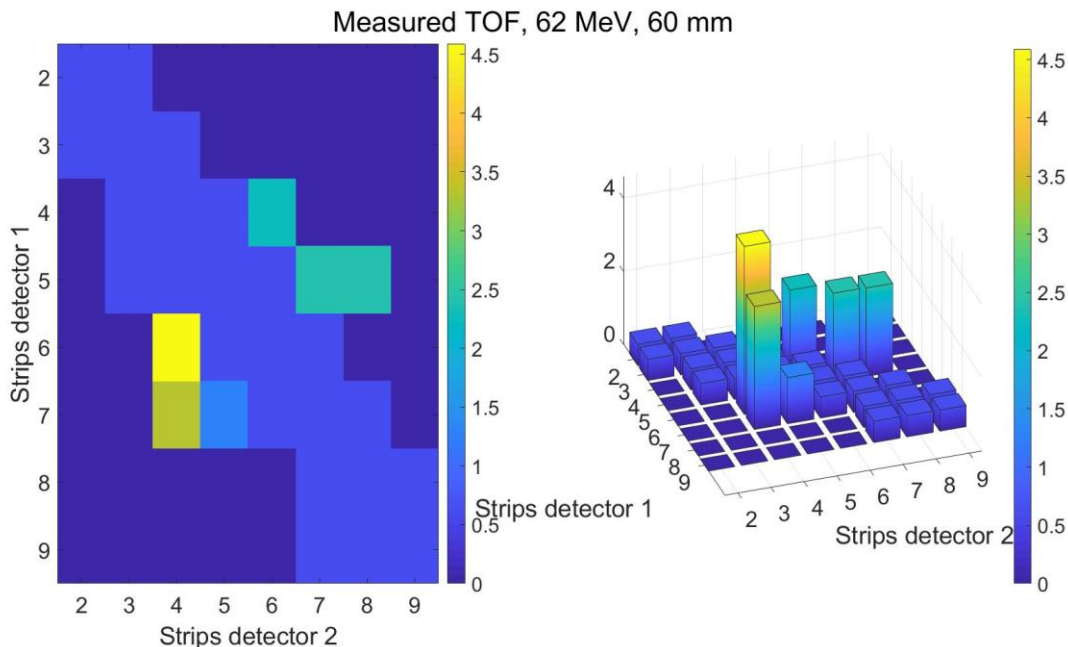


Figure 4.25: Measured TOF at 62 MeV, with  $S_1$  at 0.1 mm and  $S_2$  at 60 mm. On the left-hand side there is a 2D plot of the measured TOF, with the yellow boxes that shows a value very different with respect to the one on the main diagonal, that is around 0.3ns. On the right-hand side, are represented the same numbers but in a 3D bar plot, to show clearly with combinations are out of the proper values and of how much.

All the deep blue boxes are zeros. On the main diagonal and on the adjacent diagonals there is a value that oscillates between 0.3425 and 0.3347 ns. Then, there are other combinations (the green and yellow boxes in Fig. 4.25) with values that are out of the way. This proves that, even if has been modified, this version of the code, for the strip-by-strip analysis is not valid. There are still some combinations, in which, the number of coincidences stored are sufficiently high to be considered, and the resulting TOF is in interval  $[0;10]$  ns. But, the majority of the coincidences are “wrong”, leading to very absurd resulting time of flights (Fig. 4.25).

One possible solution is to merge the two methods, *second gaussian method* and *3-sigma method*, explained before, to treat the coincidences.

#### 4.3.6 Combination of 3-sigma and second gaussian method

A possible solution to overcome the limits of this analysis (Fig. 4.25), is a combination of the *second gaussian method* and *3-sigma method*. Basically, the approach adopted for the coincidences treatment is the same (*second gaussian method*), but there is a check of the results of the combinations of the non-facing strips, using the criteria of the *3-sigma method*.

Taking Figure 4.25 as model, the rows are the strips of the first sensor, while the columns are the strips of the second detector. The boxes are the combinations of them. For any row and column investigated, this new approach saves the TOFs coming from the analysis of the facing strips considered, and they are used as reference values. All the other results, of the same row (same strip of the first sensor, but non-facing strips of the second one), are then compared with the correspondent

values used as model. For example, the TOF measured from the combination (2,6) is compared with the one of the combination (2,2).

There are two conditions that must be respected to consider the TOF of (2,6) a valid one:

1.  $TOF_{(2,2)} - 1.5 * \sigma_{(2,2)} < TOF_{(2,6)} < TOF_{(2,2)} + 1.5 * \sigma_{(2,2)}$
2.  $\sigma_{(2,6)} < 3 * \sigma_{(2,2)}$

Condition 1 guarantees that the mean value of (2,6) is not that far from the “correct” one (but within the 3-sigma interval), and the condition 2 guarantees that, even though the mean value may be good, the dispersion must not be too large.

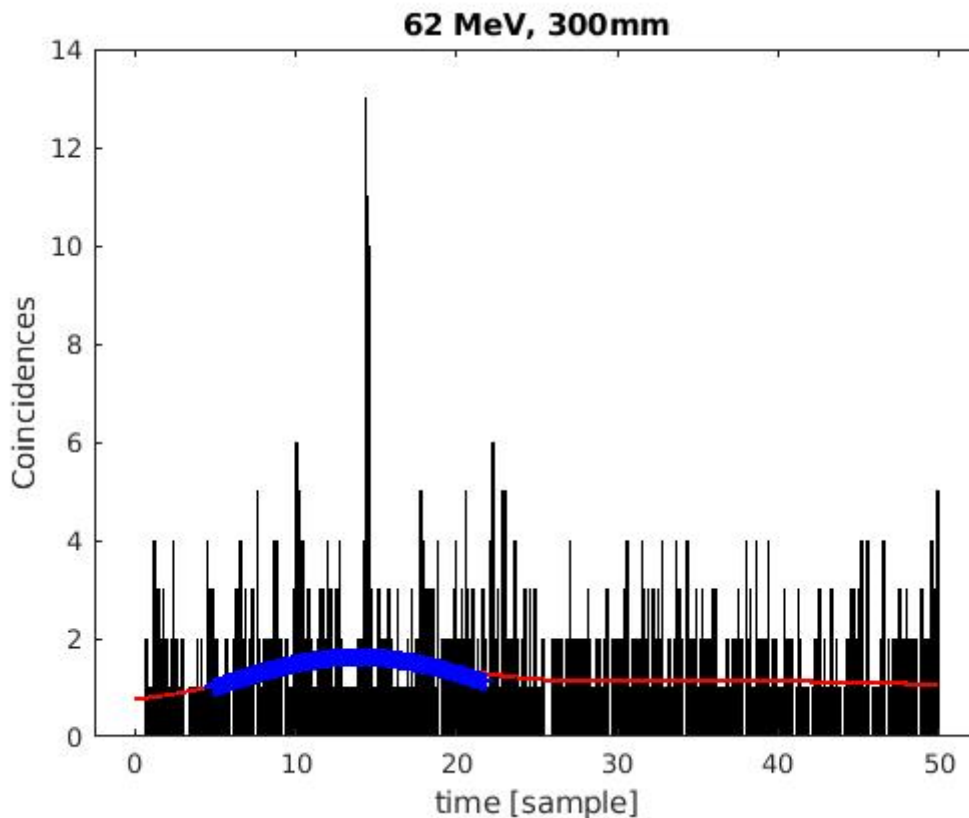


Figure 4.26: Histogram of the combination (7,2), with all the TOF measured at 62 MeV, with  $S_2$  at 300 mm. The red curve is the double gaussian fit, and the blue curve is the single gaussian fit after the application of the second gaussian method.

Condition 2 avoids situation like the one in Figure 4.26, occurring at 62 MeV, at 300 mm of distance between the detectors. The one represented is the combination (7,2), with mean TOF and dispersion that must be compared with the reference values from (2,2). The TOF calculated, around 2.8 ns, is close to the reference one, 2.3 ns, but because of the big dispersion from the second fit, this value is non accepted in the analysis. This process (checking the results) is then repeated for any combination that does not lays over the main diagonal.

It is not easy to appreciate it, but a clear image of this problem comes from the figure that collects the histograms of all the 64 combinations (Fig. 4.27), coming from the analysis of the simulation conducted at 62 MeV, and 60mm distance between the detectors.

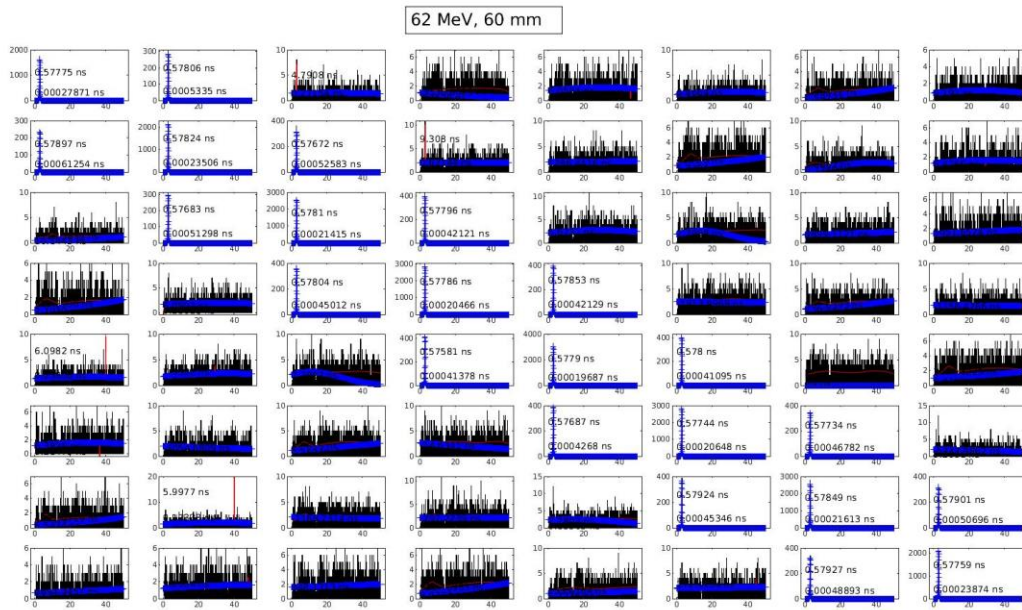


Figure 4.27: Histograms of the 64 possible combinations at 62 MeV, with  $S_2$  at 60 mm. On the main diagonals, the histograms show very narrow peaks, while on the other combinations there is no clear peak.

In conclusion, this procedure allows to get a good estimation of the TOF, but it is too complex and slow compared to the analysis of all the combinations combined together or to the facing strips analysis. Still, it could be useful for some particular application, like the one described in the following section.

## 4.4 Alignment analysis

The previous sections show that the easiest method to treat the simulated signals is by collecting all the 64 combinations together and fitting the data, rather than the strip-by-strip analysis. The latter, though, through a better characterization of the beam, allows a rough analysis about the alignment of the two sensors.

There is the possibility of having wrong positioning of the sensors along the three axes: x, y and z. As described in the section 4.2.1, the z-axis represents the distance of the detector with respect to the origin of the proton beam. While y-axis and x-axis stays as, respectively, the height and the width of the detector (Fig. 4.28).

Considering the alignment analysis performed prior the experimental acquisition, for the tests conducted (section 2.2), the most probable misalignment is the one over the z-axis, because of a tilt of the structure that holds the detector. This is the topic of this section of my thesis. However, it would be interesting, and useful, the development of a tool, within the measurement app, able to detector any possible problem about the positioning of the detector, like the one in Figure 4.30 (X-Y plane misalignment).

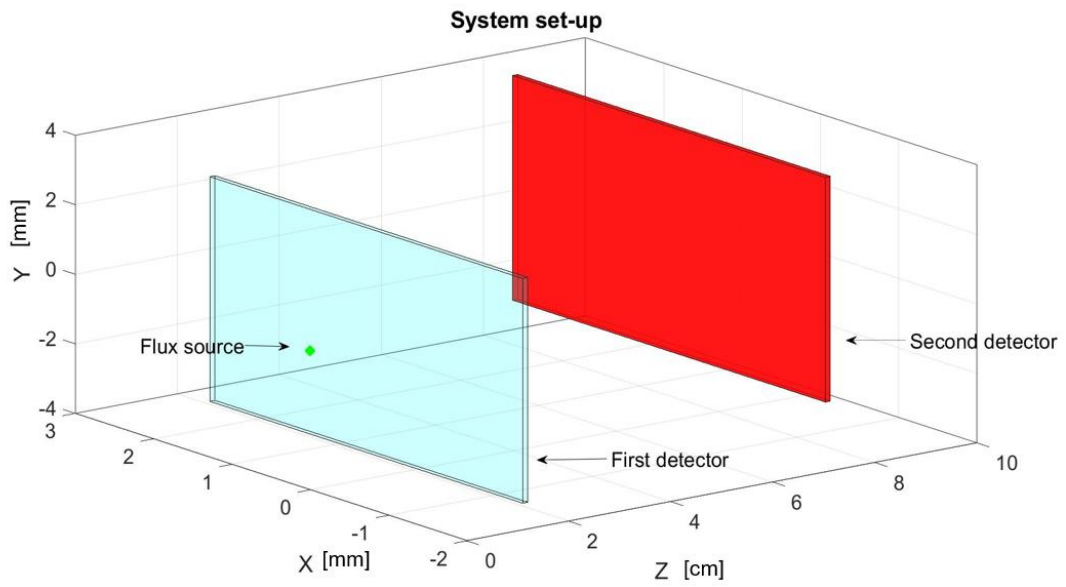


Figure 4.28 : Schematic view of the disposition of the two detectors in the Geant4 simulation.

The green dot is the origin of the system where it supposed to start the proton flux.

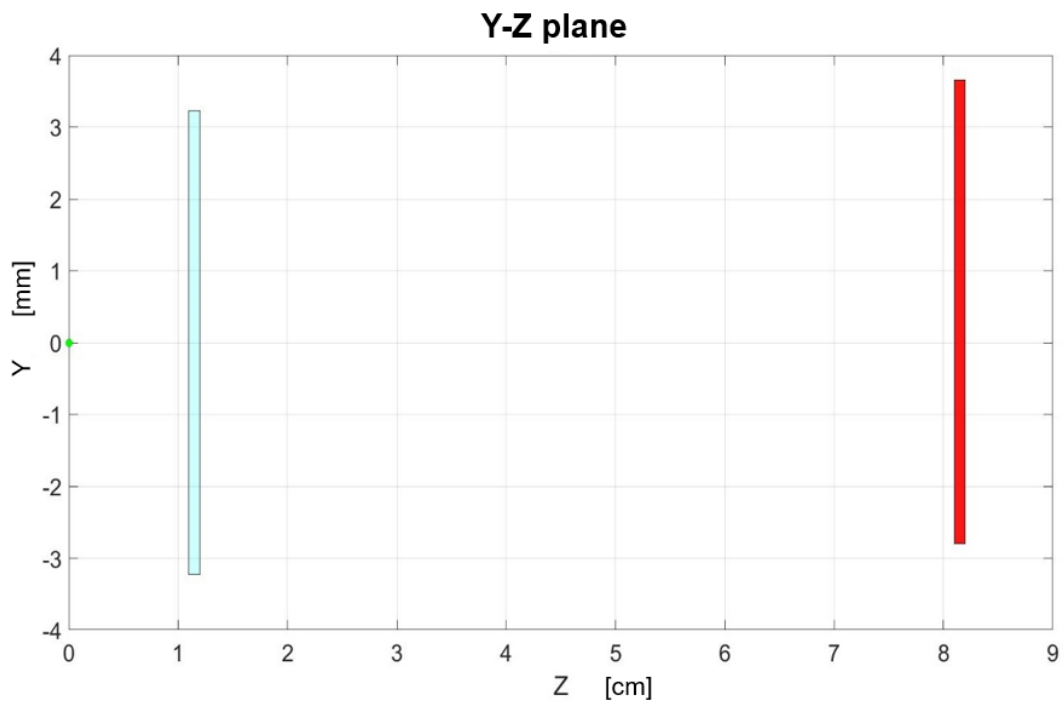


Figure 4.29 : Y-Z plane of Fig. 4.28. This figure represents a misalignment over the Y-axis.

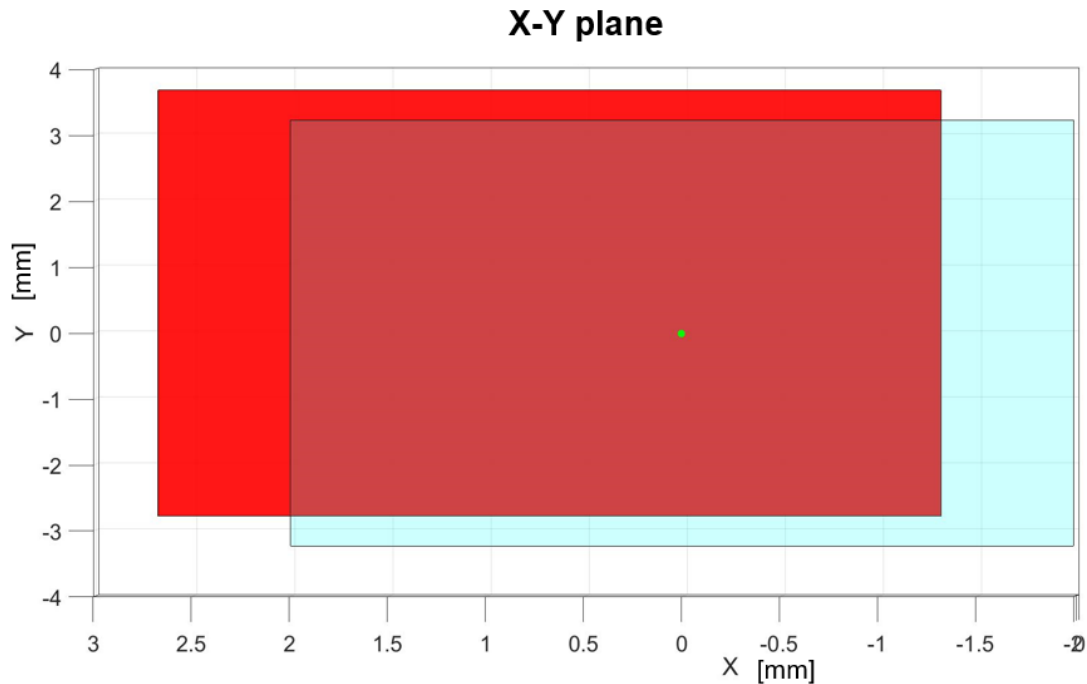


Figure 4.30: X-Y plane of Fig. 4.28. In this case, the misalignment is simulated over the X and Y-axis.

#### 4.4.1 Y-Z plane misalignment.

The study related to the alignment has been focused on the Y-Z plane (Fig. 4.29), with Z that represents the distance of the detector from the origin of the system (distance from the start position of the protons), and Y is the height of the detector.

In this kind of evaluation, the strip-by-strip distribution of the coincidences is crucial.

For a perfectly aligned system, there should be the maximum value of coincidences over the main diagonal, meaning over the facing strips.

The sensor, specifically designed for the MoVeIT project (already employed for the tests conducted at TPT), has 11 strips. As mentioned, the first, tenth and eleventh strips would not be involved in the proper acquisition of the signals (future tests). Despite it, within the Geant4 simulation, the designed detector has the same dimensions of the real one, including these 3 strips. Therefore, the matrix, generated at the end of the beam simulation, is 11x11. However, the simulation app has been developed to keep trace of the signals of just 8 strips, from the second to the ninth. Still, over the user interface, there is the possibility of choosing a different beginning strip for both the detectors (Fig. 4.31).

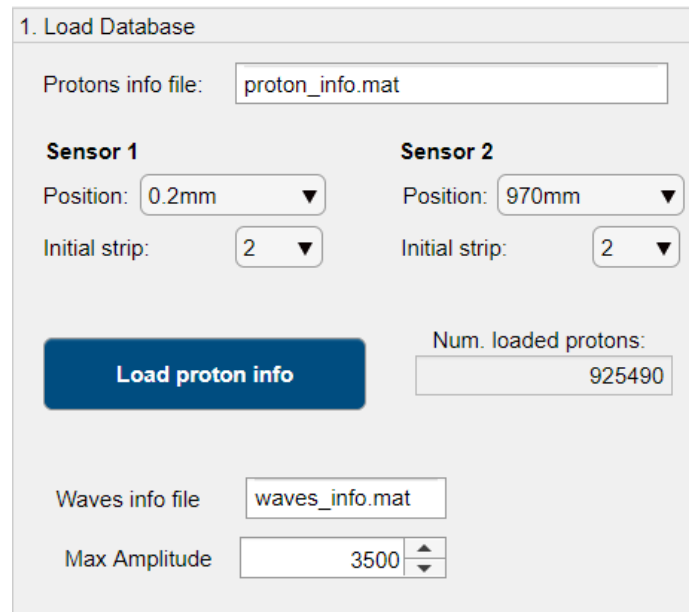


Figure 4.31: Zoom over the step 1 of the simulation app (Appendix E). This section gives the possibility of choosing the position of the two detectors (Z-axis, distance from the origin of the beam), and the initial strip of the two detectors.

A possible way to simulate a condition of not aligned sensors over the Y-Z plane relies on this aspect of the simulation that can be changed from the app interface. The idea is: keep the initial strip of the first sensor fixed at 2 and see what happen changing the first strip of the second sensor to 1 and 3. Basically it is like moving the second sensor up and down of one strip. After the simulation, the signals can go through the analysis app.

The simulation has been completed at 150 MeV.

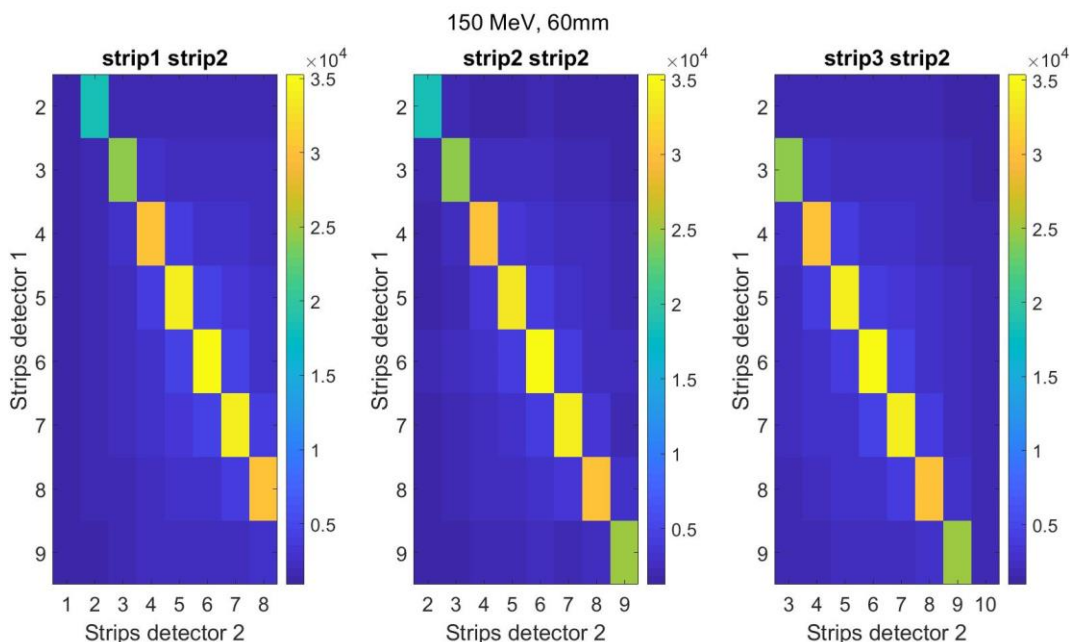


Figure 4.32: Simulation of the misalignment over the Y-Z axis. These three plots represent the distribution of the coincidences over 64 strips combinations, coming from the analysis of the simulation at 150 MeV and 60mm distance between the two detectors. In all the three plots, the strips of the first detectors are 2-9, while the ones of the second detector change. Going from the left-hand side plot to the one on the right-hand side, the strips of the second detector are: 1-8, 2-9, 3-10. The main diagonal, with the biggest number of coincidences collected (facing strips), moves according to the strips of the second sensor considered.

As expected, changing the first strip of the second sensor there is a right and left shift of the diagonal, that collects the biggest number of coincidences (Fig. 4.32). Setting the strip 1 as the first of the second detector, the diagonal goes right. And, at the same way, starting from the strip 3, the maximum value in the first row is not even there. Even though, considering the small distance (60mm), this analysis cannot be taken for granted. Even more so if the same process is adopted at bigger distances, like the following picture, in which it is not possible to recognize the same trend.

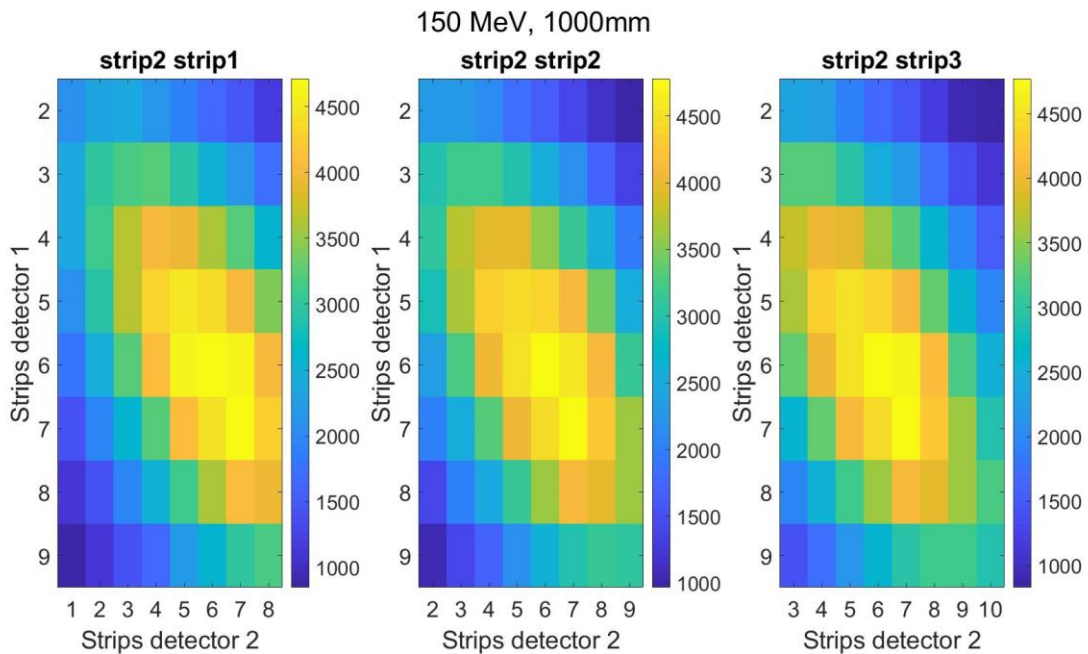


Figure 4.33: Same analysis of the Fig. 4.32. In this case, though, the simulation has been conducted at 1000mm of distance between the two detectors. This time there is no clear main diagonal (facing strips) with the biggest number of coincidences. Because of the big distance, there is a certain spread out of the flux that starts homogenizing over the entire dimension of the sensor.

This first test about the misalignment analysis must be taken carefully. Figure 4.32, even if at small distance, shows a clear pattern, that because of the homogenization of the coincidences over the detector at big distances (Fig. 4.33), disappears. Still, some further steps can be done in this direction to exploit the full capability of the app, mostly by improving the parameters setup in the simulation. Increasing the dimension of the sensitive detectors within the Geant4 simulation, it should be possible to investigate a misalignment (over the three axis) of just few microns. Indeed, one the major limit of this analysis relies in the possibility of investing a possible misalignment by one strip. Increasing the dimensions of the detector, over the three axes, the tool of the simulation app can be implemented in order to allow very small “movements” of the second detector.

Another step, still related to the Geant4 simulations, is the change of the distribution of the beam. In this way, the misalignment tool can be tested, and check whether if it is or not able to recognize some other patterns in the distribution of the coincidences, that may be evidence of a wrong positioning of the detectors.

## 4.5 Calibration validation

In addition to the results seen up to this point, two further simulations, at 105 and 180 MeV, have been conducted. With the TOF measured at these 5 distances, and 4 positions, the “simulated system” can be calibrated. Applying the calibration method, Ordinary Least Squares (OLS) and Weighted Least Squares (WLS) minimization, in terms of distance and offset, the process should give back the exact first simulated distance and a time offset equal to 0 (or so), because of the absence of cables and digitizer. In this way, a validation of the *relative approach* can be performed and check whether if the results satisfy the expectations or not. The main purpose of this further analysis is to establish if the *relative method*, explained in the third chapter, is correct.

The ones in Table 4.1 are the TOFs measured, adopting the *second gaussian method* and using all the 64 combinations, from the simulated signals.

Table 4.1 : Table collecting the TOF measured, adopting the *second gaussian method*, from the simulation conducted at 5 energies and 4 positions.

Distance [mm]	Energy at the isocenter [MeV]	Mean TOF [ns]	Mean TOF error [ps]
60	62	0.578	0.359
60	105	0.457	0.360
60	150	0.395	0.339
60	180	0.368	0.341
60	227	0.337	0.347
300	62	2.894	0.446
300	105	2.290	0.406
300	150	1.976	0.367
300	180	1.839	0.369
300	227	1.687	0.371
600	62	5.796	0.573
600	105	4.584	0.451
600	150	3.953	0.423
600	180	3.680	0.412
600	227	3.376	0.377
1000	62	9.676	0.967
1000	105	7.643	0.629
1000	150	6.591	0.498
1000	180	6.135	0.484
1000	227	5.627	0.431

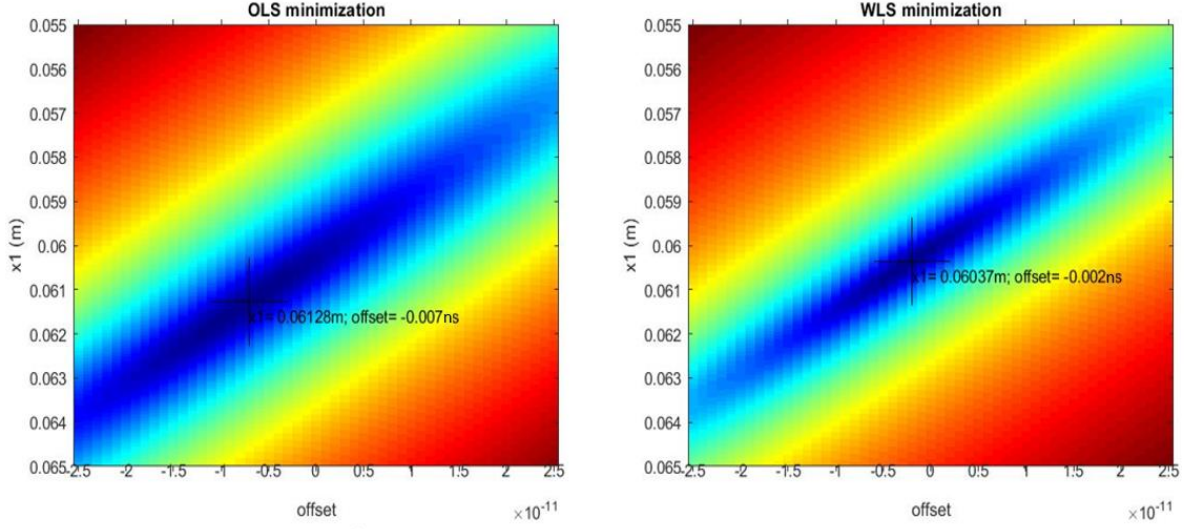


Figure 4.34: Outcomes of the calibration of the simulated system adopting the OLS and WLS minimization.

The expected  $x_1$  is 60 mm and *offset* equal to 0.

Table 4.2: Results of the calibration of the simulated system adopting the OLS and WLS minimization.

OLS		WLS	
$x_1$ [mm]	<i>offset</i> [ps]	$x_1$ [mm]	<i>offset</i> [ps]
61.28	-7	60.37	-2

The results are pretty close to the nominal values (simulated ones). In particular, the outcomes of the weighted least squares minimization have just 370  $\mu\text{m}$  of difference, for the distance, and 2 ps with respect to the time offset (Table 4.2 and Fig. 4.34).

As explained before, with the outcomes of the calibration process it is possible to measure the energy of the beam at the isocenter (considering  $L$  as  $x_1 + \Delta x$ ):

$$v_{avg} = \frac{L}{TOF - offset} \quad (2.1)$$

$$K_{avg} \cong E_0 \left( \frac{1}{\sqrt{1 - \left(\frac{v_{avg}}{c}\right)^2}} - 1 \right) \quad (3.2)$$

$$K_1 = K_{avg} + \left( \frac{S}{\rho} (K_{avg}) \right)_{air} \cdot \rho_{air} \cdot \frac{L}{2} \quad (3.4)$$

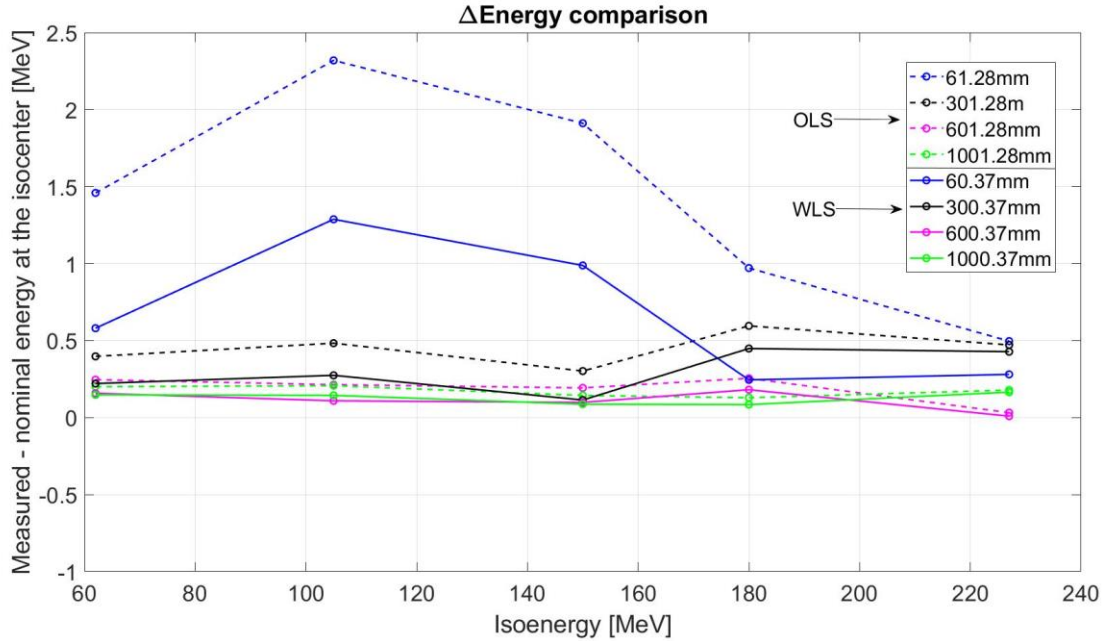


Figure 4.35: Difference between the measured and the nominal energy at the isocenter. These energy levels have been measured using the first distance ( $x_1$ ) and the time offset coming from calibration of the system, adopting the relative approach.

Figure 4.35 shows the difference between the measured and the nominal energy at the isocenter (position 0 of the simulation). The trend is pretty much the same already saw in the results of the tests conducted at TPT and CNAO. Increasing the distance, the energy measured seems more precise. It is clear the improvement going from, talking about nominal distances, 60 mm to 300 mm, and from 300 mm to 600 mm. Even though, there is no appreciable variation between 600 and 1000 mm. They are kind of overlapped. Another interesting outcome of this graph is related to the differences between the energy difference between OLS and WLS minimization process. Also in this case, as in the previous chapter, the energy measured with the  $x_1$  and the *offset* coming from the WLS minimization seems more precise, in particular at small distances.

From the beam energy, the water range can be measured, as explained in the introduction of the third chapter (Eq. 3.1) and compared with the one of the nominal energy ( $\Delta range$ ).

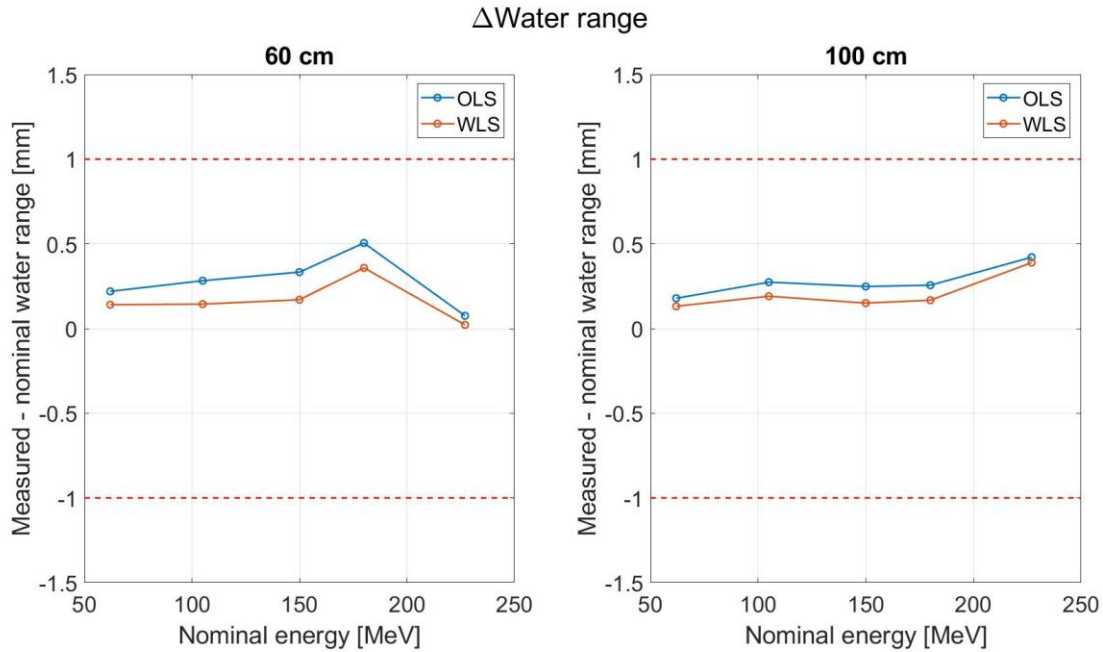


Figure 4.36: Difference between the measured and the nominal water range at 60 and 100cm. These water ranges have been measured using the energy levels of Fig. 4.35.

The water range is always within the limit of 1mm from the nominal one, even though there is no much difference between the OLS and WLS minimization results (Fig. 4.36).

It would be interesting a comparison between the results obtained with the full detectors (16 strips) involved in the acquisition, and the tests performed at TPT, with just one strip of the detector used. Unfortunately, because of the simulated nature of the signals involved in this chapter, this kind of analysis cannot be performed. Still, one possible way to evaluate the evolution of the results, according to the change in the statistics (a change in the number of strips) is to modify the number of strips involved in the TOF measurement, directly from the user interface of the app. The parameter that, at the end, will be compared, is the sum of the square of the water range residuals, from the energy measured at the biggest distances (600 and 1000mm).

To perform this analysis, some guidelines must be followed. First, all the simulations involved must have the same number of events, to simulate the same acquisition time. Second, because of the non-uniform distribution of the flux over the detector (Fig. 4.9), it has been decided to start from the strip with the highest number of coincidences (strip 6 of detector 1) and keep increasing the number adding one strip per side. The other aspect that must be faced, is which strip of the second sensor must be evaluated. The following results are collected considering the facing strip, and the two adjacent.

To summarize:

- First step. Detector 1: strip 6. Detector 2: strip 5 to 7;
- Second step. Detector 1: strip 5 to 7. Detector 2: strip 4 to 8;
- Third step. Detector 1: strip 4 to 8. Detector 2: strip 3 to 9;
- Fourth step. Detector 1: strip 3 to 9. Detector 2: strip 2 to 9.

For each test, the TOF has been measured at 4 distances (60,300,600 and 1000mm), applying the *second gaussian method* to the coincidences of all 64 combinations combined together. These TOFs have been used to calibrate the “simulated system”, in terms of distance and time offset, and with the results, it has been possible to evaluate the beam energy and the beam range (with the process explained before).

Finally, the square of the differences (residuals) between the measured and the nominal range in water (at 600 and 1000 mm) have been summed. The expected result is a decrease of this value increasing

the number of strips involved. Meaning, a more precise estimation of the beam energy (and of the water range), increasing the statistics.

In Figure 4.37 is represented the difference between the measured and the nominal energy, computed with  $S_2$  at 1000mm, with distance and time offset coming from the OLS and WLS minimization.

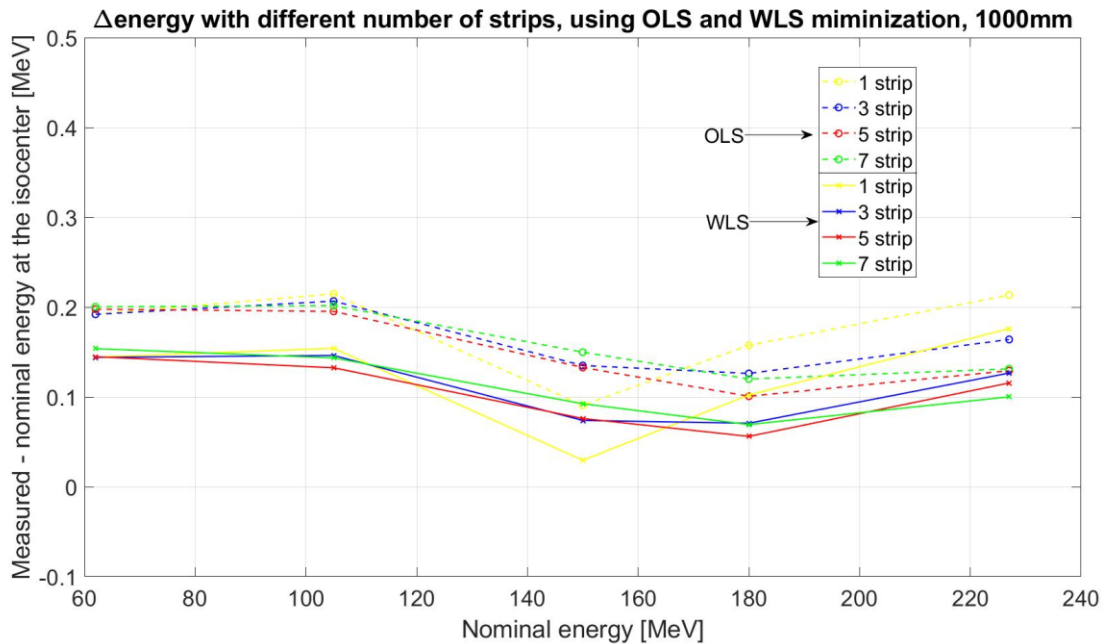


Figure 4.37: Difference between the measured and the nominal energy at 1000mm. These energies have been measured from the calibration of the system, using the TOF measured considering 1,3,5, and 7 strips of the first detector, and the second detector at 1000mm.

All the points of Fig. 4.37 are very close to 0, and there is no significant improvement of the results by increasing the number of the strips involved in the acquisition. However, with the energy levels, the water range can be measured and compared with the nominal one.

The  $\Delta range$  profile, at 600mm and 1000mm, is represented in figures 4.38 and 4.39.

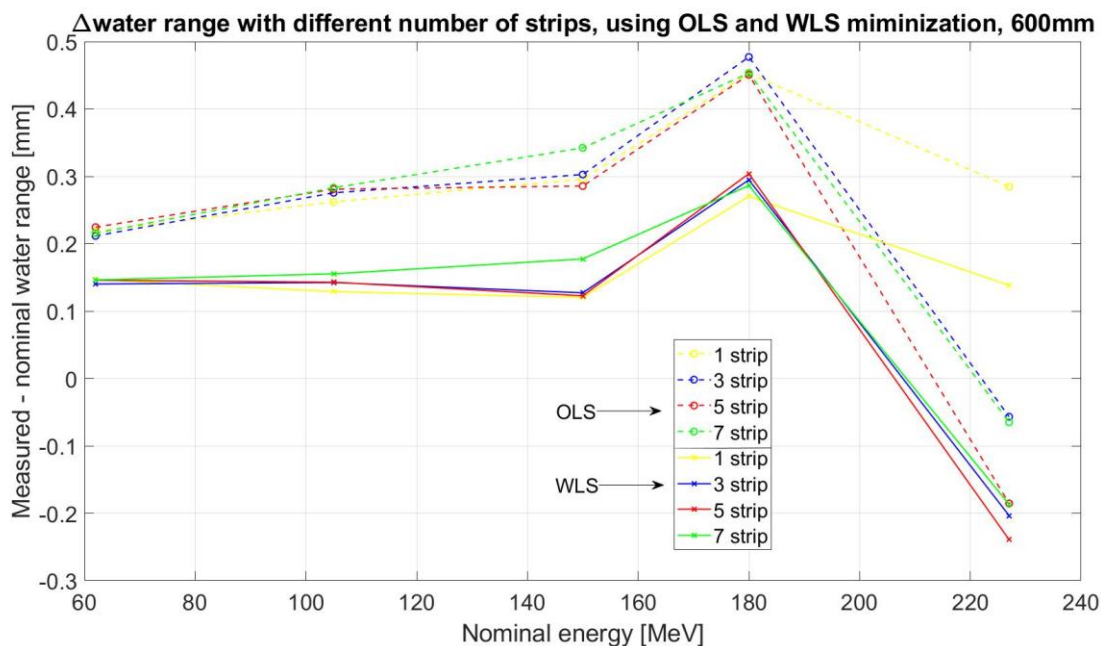


Figure 4.38: Difference between the nominal and the measured water range at 600mm.

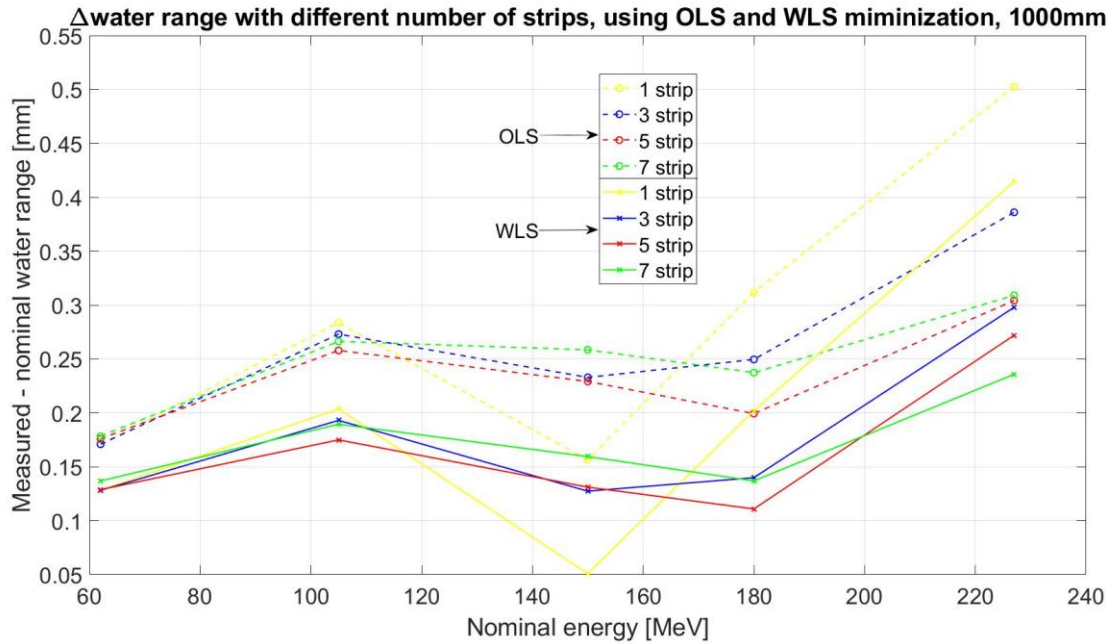


Figure 4.39: Difference between the measured and the nominal water range at 1000mm.

All the  $\Delta range$  remain within the 1mm limit for any energy, at 600 and 1000mm (respectively, Fig. 4.38 and Fig. 4.39). The results (WLS and OLS minimization) are very close, but for the majority of the points, the distances (from  $x_1$ ) and the *offset* coming from the WLS minimization lead to better energy estimation, therefore of the water range.

The results, collected as  $\sum residual_{water\ range, 600-1000mm}^2$ , for the OLS and WLS minimization, are reported in Figure 4.40.

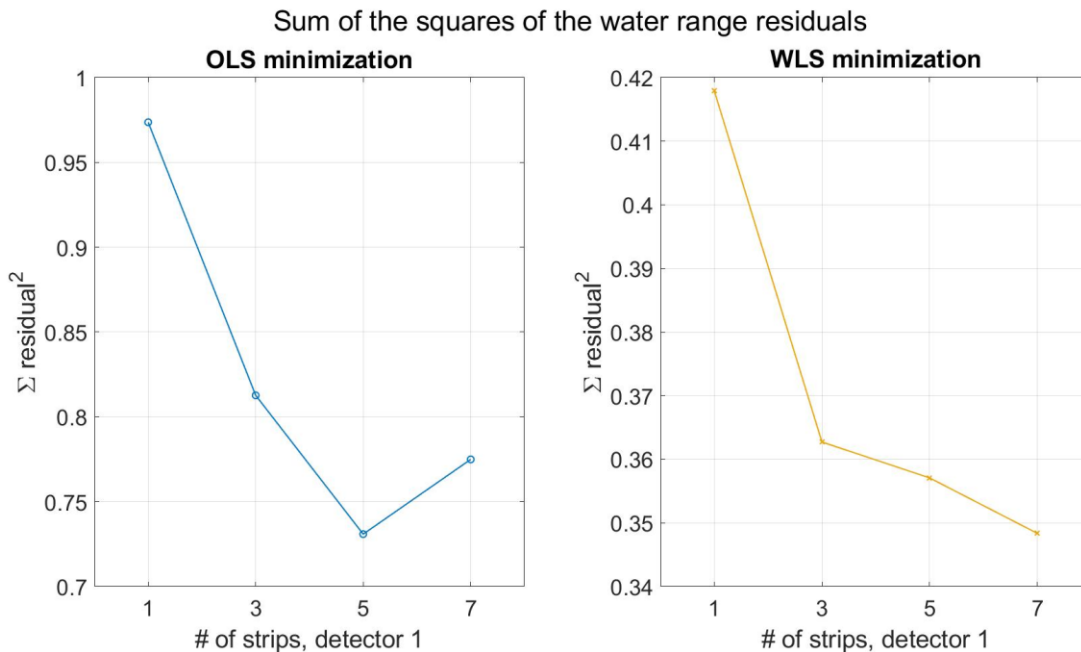


Figure 4.40: Sum of the residuals of Fig. 4.38 and Fig. 4.39, adopting the OLS and WLS minimization. There is, increasing the number of strips ( $x$ -axis), a reduction of the residual.

First, it can be noticed, that the values, on the left-hand side of the picture are bigger (Fig. 4.40). So, at the end, this can be written as a prove of the convenience of weighting the residuals. Second, the increase in the number of the strips of the first sensor considered in the TOF measurements lead to better results, besides the point at 7 strips for the OLS minimization. In particular, looking at the

figure on the right side (WLS minimization), going from 1 strip to 3, has a major impact than the following increases. It may be sign of a plateau.

Trying to summarize the results of this final analysis, the increase in the statistics seems to lead to a better evaluation of the beam penetration range. However, to be more confident about this result, this entire analysis must be repeated with experimental signals.

## 5. Conclusions

The work described in this thesis aims at developing a new technology for the real-time analysis of clinical proton beams, leading to a practical application of new treatments like rescanning and tracking, proposed to compensate for organ movements. These two proposed techniques allow a more precise and effective treatment of the tumor reducing the dose delivered to healthy tissues, using different approaches. These two methods cannot be applied with the actual beam monitoring system (Ionization Chambers), which does not measure the energy of the beam and has a certain threshold below which is not able to detect the crossing charged particles.

The measurements presented in this work are divided into two three main groups:

- The analysis of the signals experimentally acquired in CNAO and in TPT, with only one channel readout per detector, through the implementation of a MATLAB application;
- The calibration of the prototype system, needed to estimate the time offset and the distance between the sensors in the telescope;
- The simulation and the analysis of signals of a specifically designed detector (segmented in 8 strips), through the implementation of two MATLAB applications.

In the first part, there is a description of all the issues related to the analysis of the signals, in terms of noise generated and pileup effects, but also of the beam characteristics of the two facilities in which the tests have been conducted. These aspects have been considered writing the code of the MATLAB application. The program, analyzing the signals, detects the peaks in the first detector (of the telescope), and stores all the coincident signals of the second sensor, within a certain sample window (the duration is setup from the user interface). For each coincidence, the code stores the measured time of flight. At the end of this process, a histogram of the measured TOF (the time between the possible coincident signals between the two sensors) shows a peak and some false coincidences. The latter are differently distributed, depending on the type of accelerator producing the beam.

Two methods have been implemented to treat the coincident signals, named *3-sigma method* and *second gaussian method*.

The main results can be summarized as follow:

- The application is able to read the signals in a relatively short amount of time (3-4 seconds per 1000 events, with each event that lasts 204.8 ns), but still not enough for the future on-line applications, which require the TOF measurement within few milliseconds.

The TOFs measured with the *3-sigma method* have an error of the order of few ps. This has been the first method implemented, with the idea of treating the coincidences of the main peak of the histogram only. This objective is achieved reducing the spectrum of the coincidences evaluated, to a window with a certain range (half-width set up from the user interface). From the gaussian fit of the coincidences the mean TOF is measured within this window. The limitation of this method relies in the false coincidences that are still present at the base of the main peak of the histogram, that are not removed.

The *second gaussian method* (second method developed) tries to solve this issue. A double gaussian fit of all the coincidences stored inside the histogram is performed. Then, there is a subtraction of the coincidences of the histogram and the ones below the bottom gaussian (of the double gaussian fit). The mean TOF is defined from the single gaussian fit of the left coincidences. The error over the TOF is almost always smaller than 1 ps. This method proves a certain adaptability. Indeed, the distribution of the coincidences in the histogram is affected by the beam characteristics. The coincidences coming from the tests in CNAO have a constant background, while the ones coming from the tests in TPT have a radiofrequency peak at the base main peak of the histogram. The bottom gaussian, of the double gaussian fit, assumes, automatically, the shape of these false coincidences profile that are effectively removed.

Considering the setup used during the data acquisition, the main sources of error are related to the distance between the two sensors and to the time offset. Therefore, with the TOFs measured in the first part, the system must be calibrated in terms of distance and time offset. In the second part of the thesis two methods have been developed to calibrate the system, named *absolute approach* and *relative approach*. The first method uses the nominal energies and the TOFs measured as input and calibrates the system through a  $\chi^2$  minimization, keeping the distances and the time offset as free parameters. The second method is independent from the nominal energies and calibrates the system through an OLS and WLS minimization. The TOFs are still used as inputs, but there are only two free parameters: the first distance between the two detectors, involved in the data acquisition, and the time offset. All the other distances are expressed as function of the first one plus a certain, constant or not,  $\Delta x$ . The two free parameters are free to range over an interval of values.

Once calibrated, it is possible to measure the energy of the beam from the TOFs values, the distances and the time offset through an analytical approximation validated with Geant4 simulations, taking into account the energy loss in the air between the sensors (Appendix B). From the energy, the range in liquid water is measured. This is the relevant parameter in clinics, and it must be very precise. Indeed, the limit imposed by the regulation is of 1mm between the range measured and the nominal one. The following is a recap of the second part of the thesis:

- The beam energies measured with distances and time offset resulting from the *absolute approach* are very close to the nominal values. The  $\Delta energies$  profile gets better increasing the distance, as expected (the error over the distance has a small impact at big distances between the detectors). The difference in the water range measured from these energies and the nominal one, at 67 and 97 cm, are always smaller than 1mm. These good results are, though, reached using the nominal energies.
- Moreover, the beam energies coming from the results of the *relative approach* are very close to the nominal values, even though the ones coming from the *absolute approach* are better. The  $\Delta energies$  profile is the same, improving at big distances. There is a discrepancy between the results of the type of minimization adopted during the calibration procedure (OLS and WLS minimization) in terms of range in water measured. At 67 and 97 cm, the  $\Delta ranges$  from the OLS minimization are quite always over the 1mm limit. Better results are obtained from the WLS minimization, but still worse than the ones of the *absolute approach*. Besides these results, the *relative approach* has been developed mostly thinking about the new prototype system involved in the data acquisition. Indeed, In the actual prototype system, the position of S<sub>2</sub> could be changed by removing it from its first position in specific grooves of the support platform and moving it to a second position corresponding to other grooves of the same platform. While the future prototype system will move S<sub>2</sub> mechanically, with a bigger precision over the position and maintaining an eventual inclination. This will remove the uncertainties over the possible tilt of the detector, leading to a more precise estimation of distance and time offset.
- Another analysis performed and reported in Appendix C, is about the combination of energies that should be used to perform the calibration with the *relative approach* (that uses the TOFs measured at just two energies). Because of the dependence between distance and time offset, it has been developed a method to find out which is the combination that minimize this dependency (the one with the smallest correlation index). For both facilities, the best combination is always the one between the smallest and biggest energy, from the ones involved in the tests conducted.
- Although not been reported in the thesis, the analysis of the time offset of the first 4 input channels of the digitizer (0 to 3) has been performed. This work helped me to become familiar with the digitizer and to verify if a time delay between the channels is contributing to the measured time offset. Two identical signals have been generated and acquired by the digitizer with two cables of different length. The difference in length corresponds to a certain time

delay. The signals have been acquired by switching the cables and measuring the TOF with the MATLAB application described before (already knowing the correct TOF, the time delay due to the cables). For example, the channels 0 and 3 (of the digitizer) are the ones involved in the experimental tests conducted in CNAO and TPT. From this analysis, the time offset of this combination of channels results of 87 ps, measured as  $offset = \frac{TOF_{0-3} - TOF_{3-0}}{2}$ . Repeating this procedure for all the other combinations of the first four channels the offset results different for each of them.

The sensors used at CNAO were made up of 4 pads, each of them with 80 $\mu$ m of active thickness and 3x3mm<sup>2</sup> of sensitive area. To reduce the effect of the pileup, the detector has been segmented in strips, as the one used for the tests in TPT (each strip with active thickness of 50  $\mu$ m and 2.2mm<sup>2</sup>). In both cases, only one channel per detector has been readout, because of the available HV readout boards. The energy measurement in a shot-by-shot time frame, as required by possible future applications, needs a duration of few milliseconds of the whole process of collecting the data, analyzing the signals and measuring the energy. Increasing the number of the strips readout per detector (increasing the statistics), it is possible to shorten the time the system takes.

The final part of the thesis (fourth chapter) is focused on the extension of the application (second chapter) for the analysis of 2 signals (1 channel per detector) to 16 signals (8 channels per detector). The method involved in the analysis of the events is basically the same, but it is extended to multiple signals. Before proceeding with the experimental tests, the application must be validated with simulated signals, specifically designed by another MATLAB application. The beam has been simulated with Geant4, at different energies and distances between S<sub>1</sub> and S<sub>2</sub>:

- 60, 300, 600 and 1000 mm of distances.
- 62, 150, 228 MeV (plus another two energy levels, 105 and 180 MeV for the validation of the *relative approach* of the calibration).

The measurement app offers the possibility of choosing which combination of strips of the two detectors to evaluate by checking the boxes over the user interface. The analysis performed in this part involved three approaches: facing strips, all 64 combinations combined, or all 64 combinations singularly evaluated (strip-by-strip analysis). The idea of diversifying the strategy is to find out which is the best approach, in terms of precision of the results but also about the amount of time the analysis takes. A further use of these evaluations is about the spread out of the flux at different energies and distances.

To detect the coincident signals, the two methods implemented for the first version of the applications (*3-sigma* and *second gaussian*) have been employed in the measurement app. The analysis of the final results has been made considering the parameters setup in the simulations as the nominal values.

A summary of the results:

- Combining the coincidences coming from all the 64 combinations, the *second gaussian method* proved to be more precise of the *3-sigma* one, in terms of  $\Delta TOF$  with respect to the nominal values (the nominal TOF is the one that comes from the simulation), that ranges between [-1;1] ps for the first method, and [-1;2] ps for the second one;
- Adopting the *second gaussian method* for the facing strips analysis, the outcomes are pretty much the same of the previous analysis, with the  $\Delta TOF$  that ranges between [-1;1] ps with respect to the nominal TOFs. Therefore, it is not always necessary to study all the combinations;
- The strip-by-strip analysis (64 combinations evaluated singularly) measures the TOF for each combination of strips of the first and second detector (adopting the *second gaussian method*). The results are not better, in terms of  $\Delta TOF$ , with respect to the ones coming from the facing-strips or the 64 combinations combined analysis. There are though, some conditions, underlined in the fourth chapter in which it may be interesting the evaluation of what happens

in every single combination. Indeed, at small energies and high distances, the spread out of the flux is important. This turns in a decrease of the coincidences collected over the combinations of the facing-strips, with a general homogenization over the whole volume of the detector. But, in other situations, high energy and small distances, the lack of coincidences in some combinations leads to absurd results that must be properly faced;

- To face this problem, the final form of the strip-by-strip analysis combines the two methods to treat the coincidences, removing the possibility of having meaningless results. There are still no improvements in terms of precision of the results with respect to the facing strips or 64 combinations combined analysis;
- In the end, the best way to treat these 16 signals is to collect all the coincidences together and treat them with the *second gaussian method* (64 combinations combined analysis);
- One application of the strip-by-strip analysis is to characterize the spread out of the beam to perform an alignment evaluation of the two detectors. Because of the setup of the system, detectors attached at the passive board, held by rigid supports, there is the possibility of a wrong positioning of the two sensors. Having the exact dispersion of the particles at the origin (therefore an exact idea of how the coincidences should be arranged over the first detector) is it possible to evaluate a possible misalignment. The results coming from this first preliminary simulation proved to be good, but there are still some limitations to the method. Indeed, even though it shows clearly the misalignment at short distances, because of the uncertainties over the distance the result cannot be taken for granted. At high distances, the analysis cannot be performed because of the homogenization of the coincidences over the strips of the detector.

In the final part of the fourth chapter, using the results of the 16 signals analysis, two more analysis have been performed: the validation of the calibration method with the *relative approach* and how the results change, in precision, increasing the number of strips involved in the measurements.

For these additional evaluations, two more simulations have been conducted: at 105 and 180 MeV. The code for the calibration with the *relative approach* (OLS and WLS minimization) takes the TOFs measured and a certain range for the first distance ( $x_1$ ) and the time offset. To consider the system “validated”, the results of the calibration must be the first distance, imposed in the simulation (60mm), and a time offset equal to 0, because of the physical lack of wires and digitizer.

The second analysis must go through the calibration, to define the distances and the time offset, required, with the TOFs, to measure the beam energy. With the energy, the range in liquid water has been measured and compared with the one of the nominal energies (the ones imposed in the simulations).

- The results of the calibration validate the method developed. The results of the WLS minimization are better than the ones of the OLS minimization, like in the third chapter. Respectively, the WLS provides :  $x_1$  of 60.37 mm and *offset* of -2 ps, while for the OLS:  $x_1$  of 61.28 mm and *offset* of -7 ps. The first distance and the time offset are very close to the nominal values, and measuring the beam energy, the behavior is the expected one, with  $\Delta energy$  that gets better increasing the distance.
- For the second analysis, it has been measured the sum of the squares of the residuals, in terms of  $\Delta range$ , coming from the nominal and measured energies, at 60 and 100cm. For all the simulations (5 energies, 4 distances), it has been considered an increasing number of strips of the second detector: 1,3,5 and 7. The beam flux distribution over the detector is not uniform, but it is a gaussian centered in the middle point of the sensor. Therefore, the first strip considered is the one at the center (strip 6) of the sensor. The analysis, keep increasing the number of the strips, peeks the strip below and above the previous considered (strip 6, strip 5 to strip 7, etc.). Applying OLS and WLS minimization for the calibration (*relative approach*) of the system (distance and time offset are necessary to evaluate the beam energy, in this approach), there is, almost, always a decrease of the residual, proving the statement. In

particular, going from 1 strip to 3 strip presents the major improvement in terms of reduction of the residual. WLS minimization proved to be more precise than the OLS one.

There are still some open-points and analysis that must be conducted prior to applying this new detector for experimental tests in the two facilities.

First, after the validation with simulated signals, the MATLAB application must be tested with real signals, specifically generated with a pulse generator. This device must satisfy some conditions to be applied, like it should provide the possibility of generating random peaks at a certain, minimum frequency (to stress the code), and it should have 16 output channels. These 16 signals are delivered to the digitizer with 16 wires, 8 per detector. The ones of the second detector are longer than the ones of the first sensor, to simulate a certain time delay (known), that must be compared with the result of the application. After this validation, more experimental data must be collected in the two facilities, and the whole process must be repeated:

1. Collection of the data, with the signals digitized and stored;
2. TOF measurement with the MATLAB application;
3. Calibration of the system in terms of distance and time offset;
4. With the outcomes of the calibration and the TOF, the beam energy is measured;
5. From the beam energy, the range in liquid water is evaluated;
6. Check if  $\Delta range$  satisfy the 1mm limit imposed by the regulation.

This process takes a while. The step 2, on its own, takes around 40 seconds for the analysis of 1000 events. The number of events of the simulated signals (fourth chapter) is about 20 thousand; therefore, the application takes several minutes to determine the TOF. Aiming for a complete assessment of the energy in few milliseconds, there is still a lot to improve. The plan is to parallelize the code, assigning over different processors: the analysis of an equal number of events and then putting all the results together, or the analysis of the different strips.

Some preliminary tests showed a consistent improvement of performance of the code, but still a lot of work must be done to achieve the final goal.

Other tests, for a validation of the code with computational simulated signals, can be made setting up different parameters of the beam, like the distribution or increasing the number of particles.

The last addition, planned so far, is the improvement of the preliminary tool, presented in the end of the fourth chapter, for the study of a misalignment of the detectors over the three axes.

In conclusion, I had the chance to be involved in the development of the energy measurement device of the MoVeIT project, when the project was in a particularly challenging status. Indeed, I started analyzing the data of the first experimental tests and I then continued developing the methods and the instrumentations to move to the second step of the project, i.e. the improvements of the analysis code and the simulations of a more complex set of input data. Therefore, I had the opportunity to either deeply contribute to specific tasks of the project and have a global overview of the whole project at the same time, helping the medical physics group of UniTo, enlarging my interests and improving my knowledge at the same time.

# Appendix A.

The screenshot displays the 'Signal Analysis (Timing)' interface of a TOF measurement application. The interface is divided into two main sections: 'Signals' and 'Analysis result'.

**Signals Section:**

- Folder:** A text input field for the folder path.
- Signals file name:** A text input field containing 'signals\_simulation.mat'.
- Input Options:** Radio buttons for 'Matlab (.mat)', 'binary', and 'out\_N'. The 'binary' option is selected.
- Signal Files:** Text input fields for 'signal1: wave\_0.dat' and 'signal2: wave\_3.dat'.
- Columns:** Spinners for 'signal1=column: 1' and 'signal2=column: 2'.
- Event Settings:** Spinners for 'Initial Event: 1', 'Events to jump: 1', and 'Final Event: 0'.
- Buttons:** 'Load data info', 'Preview', and a checked checkbox for 'Invert signal'.
- Analysis Parameters:** Spinners for 'Signal Threshold: 200', 'Constant fraction: 0.8', 'Samples window: 50', and 'Bin size: 0.2'. There are also checkboxes for 'reject pileup' (checked) and 'view constan fraction' (checked), and a spinner for 'min. pileup peak size: 2'.
- First fit:** Radio buttons for 'Simple Gaussian' and 'Double Gaussian' (selected).
- Second fit:** A spinner for 'Second fit half width (sigma fraction): 1.5'.
- Action Buttons:** 'Analyse' (blue) and 'Close all figures' (orange).

**Analysis result Section:**

- A large empty rectangular area for displaying the analysis results.
- File Name Inputs:** 'Analysis file name: timing\_analysis.txt', 'Delta times variable: delta\_times.mat', and 'Histogram figure name: TOF\_histogram.fig'.
- Save Button:** 'Save analysis' (blue).

**Steps for analysis:**

- 1- Define the path to waves.dat files.
- 2- Press the button Load data info.
- 3-Optional: You can see a preview of the data defining initial: final and events to ...
- 4- Define or check the analysis parameters.
- 5- Press button Analyse.
- 6- Save the analysis results defining a new file name if desired.

Figure a.1: TOF measurement app interface.

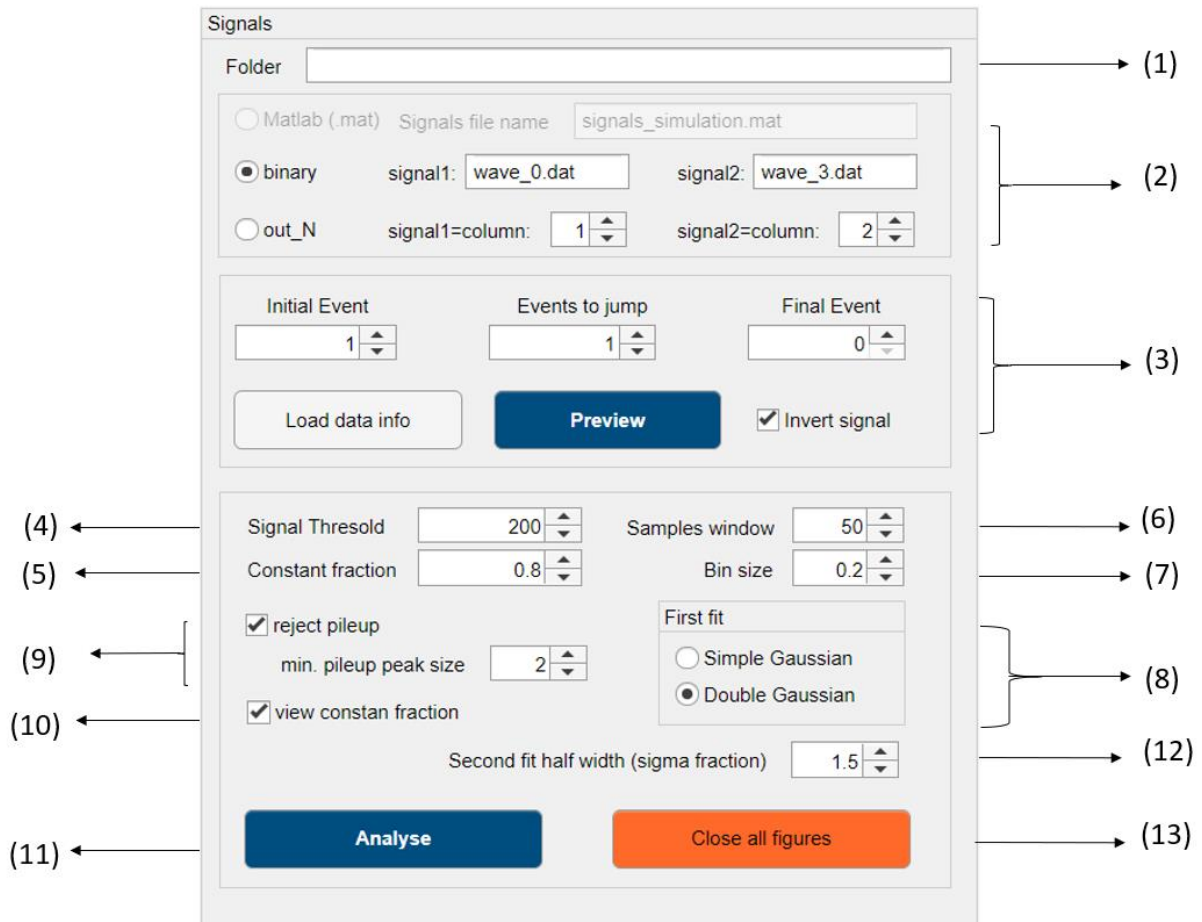


Figure a.2: Zoom of the Fig. a.1. These are the parameter that can be modified before the analysis of the signals.

Meaning of all the boxes of the measurement app (Fig. a.2):

1. Folder in which the data of the acquisition are stored;
2. Decide the format of the data. Binary for the TPT acquisition and the other for CNAO;
3. Pressing the button *load data info*, the code loads the signals acquired, showing the total number of event (final event). The analysis can be performed on a selected number of events (by modifying initial and final event) one by one or modifying the step (events to jump). Pushing preview, the code shows the first ten events stored of the two signals;
4. Signal threshold, expressed in ADC counts;
5. Percentage supplied to the constant fraction discriminator method;
6. Length of the sample window, expressed in samples;
7. Size of the bin for the final histogram that collects the coincidences;
8. Double or single gaussian fit for the final histogram;
9. Checking the box, the code rejects the pileup. *Min. pileup peak size*, is the number of samples used to identify a pileup ;
10. Shows in the preview, for each peak, the point in which the signal reaches the percentage indicated in (5);
11. Start the analysis;
12. Half width used in the first method developed to treat the coincidences to narrow the coincidences' window around the main peak of the histogram;
13. Close all figures opened.

## Appendix B.

The dependency between velocity and kinetic energy is not linear (Fig. b1). There is a mismatch between the energy measured from the average velocity, between the two detectors of the telescope, and the average energy, measured from  $K_2$  and  $K_1$ , defined, respectively, as the energy before  $S_2$  and the energy right after  $S_1$ .

$$K(v_{avg}) = E_0 \left( \frac{1}{\sqrt{1 - \left(\frac{v_{avg}}{c}\right)^2}} - 1 \right) \quad (b.1)$$

Equation b.1 calculates the energy from the average velocity, with  $c$ , speed of light, and  $E_0$ , the rest mass of the proton, and considering  $v_{avg}$  as:

$$v_{avg} = \frac{v(K_1) + v(K_2)}{2} \quad (b.2)$$

The energy, as average between  $K_1$  and  $K_2$ , is measured as:

$$K_{avg} = \frac{K_1 + K_2}{2} \quad (b.3)$$

$$v(K_{avg}) = c \sqrt{1 - \frac{E_0^2}{(E_0 + K_{avg})^2}} \quad (b.4)$$

with Equation b.4, that calculates the average velocity from the average energy (Eq. b3).

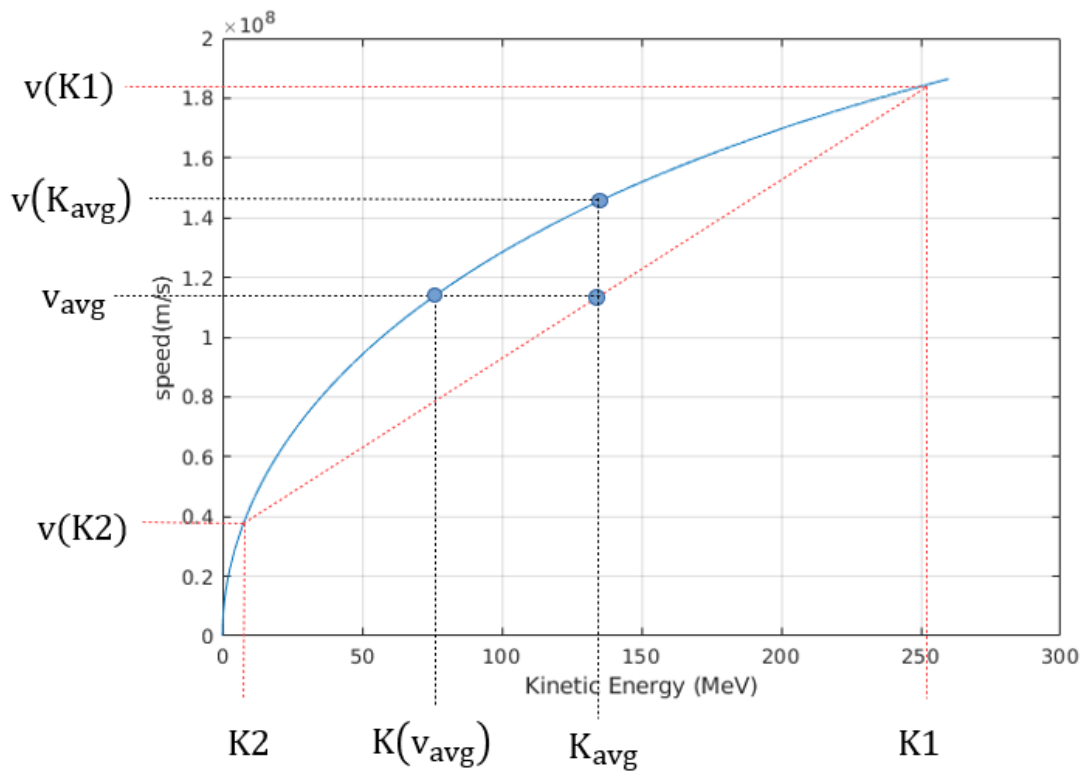


Figure b.1: : The blue curve is the speed of the proton from the relativity theory. This figure shows that a linear approximation between speed and energy does not work.

Figure b.1 shows that:

$$v_{avg} \neq v(K_{avg})$$

$$K_{avg} \neq K(v_{avg})$$

The range of energies of interest for hadron therapy applications goes from 60 MeV to 250 MeV. In this interval, Figure b.1 proves that there is no linearity between velocity and energy. However, the energy lost by the proton is very small compared to the beam energy.

From Monte Carlo simulations, the energy lost in 97 cm of air is reported in Table b.1.

Table b.1: Energy profile going from  $K_0$ , before  $S_1$  (at the isocenter).  $K_1$  after  $S_1$ ,  $K_2$  before  $S_2$ .  $\Delta K$  is the total energy lost in this path, between  $S_1$  and  $S_2$ .

$K_0$ [MeV]	$K_1$ [MeV]	$K_2$ [MeV]	$\Delta K$ [KeV]
59	58.7	57.6	1100
150	149.8	149.3	500
230	229.9	229.5	400

The linearity, in these small energy ranges, can be proved with an analytical demonstration and with a Monte Carlo simulation.

For the analytical approach,  $K_2$  is written as function of  $K_1$  and  $\Delta K$ :

$$v(K_2) = v(K_1 - \Delta K) = c \sqrt{1 - \frac{E_0^2}{(E_0 + K_1 - \Delta K)^2}} \quad (b.5)$$

Taking the Taylor series of  $v(K)$  (Eq. b.5) around  $\Delta K$ , it can be demonstrated the linearity in that small interval (Fig. b2).

$$v(K) = v_1 + \frac{c^2 E_0^2}{v_1(E_0 + K_1)^3} (\Delta K) \quad (b.6)$$

with,

$$v_1 = c \sqrt{1 - \frac{E_0^2}{(E_0 + K_1)^2}}$$

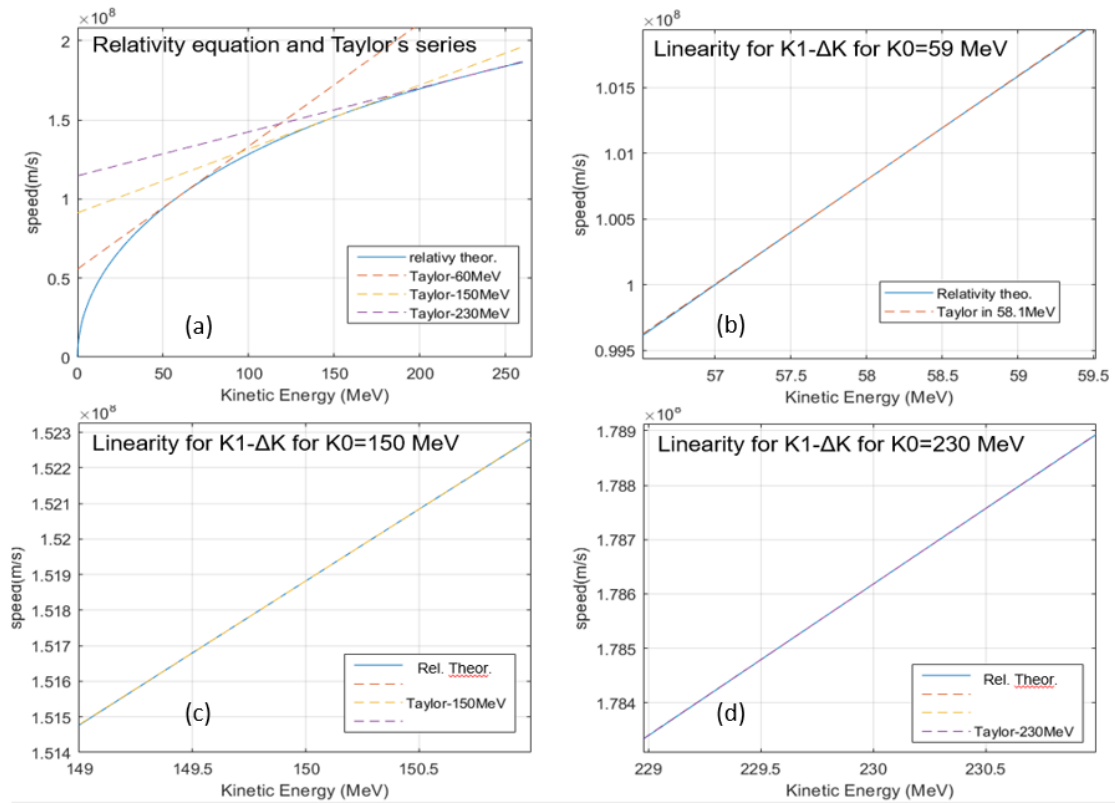


Figure b.2: Demonstration of the linearity between energy and velocity. (a) represents the behavior of the velocity as function of the energy over the interval 0-250 MeV, applying Eq. b.1 (relativity theory) and Eq. b.6 (Taylor expansions). (b), (c) and (d) prove the linearity representing the profile of the velocity as function of the energy over small intervals of energy (the ones of Table b.1).

The linearity of the energy lost through the air, and through the detector, has been proved also through a Monte Carlo simulation (Fig. b.3).

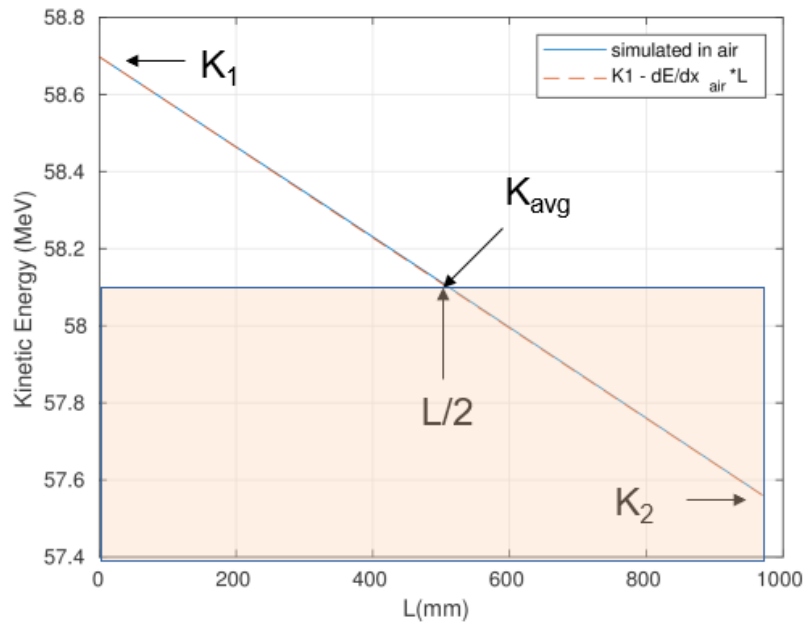


Figure b.3: Energy lost by a proton traveling through the air between 0 and 1000mm. The red line is  $K_2$  measured as  $K_1$  minus the stopping power in air times the covered distance. The blue line is the energy profile coming from a Monte Carlo simulation. The two profiles overlap.

Therefore, the average energy  $K_{avg}$  can be estimated as the mean energy between  $K_2$  and  $K_1$ .

## Appendix C.

It has been decided to perform the *relative approach* of the calibration of the system using two beam energies. Which would be the best combination of energies? The answer comes from the analysis of the correlation of distance and offset. The combination that guarantees the smallest correlation index between those two parameters has been decided to be the right one.

Considering the tests performed at CNAO (Table 3.2), assuming the  $S_1$  position being 0, two  $S_2$  positions (either 7-97, or 37-97, or 67-97) are considered in this study. With 97 cm that is kept fixed because less affected by the error over the distance. For each combination of  $S_2$  positions, the velocity is defined as:

$$v_{1-2} = \frac{x_2 - x_1}{TOF_2 - TOF_1} \quad (c.1)$$

For instance, in the case 7-97 cm, the velocity from the TOFs measured from the tests conducted at the same  $K_1$  (energy at the isocenter) of 58.95 MeV is:

$$v_{7-97_{58.95}} = \frac{97-7}{t_{97_{58.85}} - t_{7_{58.95}}} \quad (c.1)$$

To avoid confusion with  $K_{avg}$  (i.e. the mean energy between  $S_1$  and  $S_2$ ), a new term of energy is introduced ( $E_k$ ) for the average energy between two  $S_2$  positions, defined from the average velocity as:

$$E_k \cong E_0 \left( \frac{1}{\sqrt{1 - \left(\frac{v_{avg}}{c}\right)^2}} - 1 \right) \quad (c.2)$$

From  $E_k$  it is possible to go back to  $K_1$ , considering the energy loss in air:

$$K_1 = E_k + \left(\frac{S}{\rho}\right)_{air} \cdot \rho_{air} \cdot \left(\frac{x_1 + x_2}{4}\right) \quad (c.3)$$

with  $x_1$  and  $x_2$  that are the two positions of  $S_2$ . The sum of these two values, divided by 4, is the mean distance between the points at which  $E_k$  is measured (half distance between  $x_1$  and  $x_2$ ) and  $S_1$ .

Table c.1 collects all the values of  $K_1$  calculated considering all the TOFs measured at 7 and 97 cm, at the same energy, in CNAO.

Table c.1: First steps of the best energy combination process. From the  $TOF_1$  and  $TOF_2$ , measured with  $S_2$  in position  $x_1$  and  $x_4$  come those velocity measurements (third column). Using Eq c.2, the energy between the positions is measured ( $E_k$ ), and calculating the energy loss in the air, the energy right after  $S_1$  can be measured.

<b>K<sub>1</sub> nominal [MeV]</b>	<b>TOF 7 cm [ns]</b>	<b>TOF 97 cm [ns]</b>	<b>speed [m/s]</b>	<b>E<sub>k</sub> [MeV]</b>	<b>K<sub>1</sub> [MeV]</b>
58.95	0.764	9.666	1.01E+08	58.38	58.69
77.6	0.691	8.549	1.15E+08	77.02	77.27
103.5	0.624	7.548	1.30E+08	102.95	103.15
148.5	0.554	6.508	1.51E+08	148.27	148.42
226.1	0.492	5.557	1.78E+08	226.73	226.84

Using these five values of  $K_1$  (Table c.1), knowing the four nominal distances, it is possible to measure 20 values of  $K_{avg}$  (5 values per distance) as:

$$K_{avg}(L) \cong K_1 - \left( \frac{S}{\rho} (K_1) \right)_{air} \cdot \rho_{air} \cdot \frac{L}{2} \quad (c.4)$$

Table c.2: From  $K_1$ , having the four nominal distances,  $K_{avg}$  is measured.

<b>K avg 7 cm</b>	<b>K avg 37 cm</b>	<b>K avg 67 cm</b>	<b>K avg 97 cm</b>
58.68	58.68	58.68	58.68
77.27	77.27	77.26	77.26
103.15	103.14	103.14	103.14
148.42	148.42	148.42	148.42
226.84	226.84	226.84	226.84

Table c.2 reports all the values of  $K_{avg}$  measured with Eq. c.4, starting from the energies ( $K_1$ ) collected in the last column of Table c.1, and using the four nominal distances (7,37,67 and 97cm). These energy values can be translated into average velocities between the two detectors ( $S_1$  and  $S_2$ ) as:

$$v(K_{avg}) = c \sqrt{1 - \frac{E_0^2}{(E_0 + K_{avg})^2}} \quad (c.5)$$

and used to give an estimation of the distance:

$$d = v (TOF - offset) \quad (c.6)$$

where  $TOF$  is known, as well as the velocity (Eq. c.5), but there are two unknowns,  $d$  and  $offset$ . Considering two  $TOF$ , measured with  $S_2$  at the same position, and two energies (therefore velocities), the Equation c.6 becomes a system of two equations with two unknowns:

$$\begin{cases} d = v_1 (TOF_1 - offset) \\ d = v_2 (TOF_2 - offset) \end{cases} \quad (c.6a)$$

Having 5 energies per distance, without repetition, the system c.6a can be solved 10 times.

For any distance, there are 10 energy combinations (for example, at 7 cm, the combinations of  $K_{avg}$  are, from Table c.2, first column, [row1, row2], [row1, row3], ...) that must be evaluated. The correlation index, to be measured properly, requires a certain statistic but there is a limited number of values of velocities to evaluate the variance, covariance and finally get to it. To increase the statistics, a gaussian distribution of 1000 points has been built for each velocity measured in the Eq. c.6a, centered at the mean velocity, with upper and lower limit as mean value  $\pm$  mean velocity error. Considering the 10 combinations of energies, with the increased statistics about the velocity, there are, for each distance, 20 thousand values of distances and offset to measure variance and covariance.

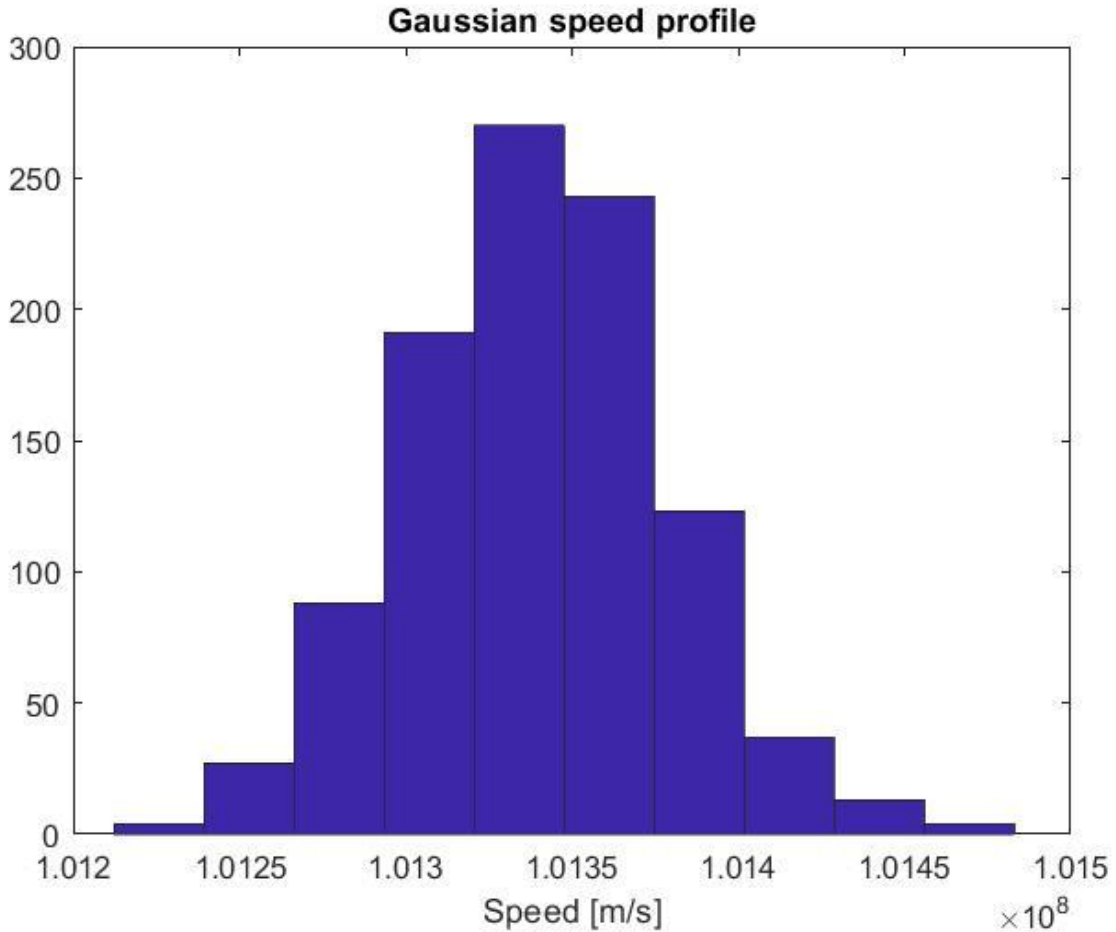


Figure c.1: Profile velocity from gaussian distributed random number generation around the mean value coming from eq c.5, and with the dispersion put as the error related to that measure.

Figure c.1 is an example gaussian coming from the velocity measured from 58.68 MeV ( $K_{avg}$ ), at 7 cm, from the combination of TOFs between 7 and 97 cm. The system of equations c.6a is written in order to let offset and distance as function of velocities and times, as:

$$offset_i = \frac{(v_{1_i} t_1 - v_{2_i} t_2)}{v_{1_i} - v_{2_i}} \quad (c.7)$$

$$distance_i = \frac{v_{1_i} v_{2_i}}{v_{1_i} - v_{2_i}} (t_2 - t_1) \quad (c.8)$$

The mean values are  $offset_{avg}$  and  $distance_{avg}$ , measured, through eq c.7 and eq c.8 with those 2000 points ( $v_{1_i}$  and  $v_{2_i}$ ), are used to measure variance and covariance:

$$\sigma_{offset}^2 = \frac{1}{n} \sum_{i=1}^n (offset_i - offset_{avg})^2 \quad (c.9)$$

$$\sigma_{distance}^2 = \frac{1}{n} \sum_{i=1}^n (distance_i - distance_{avg})^2 \quad (c.10)$$

$$cov_{offset,distance} = \frac{1}{n} \sum_{i=1}^n (offset_i - offset_{avg})(distance_i - distance_{avg}) \quad (c.11)$$

Finally, the correlation index is measured as:

$$\rho_{offset,distance} = \frac{cov_{offset,distance}}{\sigma_{offset} \cdot \sigma_{distance}} \quad (c.12)$$

All the results, for the analysis in CNAO, are collected in Table c.3, c.4 and c.5.

Table c.3: Correlation index, from CNAO TOF measurements. Distances combination: 7-97 cm.

7-97 cm		Correlation index			
Energy 1	Energy 2	7 cm	37 cm	67 cm	97 cm
58.95	77.6	-0.9981	-0.9981	-0.9980	-0.9980
58.95	103.5	-0.9921	-0.9920	-0.9921	-0.9929
58.95	148.5	-0.9801	-0.9813	-0.9814	-0.9816
58.95	226.1	-0.9566	-0.9620	-0.9572	-0.9617
77.6	103.5	-0.9980	-0.9982	-0.9981	-0.9980
77.6	148.5	-0.9910	-0.9907	-0.9898	-0.9914
77.6	226.1	-0.9968	-0.9761	-0.9724	-0.9771
103.5	148.5	-0.9972	-0.9975	-0.9971	-0.9971
103.5	226.1	-0.9885	-0.9879	-0.9877	-0.9874
148.5	226.1	-0.9969	-0.9969	-0.9970	-0.9969

Table c.4: Correlation index, from CNAO TOF measurements. Distances combination: 37-97 cm.

37-97 cm		Correlation index			
Energy 1	Energy 2	7 cm	37 cm	67 cm	97 cm
58.95	77.6	-0.9982	-0.9982	-0.9980	-0.9981
58.95	103.5	-0.9923	-0.9920	-0.9922	-0.9930
58.95	148.5	-0.9808	-0.9820	-0.9820	-0.9823
58.95	226.1	-0.9575	-0.9629	-0.9576	-0.9620
77.6	103.5	-0.9980	-0.9982	-0.9982	-0.9981
77.6	148.5	-0.9912	-0.9908	-0.9902	-0.9917
77.6	226.1	-0.9775	-0.9765	-0.9728	-0.9774
103.5	148.5	-0.9974	-0.9976	-0.9973	-0.9973
103.5	226.1	-0.9887	-0.9882	-0.9881	-0.9877
148.5	226.1	-0.9970	-0.9970	-0.9971	-0.9970

Table c.5: Correlation index, from CNAO TOF measurements. Distances combination: 67-97 cm.

67-97 cm		Correlation index			
Energy 1	Energy 2	7 cm	37 cm	67 cm	97 cm
58.95	77.6	-0.9981	-0.9981	-0.9984	-0.9982
58.95	103.5	-0.9923	-0.9923	-0.9925	-0.9926
58.95	148.5	-0.9801	-0.9798	-0.9815	-0.9815
58.95	226.1	-0.9616	-0.9616	-0.9626	-0.9658
77.6	103.5	-0.9980	-0.9981	-0.9979	-0.9980
77.6	148.5	-0.9896	-0.9899	-0.9911	-0.9901
77.6	226.1	-0.9783	-0.9762	-0.9740	-0.9774
103.5	148.5	-0.9969	-0.9970	-0.9970	-0.9970
103.5	226.1	-0.9863	-0.9886	-0.9880	-0.9862
148.5	226.1	-0.9964	-0.9968	-0.9969	-0.9968

The same procedure has been followed for TPT (Table c.6 and c.7), in which there are less distances and energy levels. One difference with respect to the test performed in CNAO is that the tests at different positions involve different beam energies. In this case: at 270 mm, there are 5 energies, at 670 mm, 6 energies, and at 970 mm there are 7 energies. Only the beam energies in common can be used for this process. Another problem related to the nominal energies in TPT is about one shot performed with S<sub>2</sub> at 270 mm. Instead of 97 MeV, the test has been performed at 98.5 MeV. Therefore, it was not possible to use that beam energy for this kind of analysis. There are only three beam energies in common.

Table c.6: Correlation index, from TPT TOF measurements. Distances combination: 27-97 cm.

27-97 cm		Correlation index		
Energy 1	Energy 2	7 cm	37 cm	67 cm
68.3	182.7	-0.9842	-0.9855	-0.9852
68.3	227.3	-0.9812	-0.9820	-0.9820
182.7	227.3	-0.9992	-0.9993	-0.9993

Table c.7: Correlation index, from TPT TOF measurements. Distances combination: 67-97 cm.

67-97 cm		Correlation index		
Energy 1	Energy 2	7 cm	37 cm	67 cm
68.3	182.7	-0.9870	-0.9872	-0.9869
68.3	227.3	-0.9844	-0.9845	-0.9871
182.7	227.3	-0.9993	-0.9993	-0.9993

For all the combinations examined and at any distance the smallest correlation index is always the one between the maximum and the minimum energy tested.

# Appendix D.

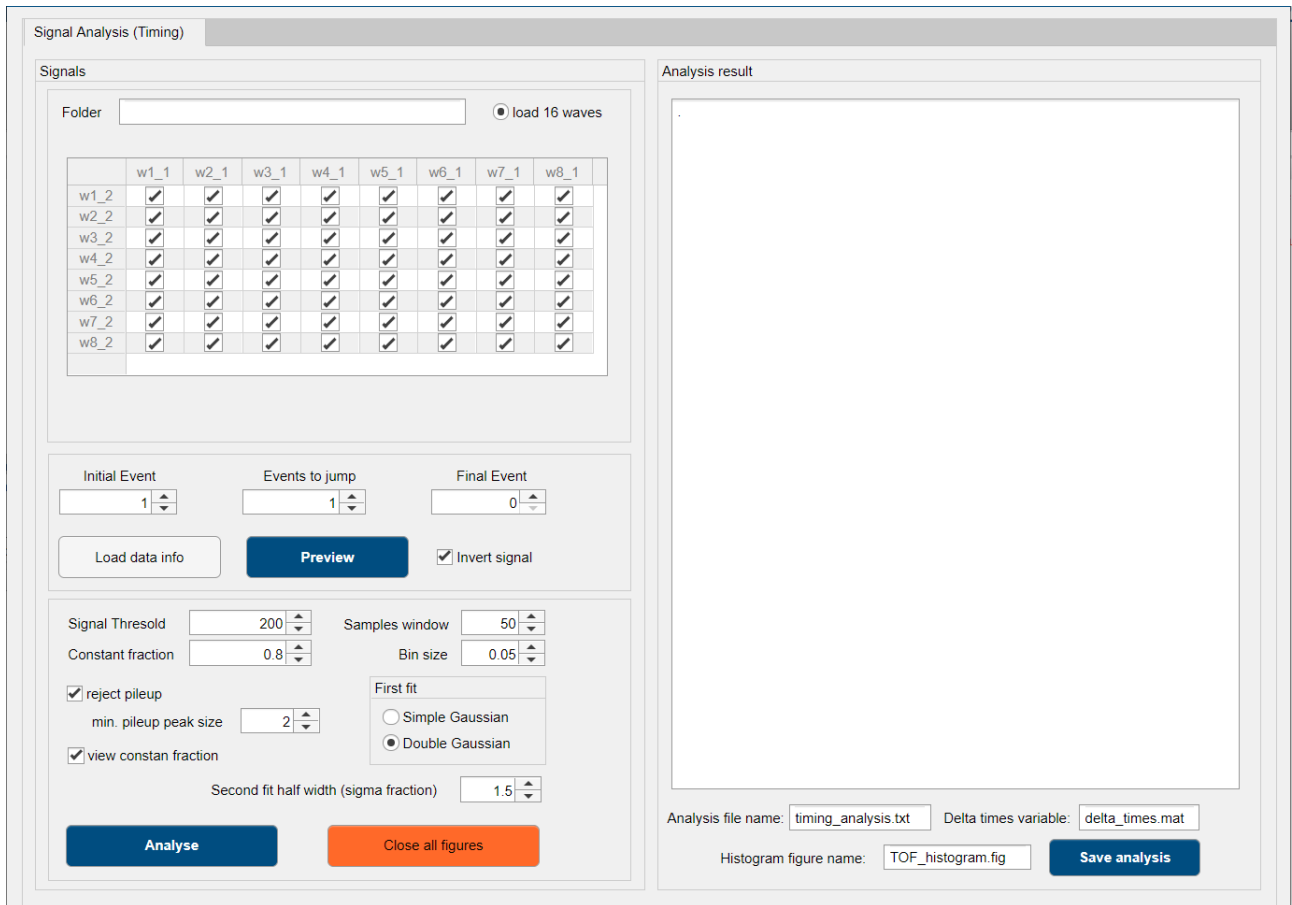


Figure d.1 : Interface of the TOF measurement app.

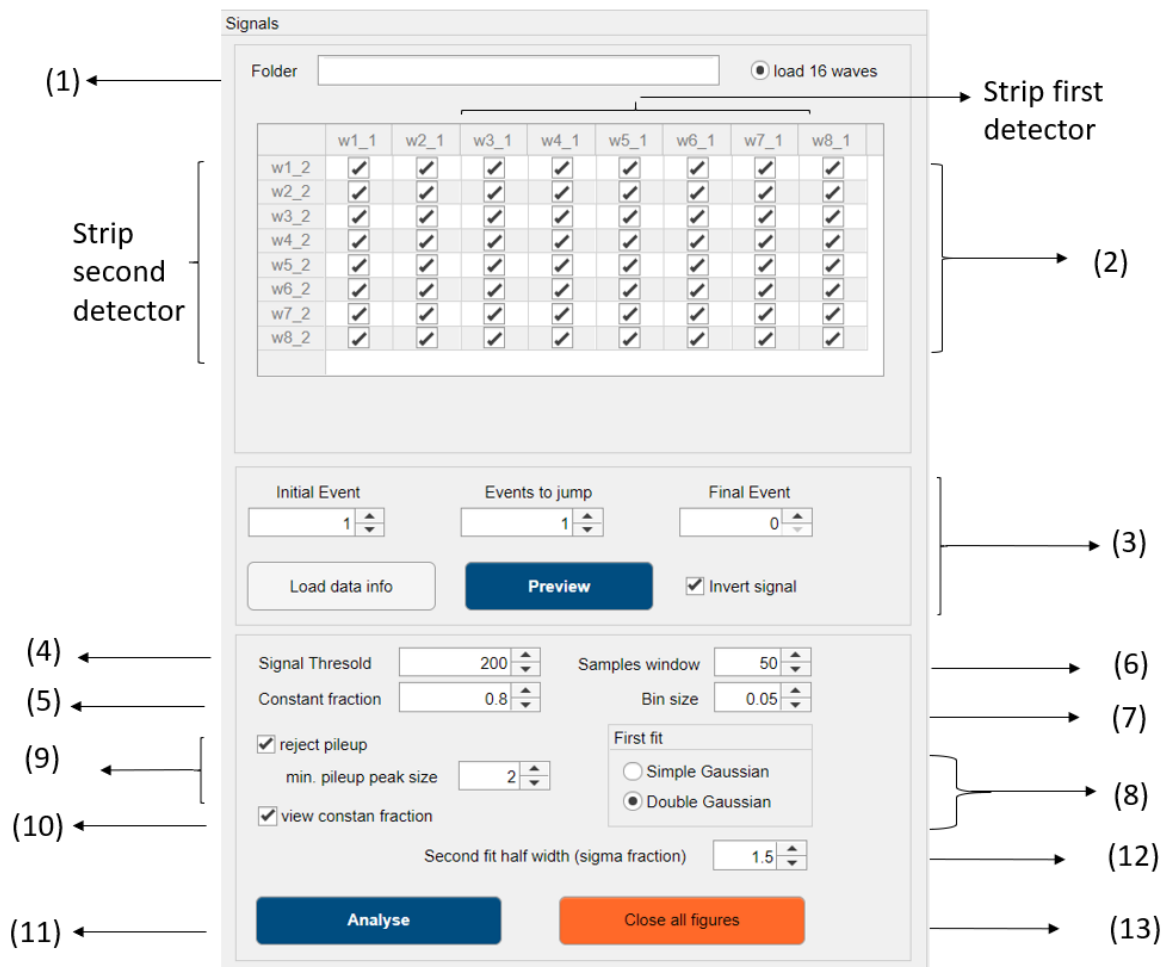


Figure d.2 : Zoom of the Fig. d.1. These are the parameter that can be modified before the analysis of the signals.

Meaning of all the boxes of the measurement app (Fig. d.2):

1. Folder in which the data of the acquisition are stored;
2. These boxes represent all the 64 possible combinations of the 8 strips for each detector. By checking one box, the program considers that combination to collect coincidences.
3. Pressing the button *load data info*, the code loads the signals acquired, showing the total number of event (final event). The analysis can be performed on a selected number of events (by modifying initial and final event) one by one or modifying the step (events to jump). Pushing preview, the code shows the first ten events stored of the two signals;
4. Signal threshold, expressed in ADC counts;
5. Percentage supplied to the constant fraction discriminator method;
6. Length of the sample window, expressed in samples;
7. Size of the bin for the final histogram that collects the coincidences;
8. Double or single gaussian fit for the final histogram;
9. Checking the box, the code rejects the pileup. *Min. pileup peak size*, is the number of samples used to identify a pileup ;
10. Shows, in the preview, for each peak, the point in which the signal reaches the percentage indicated in (5);
11. Start the analysis;
12. Half width used in the first method developed to treat the coincidences to narrow the coincidences' window around the main peak of the histogram;
13. Close all figures opened.

# Appendix E.

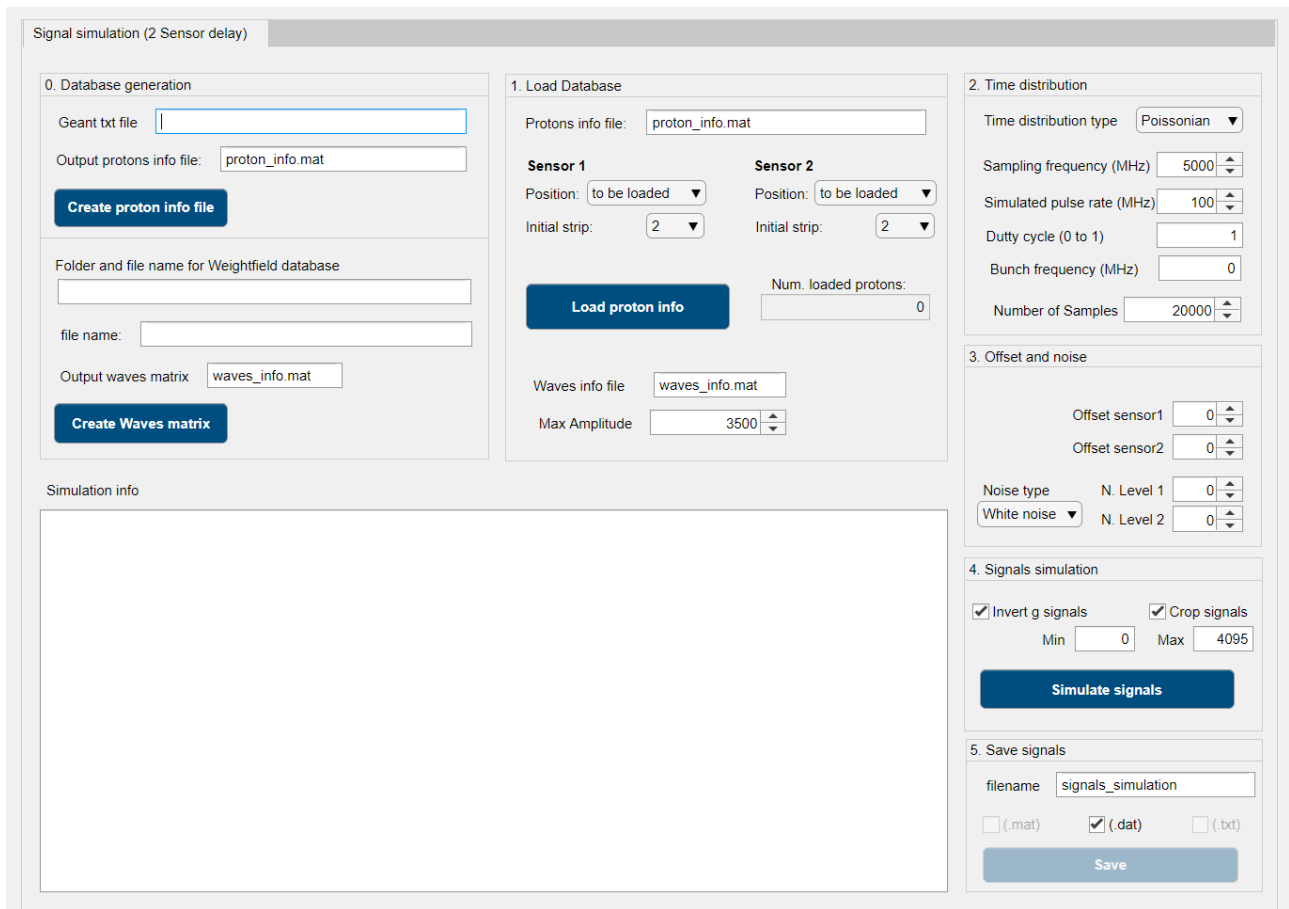


Figure e.1: Signal simulation app interface.

The signals' simulation app is made of 6 steps (Fig. e1). In the step 0, the code loads the data simulated with Geant4 and Weightfield2, and generates two matrices, in a specific format, required for the signals' simulation.

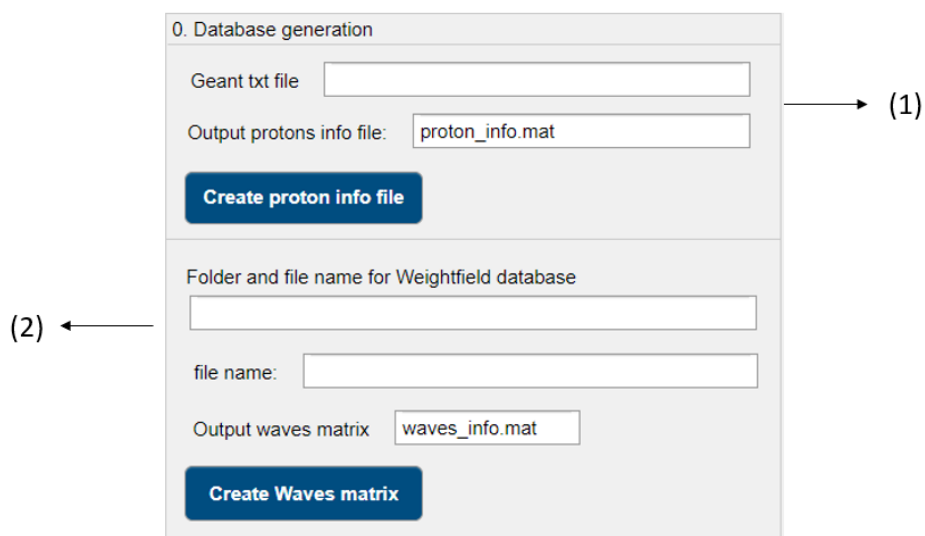


Figure e.2: Step 0 of the signals simulation process.

Meaning of these boxes of step0 (Fig. e.2):

1. Folder in which the Geant4 file is saved. The program analyzes this file and generates a matrix called as the name inserted (proton\_info.mat);
2. Folder and name of the Weightfield file is saved. The program analyzes the file and generates a matrix called as the name inserted (waves\_info.mat).

The Step 1 (Fig. e.3), after having acquired the two matrices (from Geant and Weightfield), allows the user to choose the positions and the initial strip for each detector, and the maximum amplitude of the peaks, expressed in ADC counts. However, the total number of strips per detector (8) is fixed.

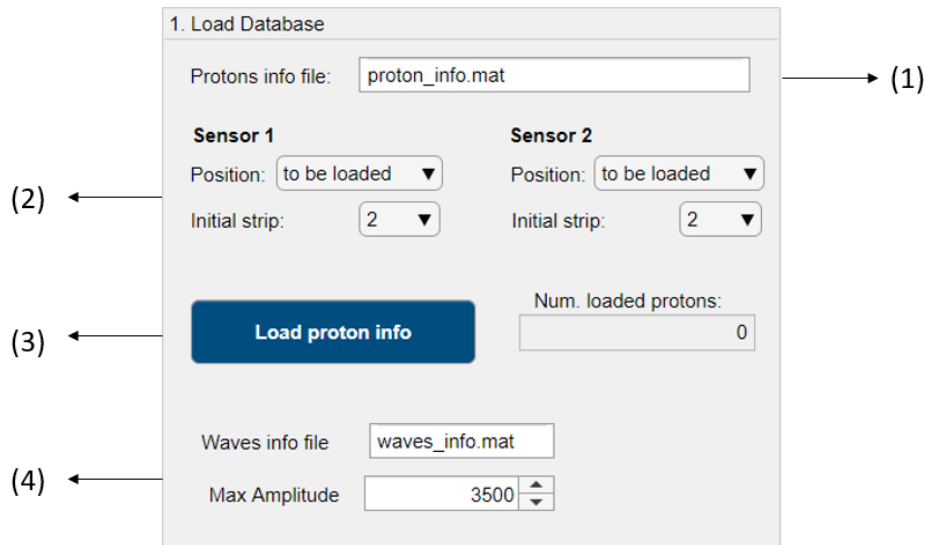


Figure e.3: Step 1 of the signals simulation process.

Meaning of these boxes of step1 (Fig. e.3):

1. Load the matrix of the Geant simulation;
2. Choose the position and the initial strip of the two detectors;
3. Loading the information of the simulated protons, according to the positions and strips indicated in (2);
4. Load the matrix of the Weightfield simulation. The maximum amplitude of the peaks of the signals' simulation can be decided here (ADC counts).

In the step2, the user has to specify some important parameters, that characterize the simulated beam.

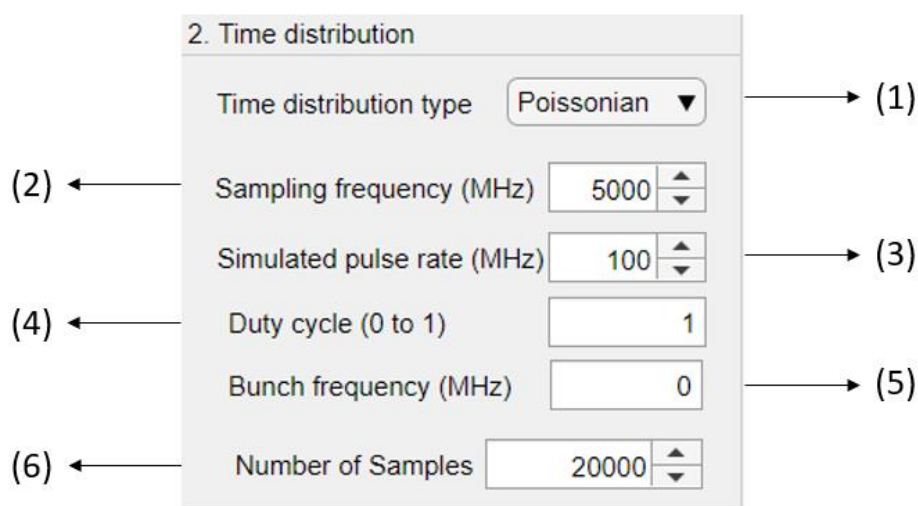


Figure e.4: Step 2 of the signals simulation process.

Meaning of these boxes of step2 (Fig. e.4):

1. Distribution of time intervals between successive peaks;
2. Sampling frequency is the number of samples per second;
3. Simulated pulse rate is the number of pulses per unit of time;
4. The duty cycle is the fraction of one period in which the signal is active. By setting a value different from 1, a non-continuous beam can be simulated;
5. The bunch frequency is the number of pulses of particles emitted per unit of time;
6. The total number of samples is a measure of the time acquisition (1 sample is equal to 0.2 ns).

By modifying these parameters, the beam can be simulated as the one in CNAO (synchrotron), or the one in TPT (cyclotron).

To simulate the acquisition of the DIGITIZER, the sampling frequency must be maintained at 5000MHz (0.2ns).

The total number of pulses comes from the sampling frequency, simulated pulse rate and the number of samples. In this case, for the number present in the Fig. 3.4, it is equal to 400 peaks.

In the step3 (Fig. e.5) the offset (baseline of the signals) and level of noise of the two detectors can be setup.

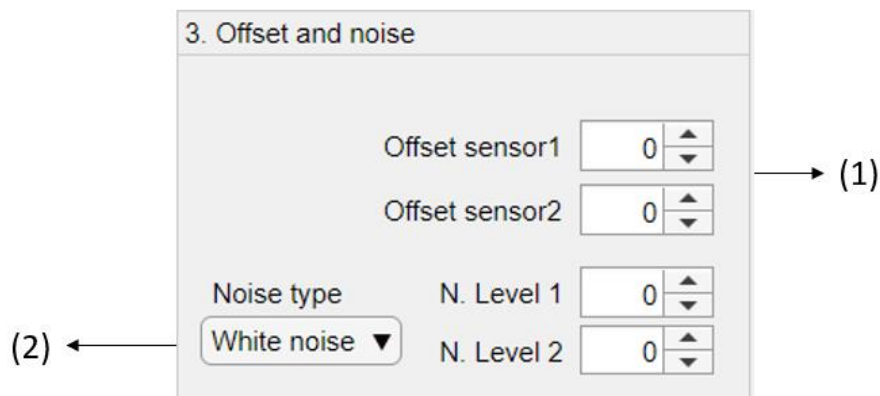


Figure e.5: Step 3 of the signals simulation process.

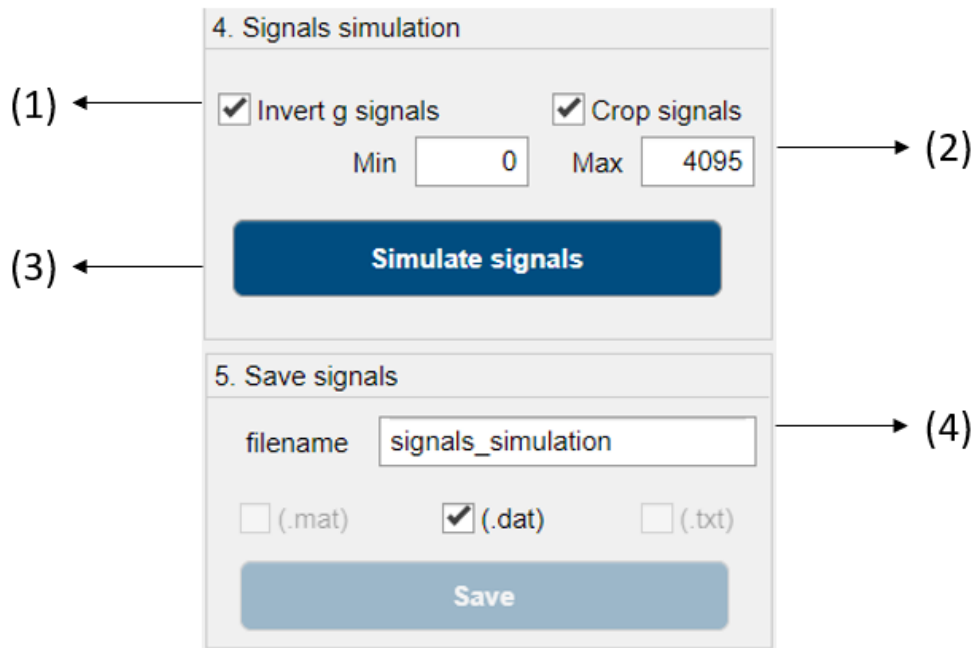


Figure e.6 : Step 4 and 5 of the signals simulation process.

Meaning of these boxes of step4 and step5 (Fig. e.6):

1. This box inverts the signal if they are generated negative;
2. This box cut the signals over the limit (min, max) indicated.
3. Starts the generation of the signals, after having set all the previous parameters.
4. Save the results, in terms of signals per each strip, as wave\_stripdetector1\_stripdetector2, according to the extension indicated.

## Bibliography.

- [1] L.J. Verhey, A.M. Koehler, J.C. McDonald, et al., “The Determination of Absorbed Dose in a Proton Beam for Purposes of Charged-Particle Radiation Therapy”, *Radiation Research*, vol. 79, no. 1, pp. 34, 1979.
- [2] W.D. Newhauser and R. Zhang, “The Physics of Proton Therapy”, *Physics in Medicine and Biology*, vol. 60, no. 8, pp. 155-209, 2015.
- [3] W.R. Leo, *Techniques for Nuclear and Particle Physics Experiments*, Springer, Berlin, 1994.
- [4] M.F. L’Annunziata, “Radiation Physics and Radionuclide Decay” In: *Handbook of Radioactivity Analysis*, Elsevier Inc, pp. 1–162, 2012.
- [5] S. Gagnebin, “Experimental determination of absorbed dose to water in a scanned proton beam using a water calorimeter and an ionization chamber”, *Research, Section B: Beam Interactions with Material and Atoms*, vol. 268, no. 5, pp. 524-528, 2010.
- [6] R. Atun, D.A. Jaffray, M.B. Barton, et al., “Expanding global access to radiotherapy”, *The Lancet Oncology*. vol. 16, no. 10, pp. 1153–1186, 2015.
- [7] U. Amaldi and G. Kraft, “Radiotherapy with beams of carbon ions”, *Reports on Progress in Physics*. vol. 68, no. 8, pp. 1861–1882, 2005.
- [8] T. Elsässer, W.K. Weyrather, T. Friedrich, et al., “Quantification of the relative biological effectiveness for ion beam radiotherapy: Direct experimental comparison of proton and carbon ion beams and a novel approach for treatment planning”, *International Journal of Radiation Oncology Biology Physics*. vol. 78, no. 4, pp. 1177–1183, 2010.
- [9] <https://www.pyrexar.com/protons-vs-carbon-ions>.
- [10] F. Fausti, *Design and test of readout electronics for medical and astrophysics applications*. PhD Thesis, Politecnico di Torino, 2018.
- [11] S. Giordanengo, *Desing, implementation and test of the hardware and software for the fast control of the dose delivery system of Centro Nazionale di Adroterapia Oncologica (CNAO)*. PhD Thesis, Università degli studi di Torino, 2009.
- [12] T. Kubiak, “Beam delivery systems in hadron therapy for cancer treatment”, *PhD Interdisciplinary Journal*, vol. 1, pp. 67–73, 2013.
- [13] T.F. DeLaney, “Charged Issues: Particle Radiation Therapy”, *Seminars in Radiation Oncology*, vol. 28, no. 2, pp. 75–78, 2018.
- [14] F. Tommasino, M. Rovituso, S. Fabiano, et al., “Proton beam characterization in the experimental room of the Trento Proton Therapy facility”, *Nuclear Instruments and Methods in Physics Research, Section A: Accelerators, Spectrometers, Detectors and Associated Equipment*. vol. 869, no. July, pp. 15–20, 2017.
- [15] S. Rossi, “The National Centre for Oncological Hadrontherapy (CNAO): Status and perspectives”, *Physica Medica*, vol. 31, no. 4, pp. 333-351, 2015.
- [16] G.E. Knoll, *Radiation Detection and Measurement Third Edition*, John Wiley & Sons, New York, 2000.
- [17] S. Giordanengo, M.A. Garella, F. Marchetto, et al., “The CNAO dose delivery system for modulated scanning ion beam radiotherapy”, *Medical Physics*, vol. 42, no. 1, pp. 263–275, 2015.
- [18] S.M. Zenklusen, E. Pedroni, and D. Meer, “A study on repainting strategies for treating moderately moving targets with proton pencil beam scanning at the new gantry 2 at PSI”, *Physics in Medicine and Biology*, vol. 55, no. 17, pp. 5103–5121, 2010.
- [19] S. Van De Water, R. Kreuger, S. Zenklusen, E. Hug, and A.J. Lomax, “Tumour tracking with scanned proton beams: Assessing the accuracy and practicalities”, *Physics in Medicine and Biology*, vol. 54, no. 21, pp. 6549–6563, 2009.

- [20] S.E. McGowan, N.G. Burnet, and A.J. Lomax, “Treatment planning optimisation in proton therapy”, *British Journal of Radiology*, vol. 86, n. 1021, 2013.
- [21] A. Vignati, V. Monaco, A. Attili, et al., “Innovative thin silicon detectors for monitoring of therapeutic proton beams: Preliminary beam tests”, *Journal of Instrumentation*, vol. 12, no. 12, 2017.
- [22] MATLAB version 9.5.0.1178774 (R2018b), The Mathworks, Inc., Natick, Massachusetts, 2018.
- [23] S.O. Grözinger, C. Bert, T. Haberer, G. Kraft, and E. Rietzel, “Motion compensation with a scanned ion beam: A technical feasibility study”, *Radiation Oncology*. vol. 3, no. 1, 2008.
- [24] M. Krim, N. Harakat, A. Khouaja, et al., “Method for range calculation based on empirical models of proton in liquid water: Validation study using Monte-Carlo method and ICRU data”, *International Journal of Scientific & Engineering Research*. vol. 8, no. 3, pp. 728–735, 2017.
- [25] H.M. Tawfeek, F.M. Hady, and M.K. Jassim, “Investigations into the Proton Stopping Power of Human Body”, *Journal of chemical, Biological and Physical Sciences*. vol. 5, no. 4, pp. 4345–4354, 2015.
- [26] R.B. and F. Rademakers, "ROOT- An object oriented data analysis framework", *Nuclear Instruments and Methods in Physics Research, Section A: Accelerators, Spectrometers, Detectors and Associated Equipments*, vol. 389, no. 1-2, pp. 81-86, 1997.
- [27] S. Agostinelli, J. Allison, K. Amako, et al., “GEANT4 - A simulation toolkit”, *Nuclear Instruments and Methods in Physics Research, Section A: Accelerators, Spectrometers, Detectors and Associated Equipment*, vol. 506, no. 3, pp. 250–303, 2003.
- [28] F. Cenna, N. Cartiglia, M. Friedl, et al., “Weightfield2: A fast simulator for silicon and diamond solid state detector”, *Nuclear Instruments and Methods in Physics Research, Section A: Accelerators, Spectrometers, Detectors and Associated Equipment*. vol. 796, pp. 149–153, 2015.